Local Dynamics and Bending Mechanics of Mesostructured Materials

Dissertation zur Erlangung des Grades:
"Doktor der Naturwissenschaften"
am Fachbereich Physik, Mathematik und Informatik der
Johannes Gutenberg-Universität Mainz

MAX-PLANCK-GESELLSCHAFT

vorgelegt von
Tomas P. Corrales
geboren in Santiago, Chile

Max-Planck-Institut für Polymerforschung
Mainz, 2013

Tag der Mündlichen Prüfung : 21.11.2013

Zusammenfassung

Die vorliegende Arbeit behandelt die Anwendung der Rasterkraftmikroskopie auf die Untersuchung mesostrukturierter Materialien. Mesostrukturierte Materialien setzen sich aus einzelnen mesoskopen Bausteinen zusammen. Diese Untereinheiten bestimmen im Wesentlichen ihr charakteristisches Verhalten auf äußere mechanische oder elektrische Reize, weshalb diesen Materialien eine besondere Rolle in der Natur sowie im täglichen Leben zukommt. Ein genaues Verständnis der Selbstorganisation dieser Materialien und der Wechselwirkung der einzelnen Bausteine untereinander ist daher von essentieller Bedeutung zur Entwicklung neuer Synthesestrategien sowie zur Optimierung ihrer Materialeigenschaften. Die Charakterisierung dieser mesostrukturierten Materialien erfolgt üblicherweise mittels makroskopischer Analysemethoden wie der dielektrischen Breitbandspektroskopie, Thermogravimetrie sowie in Biegungsexperimenten. In dieser Arbeit wird gezeigt, wie sich diese Analysemethoden mit der Rasterkraftmikroskopie verbinden lassen, um mesostrukturierte Materialien zu untersuchen. Die Rasterkraftmikroskopie bietet die Möglichkeit, die Oberfläche eines Materials abzubilden und zusätzlich dazu seine quantitativen Eigenschaften, wie die mechanische Biegefestigkeit oder die dielektrische Relaxation, zu bestimmen. Die Übertragung makroskopischer Analyseverfahren auf den Nano- bzw. Mikrometermaßstab mittels der Rasterkraftmikroskopie erlaubt die Charakterisierung von räumlich sehr begrenzten Proben bzw. von Proben, die nur in einer sehr kleinen Menge (<10 mg) vorliegen. Darüberhinaus umfasst das Auflösungsvermögen eines Rasterkraftmikroskops, welche durch die Größe seines Federbalkens (50 μm) sowie seines Spitzenradius (5 nm) definiert ist, genau den Längenskalenbereich, der einzelne Atome mit der makroskopischen Welt verbindet, nämlich die Mesoskala. In dieser Arbeit werden Polymerfilme, kolloidale Nanofasern sowie Biomineralien ausführlicher untersucht.

Im ersten Projekt wird die Spitze des Rasterkraftmikroskops als dielektrischer Sensor verwendet, um die Dynamik von Polymeren mit einer lateralen Auflösung im Sub-Mikrometerbereich zu analysieren. Diese Methode wird auch als lokale Dielektrizitätsspektroskopie bezeichnet. Hier wird sie angewendet, um ein mischbares Polymergemisch bestehend aus Polyvinylacetat (PVAc) und Polyethylenoxid (PEO) zu untersuchen. Diese Homopolymere weisen sehr unterschiedliche Relaxationszeiten sowie Glastemperaturen auf. Messungen der lokalen Zusammensetzung von 200 nm dicken Filmen zeigen, dass die lokale Dielektrizitätsspektroskopie dynamische Heterogenitäten in einer Größenordnung von 100 nm auflösen kann. In dünneren Polymerfilmen tritt Phasenseparation auf. Die Änderung der lokalen Filmzusammensetzung mit der Zeit kann dabei als Maß genutzt werden, um die Entmischungsgeschwindigkeit zu quantifizieren. Damit eröffnen sich neue Möglichkeiten, die Interdiffusion und Adhäsion an der Polymer-

Polymergrenzflä-che als Funktion der Glühtemperatur mittels lokaler Dielektrizitätsspektroskopie zu untersuchen.

Das zweite Projekt dieser Arbeit befasst sich mit der Charakterisierung der mechanischen Eigenschaften von kolloidalen Nanofasern, in die definierte Fehlstellen eingebracht werden. Diese Nanofasern setzen sich aus Siliziumoxid-Nanopartikeln als strukturgebende Bausteine sowie aus Polystyrol-Nanopartikeln als lochbildende Komponente zusammen. Ihre Herstellung erfolgt über das sog. bikolloidale Elektrospinning. Nach der anschließenden Kalzinierung verbleiben an Stelle der Polystyrol-Partikel Fehlstellen mit definierter Größe und Verteilung in der Nanofaser. Des Weiteren sintern die Siliziumoxid-Partikel während des Erhitzens zu einer mechanisch stabilen Faser mit einem mittleren Durchmesser von 300 nm zusammen. Die mechanischen Eigenschaften dieser Nanofasern können dann mittels eines Drei-Punkt-Biegeexperiments bestimmt werden. Die Untersuchung von Fasern ohne Fehlstellen sowie von Fasern mit jeweils 60 nm bzw. 260 nm großen Fehlstellen zeigen, dass die Einführung von Fehlstellen sowohl das Elastizitätsmodul als auch die mechanischen Brucheigenschaften der Fasern beeinflussen. Im Hinblick auf die Brucheigenschaften zeigen dabei die Fasern mit einer Fehlstellengröße von 60 nm eine einheitliche Fragmentierung in jeweils drei Bruchstücke, während die Fasern ohne Fehlstellen sowie solche mit 260 nm großen Fehlstellen wahlweise in zwei bis drei Segmente zerbrechen. Darüberhinaus können die beim Bruch der Fasern auftretenden Kräfte und Spannungen quantifiziert werden. Eine genaue Kenntnis der auftretenden Kräfte ist eine Grundvoraussetzung für die kontrollierte Fragmentierung von Nanofasern zur Herstellung anisotroper Nanopartikel.

Im letzten Projekt werden Biegeexperimente von biomineralischen Nadeln durchgeführt. Sowohl natürlich vorkommenden als auch synthetisch hergestellte Nadeln bestehen aus einer Mischung aus Mineralien (Kalzit) und Proteinen und besitzen eine vergleichbare Größe. Ihre mechanischen Eigenschaften können über Biegeexperimente im Rasterkraftmikroskop untersucht werden. Beide Nadeln weisen eine vergleichbare mechanische Biegesteifigkeit auf, hingegen gibt es signifikante Unterschiede in ihrem Bruchverhalten. Die synthetischen Nadeln zeigen eine deutlich stärkere mechanische Widerstandsfähigkeit, welche sich in ihrem etwa 10-fach höheren Proteinanteil begründet, wie durch thermogravimetrische Messungen mittels Rasterkraftmikroskopie ermittelt werden kann. Diese veränderte Zusammensetzung der synthetischen Nadeln resultiert in einer veränderten hierarchischen Architektur, die wiederum die Brucheigenschaften der synthetischen Fasern beeinflusst.

Alle diese Projekte demonstrieren die vielseitige Einsetzbarkeit der Rasterkraftmikroskopie zur Charakterisierung mesostrukturierter Materialien. Die Korrela-

tion ihrer mechanischen und dielektrischen Eigenschaften mit ihrer topographischen Beschaffenheit erlaubt ein tieferes Verständnis der mesoskopischen Materialien und ihres Verhaltens auf die Einwirkung äußerer Reize.

Abstract

This thesis explores the applications of ***scanning probe microsocpy*** (SPM) in the study of mesostructured materials. Materials composed of mesoscopic building blocks are defined as ***mesostructured***. A main feature of these materials is that their reaction to external stimuli, e.g. electric or mechanical, is controlled by mesoscopic structures. These materials play a central role in daily life applications and are found in nature. Knowledge of how mesostructured materials self-assemble and their building blocks interact is of fundamental importance in order to tune their properties and develop new synthesis schemes. Mesostructured materials are typically tested with macroscopic experiments, e.g. broadband dielectric spectroscopy (BDS), bending tests and thermal gravimetric analysis (TGA). In this thesis, ways to combine the main features of these testing experiments with SPM have been demonstrated and used to study mesostructured materials. SPM offers a unique way to image the surface and obtain quantitative properties of mesostructured materials, e.g. mechanical stiffness and dielectric relaxation. Expanding macroscopic testing experiments to the micro- and nanoscale with SPM allows the study of samples that are spatially reduced or prepared in small quantities (<10 mg). Furthermore, the dimensions of the SPM tip (5 nm) and cantilever (50 μm) makes it an essential tool to cover the length scales that separate single atoms with our macroscopic world, i.e. the mesoscopic scale. Materials of interest throughout this work include polymer blends, colloidal nanofibers and biominerals.

In a first project, the SPM tip is used as a dielectric sensor in order to measure polymer dynamics with a sub-micrometer spatial resolution. This technique is called local dielectric spectroscopy (local-DS). Local-DS is employed to analyze a miscible blend composed of poly(vinyl acetate) (PVAc) and poly(ethylene oxide) (PEO). The two homopolymers have very different relaxation times and glass transition temperatures. Measurements of the local blend composition in 200 nm thick films show that local-DS is sensitive to dynamic heterogeneity with a lateral resolution of around 100 nm. In thinner films (50 nm), phase segregation occurs, and the kinetics of phase demixing is studied using as a probe the change in local composition. These results open new possibilities for studying interdiffusion and adhesion at polymer-polymer interfaces as a function of annealing temperature with local-DS.

The second project involves the characterization of the mechanical properties of colloidal nanofibers, where well defined voids are introduced. These nanofibers are prepared from silica nanoparticles, used as the structural building blocks, and polystyrene nanoparticles, introduced as sacrificial material. Nanofibers are fabricated by bicolloidal electrospinning. After a calcination step the sacrificial

particles are successfully converted to voids with controlled average size and occurrence in the fiber. Furthermore, the silica nanoparticles are sintered during the calcination step, yielding a mechanically stable fiber with a diameter of around 300 nm. The mechanical properties of the sintered colloidal nanofibers with tunable-sized voids are investigated with a nano-mechanical three-point bending experiment. Three different cases are investigated: fibers without voids, with 60 nm, and 260 nm voids. It is shown that the introduction of voids can be used to control the Young's modulus and fracture properties of the nanofibers. It is found that fibers with 60 nm voids fracture into three segments, whereas fibers with no voids and 260 nm voids, fracture either into two or three segments. The forces involved in the fracture process, and respective fracture stresses, are also determined. Knowledge of the forces and stresses involved in nanofiber fracture is a prerequisite for the controlled fragmentation of nanofibers to yield anisotropic particles.

Finally, in a last project, bending experiments are performed on biomineral spicules. Natural and synthetic spicules are made from a combination of mineral (calcite) and protein. Synthetically produced spicules are found to have similar dimensions as their natural counterparts. Using SPM bending experiments, it is found that synthetic and natural spicules have similar mechanical stiffness, but differ significantly in how they react to large deformations, i.e. how they fracture. From fracture experiments, it is found that synthetic spicules are mechanically more resistant than natural spicules. Using a nano-TGA procedure it is found that synthetic spicule have at least 10 times more protein content than natural spicules. This fact, in combination with their different hierarchical architectures, explain the differences seen in their fracture properties.

These projects demonstrate that SPM is a powerful tool for studying mesostructured materials. Quantitative information about mechanical or dielectric properties in correlation with topographical imaging, allows a deeper understanding of mesostructured materials and their reaction to external stimuli.

Contents

Chapter 1

Introduction

In condensed matter physics, the mesoscopic regime refers to the intermediate length scale that bridges single atoms (0.1 nm) with the continuous macroscopic world, e.g. the size of a human hair (100 μm). Although atomic and macroscopic scales are well described by quantum and classical mechanics respectively, mesoscale phenomena cannot be described solely by laws that are valid for single atoms. [1] Some universal examples of phenomena occurring on the mesoscale are: collective behavior of identical units, appearance of defects, and heterogeneity in structure and dynamics. [2] Figure 1.1 depicts the mesoscopic regime with some examples of relevant mesostructures studied throughout this work, e.g. polymers, proteins, mesocrystals and colloidal particles.

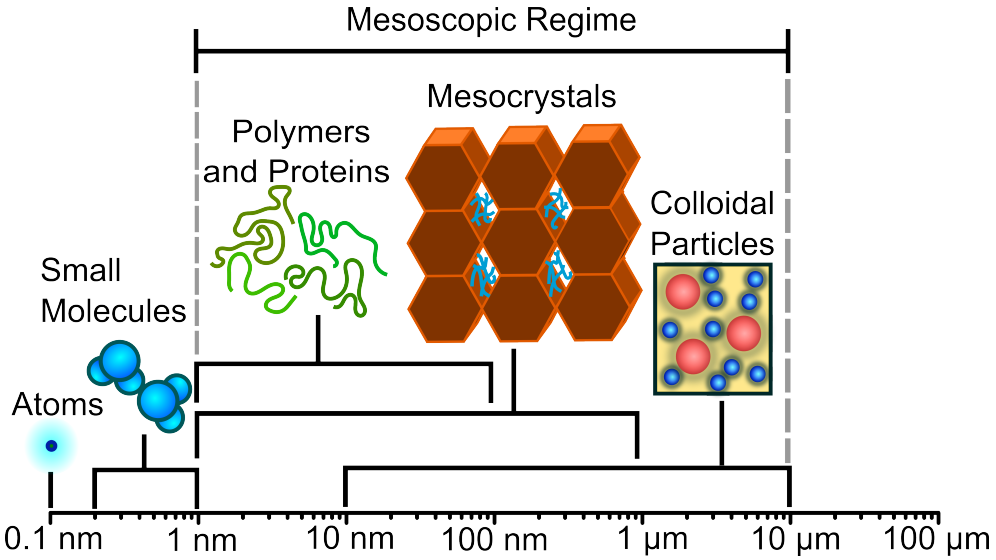

Figure 1.1: *The mesoscopic regime and some examples of structures that organize themselves to produce mesostructured materials.*

The fundamental building blocks of matter, single atoms, assemble into these mesoscopic structures using two different architectural platforms: the periodic lattice (crystals) or the chemical bond (molecules). Materials composed of mesoscopic structures are defined as ***mesostructured*** from hereon. A main feature of these materials is that their reaction to external stimuli, e.g. electrical or mechanical, is controlled by structures that assemble on the mesoscale. Mesoscopic structures play an essential role in the properties of materials present in modern life applications and can be found also in nature. A key example are polymers, which are the fundamental building blocks of such ubiquitous products as rubber tires, plastics containers and textile fabrics (Fig. 1.2a-c). Furthermore, mesostructures are also fundamental in biology, where structures such as proteins, DNA and lipid bilayers form the basis of living cells, i.e. the basic structural unit of living organisms. A collections of cells, in turn, forms biological tissue, which gathers into functional units called organs, e.g. the human eye (Fig. 1.2d). Plastics and biological matter are considered soft, with Young's moduli spanning 1 MPa to 1 GPa. [3] Proteins can also interact with inorganic nanocrystals to form hard macroscopic materials, with Young's moduli $\geq$ 10 GPa, e.g. skeletal structures (Fig. 1.2e). Skeletal structures are produced in a process termed biomineralization, [4] where protein and nanocrystals assemble in a structural unit termed mesocrystal. Protein mineral interactions can give way to intricate shapes seen in nature, e.g. diatoms (1.2f).

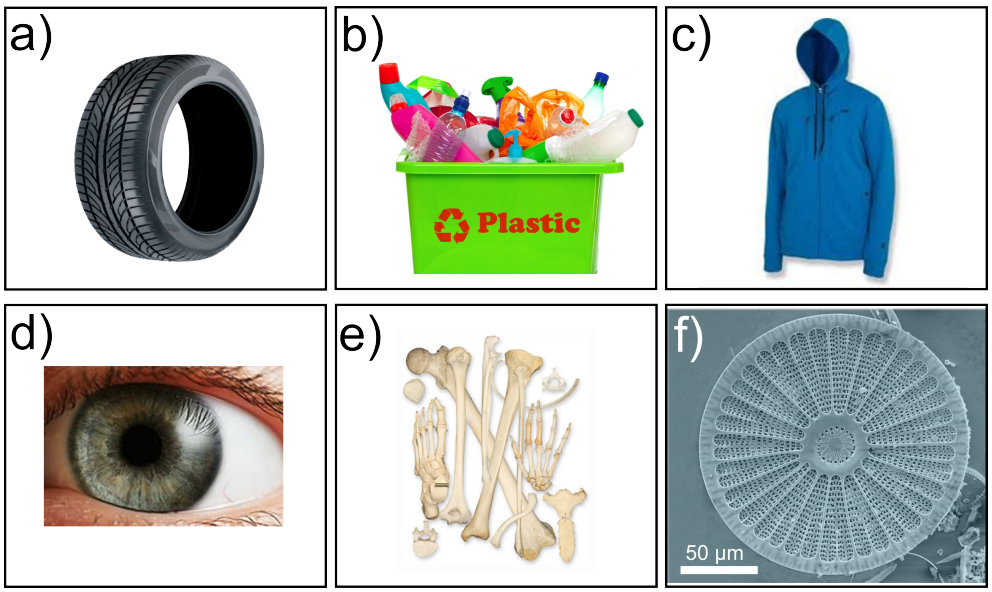

Figure 1.2: *Mesostructured materials in daily life, e.g. a) car tires, b) plastic containers c) synthetic clothes, and in nature, e.g. d) biological organs, e) bones and f) diatoms (adapted from Alfred-Wegener-Institut www.awi.de).*

Even though mesostructured materials are involved in several everyday applications and are essential for biological matter, there is still much to learn about the underlying physics happening within the mesoscopic regime. Some points of ongoing research in mesoscale science include the physical nature of the glass transition [5] and the process of biomineralization. [6] This last research topic consists in understanding how soft matter (<1 GPa), such as proteins are able to create harder materials (>10 GPa), such as bone, by incorporating inorganic minerals. In particular, a key question in this field, is how proteins affect the crystallization process, creating crystal structures that are completely different from normal inorganic crystals of the same material.

Many experimental methods have been developed to study mesostructured materials along their different length scales. On macroscopic scales some common techniques to probe the mechanical and thermal properties of mesostructured materials include: Rheology, Flexural Testing, Differential Scanning Calorimetry (DSC) and Thermal Gravimetric Analysis (TGA).

On the other end of the scale, optical tweezers [7] have become an attractive technique to probe movement and rupture forces of single molecules. Between these two length scales there are several orders of magnitude, where interactions, collective motion and structure of mesoscale building blocks become relevant for the final properties of the material. Some techniques with which these intermediate scales can be accessed include: scanning electron microscopy (SEM), transmision electron microscopy (TEM) [8], x-ray scattering [9], flourescence correlation spectroscopy (FCS) [10], broadband dielectric spectroscopy (BDS) and ***scanning probe microscopy*** (SPM).

From all these techniques, one of the most versatile ones is SPM. SPM is an important technique in the study of mesostructured materials given the option of combining imaging with force measurements at length scales that can go from single atoms to several microns. Several developments within the last decade have taken SPM from a bare imaging instrument to a quantitative tool with which mesoscopic mechanical and dielectric properties can be characterized.

An advantage of SPM arises from the fact that mesostructured materials are often available in small quantities only (<10 mg), or are produced within spatially limited dimensions (10 nm - 100 μm). Under these conditions macroscopic thermal (DSC, TGA) and flexural testing experiments are not feasible. Therefore, new techniques to mimic macroscopic testing experiments with limited amounts of material and reduced length scales are required. In this sense SPM represents a convenient way to adapt many of the macrosocpic mechanical, thermal and dielectric experiments, to samples that are structured on length scales comparable

to the size of the SPM tip (5 nm) or cantilever (50 μm).

This thesis explores mechanical and dielectric properties of mesostructured materials using different SPM-related methods that are adapted from macroscopic mechanical and dielectric testing. In particular, focus shall be centered on the measurement of local dynamics within polymer blends and bending mechanics of mesostructured fibers. By employing SPM as a mechanical and dielectric sensor, quantitative information is obtained on how materials are structured on the mesoscopic regime and the influence this has on their macroscopic properties.

In remainder of this chapter the different mesoscopic structures which shall appear throughout this work are introduced to the reader. These systems include: polymers and polymer blends (1.1), colloids and colloidal fibers (1.2), and biominerals (1.3). In chapter 2 the fundamentals of SPM shall be described and the different SPM variations employed to obtain the quantitative information shown throughout this work are described. In chapter 3 the experimental setups and sample preparation methods are detailed.

Within chapters 4, 5 and 6 results and discussions regarding measurements on mesostructured materials using SPM shall be presented. Chapter 4 is centered on the local dynamics and phase separation kinetics of a polymer blend. In chapter 5, results regarding the mechanical properties of colloidal nanofibers are shown. Finally in chapter 6, the mechanical properties and organic content of biominerals are measured using SPM.

1.1 Polymers

Polymers are molecules composed of n repeating chemical units, or monomers, connected to each other by covalent bonds to form a chain. The main property of a polymer is that the addition or subtraction of a few monomers within the chain does not considerably affect the final properties of the material. This requirement is fulfilled when the number of repeating units is large, $n \geq 1000$. The simplest polymer is polyethylene (PE), which consists only of repeating ethylene units (Fig. 1.3a). In the simple case of PE, carbon atoms form a zig-zag structure sharing a single electron with the next adjacent carbon atom and 2 electrons with 2 neighboring hydrogen atoms. Two hydrogen atoms (sketched as white spheres) are bonded to each carbon atom (sketched as black spheres) along the monomer in a tetrahedral arrangement (Fig. 1.3b).

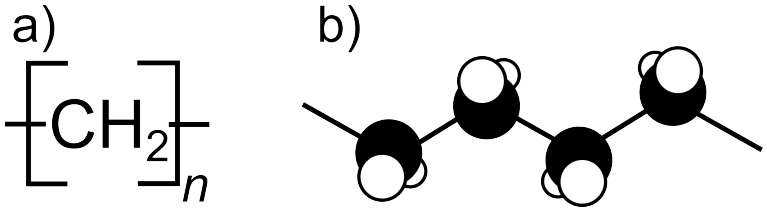

Figure 1.3: *a) Repeating unit of the polymer Polyethylene (PE). b) PE linear chain, where black and white spheres represent carbon and hydrogen atoms respectively.*

Common polymers exhibit structures similar to that of PE, i.e. they consist of a carbon chain backbone, where only one or both of the hydrogens are replaced by more complex side groups. An example would be polystyrene (PS), where a hydrogen atom is replace by benzene. In general, distances (a=1.54 Å) and tetrahedral angles (θ=0.68^o) between carbon atoms of a polymer molecule are fixed. This means that on the local scale of single monomers, a polymer chain may seem to be a rigid structure. Flexibility in single polymer chains arises from *gauche* defects within the chain's backbone. *Gauche* defects within the chain makes the carbon atom snap out from the plane containing the other in-plane carbon atoms (Fig. 1.4a). Successive *gauche* defects give the chain its flexibility. The concept of a length scale where the polymer chain appears to be flexible is called the persistence length of the chain and is related to the energy required to snap from an in-plane (*trans*) configuration to a *gauche* configuration (Fig. 1.4b).

An important concept in polymer physics is the polymer conformation, in other words, how the polymer chain is distributed in space. The conformation of a

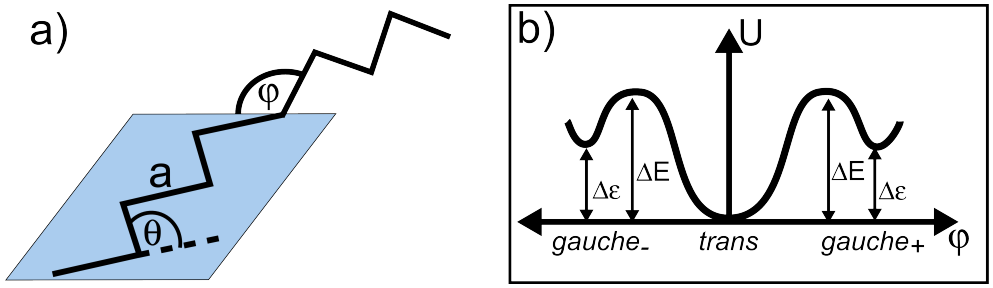

Figure 1.4: *a) Flexibility in polymer chains arises from gauche defects which alter the torsional angle of the polymer φ. b) Binding energy as a function of torsional angle φ. Gauche defects represent local minimums.*

single polymer chain depends on three factors: flexibility of the chain, interactions between monomers of the chain, and interactions between the chain and its surrounding environment. In the simple case of a single and isolated PE chain without *gauche* defects, the chain length reaches a maximum extension: $R_{max} = na \cdot cos(\theta/2)$. This maximum extension is called the *contour length*, where n is the number of carbon atoms of the chain.

In order to describe the conformation of a flexible polymer the concept of ideal chains is introduced, in which no external interactions arising from the polymer's environment are considered. An ideal polymer chain can be modeled as a collection of beads randomly distributed. Each bead represents the position of a carbon atom and is connected to other atoms by bond vectors $\vec{r}_i$ of fixed length ($|\vec{r}_i| = a$) as depicted in figure 1.5.

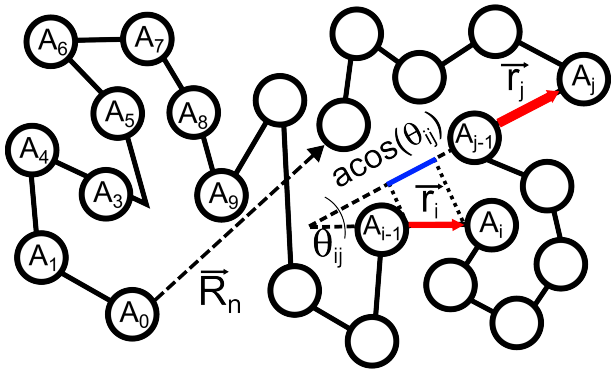

Figure 1.5: *Random polymer chain where a collection of randomly distributed carbon atoms (A_i) are connected through bond vectors $\vec{r}_i$. Bond vectors $\vec{r}_i$ and $\vec{r}_j$ form an angle θ_{ij}*

The polymer is defined as an ideal chain if there are no interactions between

atoms A_i and A_j for large separations, this means $|i-j| \gg 1$. The contour length for such a chain model is $R_{max} = na$, assuming arbitrary bond angles (θ). An important definition in this model is the end-to-end vector $\vec{R}_n$, which is the sum of all bond-vectors connecting individual beads within the chain in figure 1.5:

$$\vec{R}_n = \sum_{i=1}^{n} \vec{r}_i \tag{1.1}$$

If the end-to-end vector is averaged over all possible conformations of a single polymer, or a large amount of randomly distributed polymer chains, then $\left\langle \vec{R}_n \right\rangle = 0$. Therefore it is more meaningful to introduce the mean square end-to-end distance:

$$\left\langle R^2 \right\rangle \equiv \left\langle \vec{R}_n^2 \right\rangle = \sum_{i=1}^{n} \sum_{j=1}^{n} \langle \vec{r}_i \cdot \vec{r}_j \rangle \tag{1.2}$$

where $\langle \ \ \rangle$ denotes the average over all possible polymer configurations. If all bond vectors have the same length a, then the vector point product is $\vec{r}_i \cdot \vec{r}_j = a^2 \cos(\theta_{ij})$ and equation 1.2 becomes:

$$\left\langle R^2 \right\rangle = a^2 \sum_{i=1}^{n} \sum_{j=1}^{n} \langle cos(\theta_{ij}) \rangle \tag{1.3}$$

where $\langle cos(\theta_{ij}) \rangle$ is a measure of the correlation between bonds i and j averaged over all possible configurations of the chain. In the simplest of cases, called the *freely joint chain model*, no correlations are found between the different configurations, therefore: $\langle cos(\theta_{ij}) \rangle = 0$ for $i \neq j$ and only terms $i = j$ contribute to the average ($\langle cos(\theta_{ij}) \rangle = 1$), yielding:

$$\left\langle R^2 \right\rangle = na^2 \tag{1.4}$$

In real polymer systems, there are correlations between bond vectors, especially near neighboring atoms. Such correlations yield $\langle cos(\theta_{ij}) \rangle \neq 0$ for $i \neq j$. For very long chains such a correlation factor converges to a finite number called the characteristic ratio (C_∞) and thus:

$$\left\langle R^2 \right\rangle = C_\infty na^2 \tag{1.5}$$

A simplification of this model is the *equivalent freely jointed chain*, where the complete chain description, with all its atoms, is replaced by an equivalent chain with N joints and an effective bond length l_K. This equivalent bond length is called the *Kuhn length*. In this description, the countour length is $R_{max} = Nl_K$ and the average square end-to-end distance is $\langle R^2 \rangle = Nl_K^2$. Which means that the Kuhn length is:

$$l_K = \frac{\langle R^2 \rangle}{R_{max}} = \frac{C_\infty na^2}{R_{max}} \tag{1.6}$$

In a physical sense, the Kuhn length is the scale on which polymer chains appear to be stiff. For example, a polyethylene (PE) chain with characteristic ratio $C_\infty = 7.4$, a Kuhn length $l_K = 14$ Å is calculated using equation 1.6.

Polymers do not always form linear macromolecules, but may also branch and form diverse types of structures, such as rings, combs, or ladders (Fig. 1.6b-f).

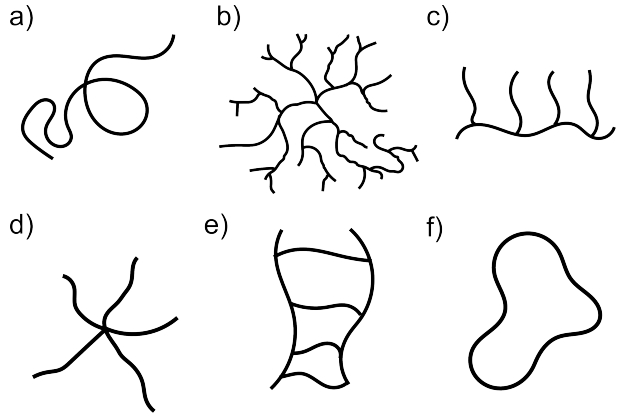

Figure 1.6: *Types of polymer architectures: a) linear, b) dendrite, c) comb, d) star, e) ladder and f) ring.*

A convenient way to describe the size of such polymers is by defining the *radius of gyration* ($\vec{R}_g$). The radius of gyration considers the polymer size as the average distance of each of its Kuhn components (R_i) to the center of mass of the structure ($\vec{R}_{cm}$):

$$R_g^2 = \frac{1}{N}\sum_{i=1}^{N}\left(\vec{R}_i - \vec{R}_{cm}\right)^2 \tag{1.7}$$

Given that the center of mass for equal mass particles is:

$$\vec{R}_{cm} = \frac{1}{N}\sum_{j=1}^{N}\vec{R}_j \tag{1.8}$$

then equation 1.7 reduces to,

$$R_g^2 = \frac{1}{N^2}\sum_{i=1}^{N}\sum_{j=1}^{N}\left(\vec{R}_j - \vec{R}_j\right) \tag{1.9}$$

For averages over allowed conformations equation 1.9 becomes:

$$\left\langle R_g^2\right\rangle = \frac{1}{N^2}\sum_{i=1}^{N}\sum_{j=1}^{N}\left\langle\left(\vec{R}_j - \vec{R}_j\right)\right\rangle \tag{1.10}$$

For an ideal polymer chain equation 1.10 is solved by transforming the summation to an integral over the Kuhn length (l_k), yielding:

$$\begin{aligned} \left\langle R_g^2 \right\rangle &= \frac{l_k^2 N}{6} \\ &= \frac{\langle R^2 \rangle}{6} \end{aligned} \tag{1.11}$$

In general, gyration radii are calculated by integrating over the equivalent freely joint chain. A ring chain, for example, has a gyration radius of: $\left\langle R_g^2 \right\rangle = N l_k^2/12$.

Single polymer chains, as described up to now, are mesoscopic structures. A large quantity of polymer chains ($\sim 10^{-20}$ molecules) forms a macroscopic material, i.e. polymer substance. Pure polymer substances can be liquid or solid depending on thermodynamic variables, mainly temperature.

1.1.1 Polymer Liquids

Pure polymer liquids are usually referred to as polymer melts. Typically such polymer substances are at a temperature in which polymer chains are thermally active. This means that they are able to move and flow when sheared. The relevant temperatures above which polymer melts are obtained is usually referred to as the melting temperature (T_m). Polymer melts, although having liquid properties, conserve an elastic component. This mixed elastic and fluid properties is termed *viscoelasticity* and is one of the major traits of polymers melts. Polymer melts which are cooled down below T_m form the next type of polymer substance to be described, polymer solids.

1.1.2 Polymer Solids

Polymers can form amorphous or semicrystalline solids when cooled below their melting temperature (T_m). In order to describe these two different solidification processes, specific volume ($v^*=\rho^{-1}=V/m$) versus temperature plots are used. Figure 1.7 depicts specific volume plots for a generic substance, not necessarily a polymer, which can solidify completely into a crystal or an amorphous material depending on cooling rate.

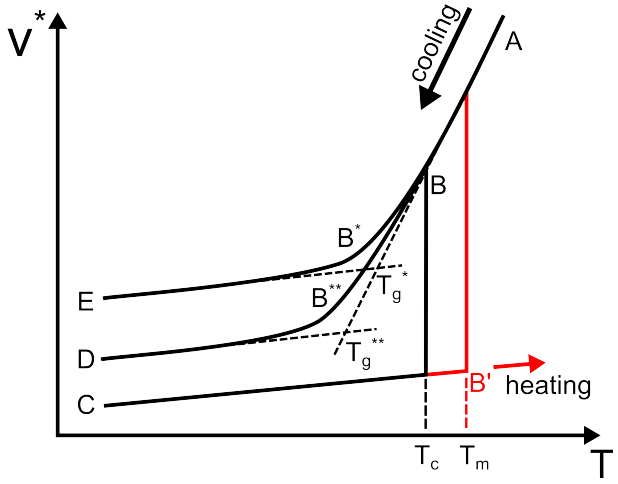

Figure 1.7: *Specific volume for different cooling routes: A-B-C, A-B*-D and A-B**-E*

In the specific volume plot shown above, three different cooling routes are shown that: A-B-C, A-B*-D and A-B**-E. Each route has a different cooling rate, which gives way to different features. When cooling slowly (A-B-C), the substance completely crystallizes at a temperature T_c. Such a crystallization process is a first order phase transition that is accompanied by an increase in mechanical stiffness, expansion coefficients and density of the solid. If this route is inverted (C-B'-A), then the solidified substance melts at T_m. When the melt is cooled at a faster rate (A-B*-D), the substance avoids crystallization at T_c and forms a supercooled liquid. If further cooled along route A-B*-D, an amorphous solid is formed at the glass transition temperature (T_g). The glass transition is observed in route A-B*-D as a change in slope of the specific volume plot, which represents a change in expansion coefficient of the material. If the substances is cooled at an even faster rate (A-B**-E), the substance goes through a glass transition at a temperature below the previous route ($T_g^{**} < T_g^*$).

Common polymers usually solidify completely into amorphous materials, i.e. a glass, exhibiting a kink and change in specific volume at T_g. It is well accepted

that the glass transition is not a thermodynamic phase transition, given that T_g depends on the cooling rate. Polymers are not the only types of molecules that form glasses, another very famous glass forming material is silicon oxide (SiO_2), which in amorphous state is commonly termed silica. Polymers which can crystallize generally do not crystallize completely, like in cooling route A-B-C, but form crystalline regions that are separated by amorphous regions. These materials are called *semicrystalline polymers* and, depending on the degree of crystallization, show both crystallization and glass transition features in specific volume curves.

1.1.3 The Glass Transition

The glass transition, as explained in the previous section, consists in the amorphous solidification of a melted substance. Such a solidification brings extraordinary changes in the material. In order to obtain a glass, a liquid must be cooled fast enough to avoid crystallization. When crystallization is avoided and the substance reaches T_g an amorphous material, i.e. a glass, is formed. The formation of a polymer glass is accompanied by an increase of around 3 orders of magnitude in the materials' mechanical stiffness, e.g. Young's modulus (E). The viscosity (η) of the material suffers even more drastic changes, increasing 6 orders of magnitude for polymers cooled below T_g (Fig. 1.8b).

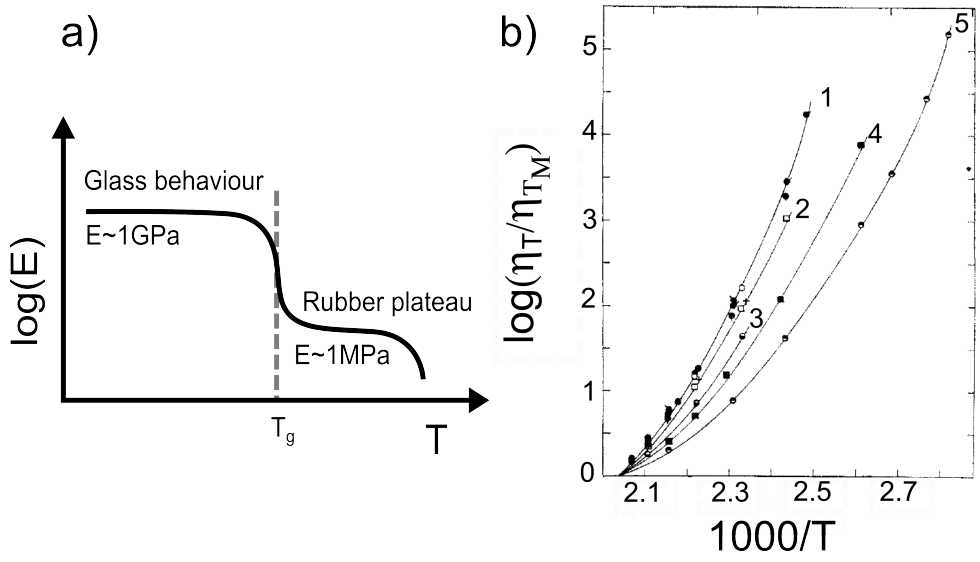

Figure 1.8: *a) Young's modulus of a polymer melt when cooled into an amorphous material or glass. b) Relative change of viscosity of PS normalized by viscosity at T_M = 490 K against 1/T for different molecular weights between: 134000-25000 (curve 1), 13500-11000 (curve 2), 7400 (curve 3), 5100 (curve 4) and 4900 g/mol (curve 5), (Adapted from Flory, P.J. et al. [11]).*

Given that the glass transition is not a thermodynamic phase transition, T_g is only empirically defined as the temperature where the liquid becomes too viscous to flow within a reasonable time scale (of the order of days). The viscosity of bulk polymer melts, as they approach T_g, can be obtained using viscometers, in which a shear force is applied on a material (Fig. 1.9).

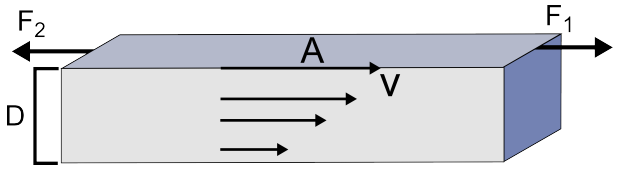

Figure 1.9: *In a shear experiment, a force F_1 is applied to the surface of a material (or liquid). The surface of the material moves at a velocity v as the material is sheared. This shear velocity is measured in order to estimate the viscocity of the material.*

In order to relate the viscosity (η) with the time scale on which the polymer flows, i.e. relaxation time τ, the shear experiments is described as follows. First, the viscous force (F_2), opposite to the shear (F_1), is proportional to: velocity (v) of the sheared surface and its area (A). On the other hand, F_2 is inversely proportional to the thickness (D) of the slab of material that is sheared. Altogether, this can be written as (eq.1.12):

$$F_2 = \eta \frac{vA}{D} \tag{1.12}$$

The shear velocity (v) can be considered as a small displacement of the surface (Δ x) within a certain relaxation time (τ) in reaction to the applied stress ($\sigma = F_1/A$). Assuming that equilibrium has been reached (F_1=F_2), equation (1.12) is rewritten as:

$$\sigma = \frac{\eta}{D}\frac{\Delta x}{\tau} \tag{1.13}$$

Given that the relative deformation of the system is $\xi = \Delta x/D$, then equation (1.13) reads:

$$G = \frac{\eta}{\tau} \tag{1.14}$$

where G is defined as the shear modulus $G = \sigma/\xi$. From this simple model, a direct relationship between viscosity (η) and relaxation time (τ) is demonstrated ($\eta = G\tau$). As seen from experiments, viscosity, and therefore relaxations times, are a function of temperature, increasing dramatically as the temperature is reduced towards T_g (Fig. 1.8b). Although shear experiments are relatively easy to perform, great efforts have been made to learn how relaxation processes occur on the molecular level, and whether this can be related to what is seen in shear

experiments. Polymers have many degrees of freedom which are indistinguishable using classical viscometer experiments. Such degrees of freedom can be for example, segmental motions of the chain, rotation of molecular groups along the chain, reptation and end-to-end distance variations. A widely used method to isolate the different dynamic motions of a polymer chain is broadband dielectric spectroscopy.

1.1.4 Broadband Dielectric Spectroscopy

Broadband dielectric spectroscopy (BDS) is used to probe the electric response of a material by placing it between two conductive electrode plates. Within this setup a voltage is applied between the electrodes and the capacitive current is measured in order to obtain the materials dielectric response function, either in the time or frequency domain (Fig. 1.10a). The term *broadband* comes from the wide frequency range that these instruments can sweep, typically around 12 frequency decades. For polymer materials, the dielectric response originates from reorientation of permanent dipole moments distributed along the chain (Fig. 1.10b-c).

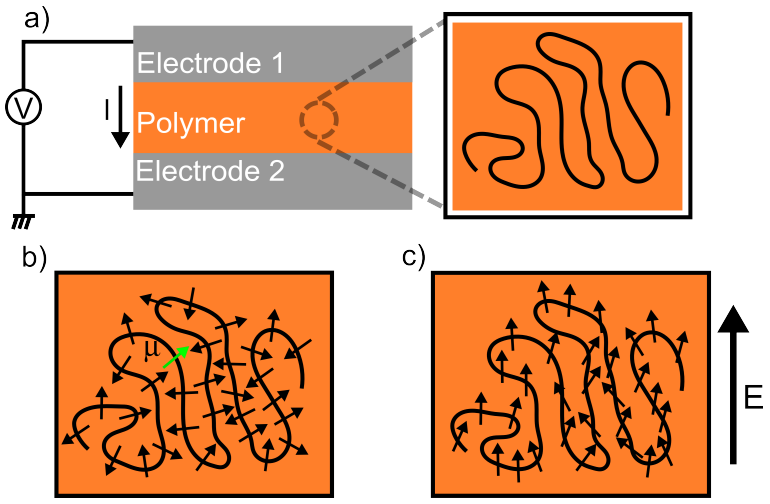

Figure 1.10: *a) A basic picture of dielectric spectroscopy for a polymer material.b) A polymer chain with a collection of equal permanent dipoles, with a moment μ, distributed along the chain backbone. c) Dipoles reorient in order to follow the external applied field (E) if the chain, or parts of it, are able to move.*

The response function of the system is the complex dielectric function (ϵ^*), which relates the external field (E), generated by the applied voltage, and the polarization ($\vec{P}$) of the sample:

$$\vec{P} = \epsilon_0(\epsilon^* - 1)\vec{E} \tag{1.15}$$

In order to simplify expressions, it is convenient to introduce the *Displacement* vector ($\vec{D}$), which is the sum of charges generated by the field and the polarization ($\vec{P}$) of the material:

$$\vec{D} = \epsilon_0 \vec{E} + \vec{P} \tag{1.16}$$

Combining this equation with 1.15 gives,

$$\vec{D} = \epsilon_0 \epsilon^*(\omega) E \tag{1.17}$$

In this way, the displacement vector is directly proportional to the dielectric function and the external field.

Total polarization of a polymer sample is induced by several processes that occur within a wide range of times scales. Such processes include the diffusion of ions (>10 seconds), reorientation of dipole moments (100-10^{-9} seconds), vibrations of atomic bonds (10^{-12} seconds) and charge separation within electronic clouds of single atoms (10^{-15} seconds). Given the electronic limitations of dielectric spectroscopy, the technique covers ions diffusion (>0.01-10 Hz) and reorientation of permanent dipoles (<1 MHz). All faster processes require complimentary techniques which allow higher time resolution, such as infrared spectroscopy. [12, p.35]

For polymers, reorientation of permanent dipole moments give rise to changes in polarization which in turn are proportional to changes in the displacement vector. Dipolar motion in polymers depend on how free the chain is to move and adjust to external fields. Therefore such reorientations are dependent on temperature. Below T_g, the chain is not able to readjust to the external field in reasonable time scales (in the order of hours). Above T_g, the chain is able to move, giving the dipole moments the possibility of reorienting along the external field.

In order to study the relaxation time in which such reorientation of dipoles occur within a double plate capacitor setup, either a voltage step can be applied and the transient current within the capacitor is measured (time domain), or an alternating applied voltage $V = V(\omega)\exp(i\omega t)$ can be swept in frequency (frequency domain) and the resulting capacitive current ($I = I(\omega)\exp(i\omega t + \phi)$) is measured. Here, ϕ is the phase lag between voltage and current. In the frequency domain the complex capacitance of the system is:

$$C(\omega) = \frac{I}{dV/dt} = \frac{I(\omega)}{i\omega V(\omega)} e^{i\phi} \tag{1.18}$$

The capacitance of a double plate system is proportional to complex dielectric function of the dielectric material ($C = C_0 \epsilon^*$) between the plates, where C_0 is the

capacitance without dielectric filling. Using this, equation 1.18 reads:

$$\epsilon^* = \frac{I(\omega)}{i\omega C_0 V(\omega)} e^{i(\phi)} \tag{1.19}$$

The complex dielectric function for a polymer material depends on temperature and frequency: $\epsilon^*(\omega, T) = \epsilon_1(\omega, T) + i\epsilon_2(\omega, T)$. By using this relation in equation 1.19:

$$\epsilon_1(\omega, T) + i\epsilon_2(\omega, T) = \frac{I_0}{\omega C_0 V_0} e^{i(\phi - \pi/2)} \tag{1.20}$$

and by defining $\delta = \phi - \pi/2$, equation 1.20 is separated into real and imaginary parts:

$$\epsilon_1(\omega, T) = \frac{I(\omega)}{\omega C_0 V(\omega)} \cos(\delta) \tag{1.21}$$

$$\epsilon_2(\omega, T) = \frac{I(\omega)}{\omega C_0 V(\omega)} \sin(\delta) \tag{1.22}$$

where ϵ_1 is called the storage function and ϵ_2 loss function. In such experiments the relevant measurements are the material's impedance (Z(ω)=V(ω)/I(ω)) and phase lag (ϕ) between the applied voltage and circulating current. An important definition in the frequency domain is the loss tangent function which is defined as the ratio of loss to storage function (Eq.1.23).

$$\tan\delta = \frac{\epsilon_2}{\epsilon_1} \tag{1.23}$$

Dipolar motion, or relaxation, gives information of the different dynamical motions in a polymer chain. Such relaxation processes are measured through the complex dielectric function described earlier. In order to have a notion of what a dielectric spectrum looks like, the ***Debye model*** is introduced. This model was first developed to describe a polar liquid, where a collection of equal non-interacting dipole moments are distributed within a liquid (Fig. 1.11) and are set to interact with and external electric field (E).

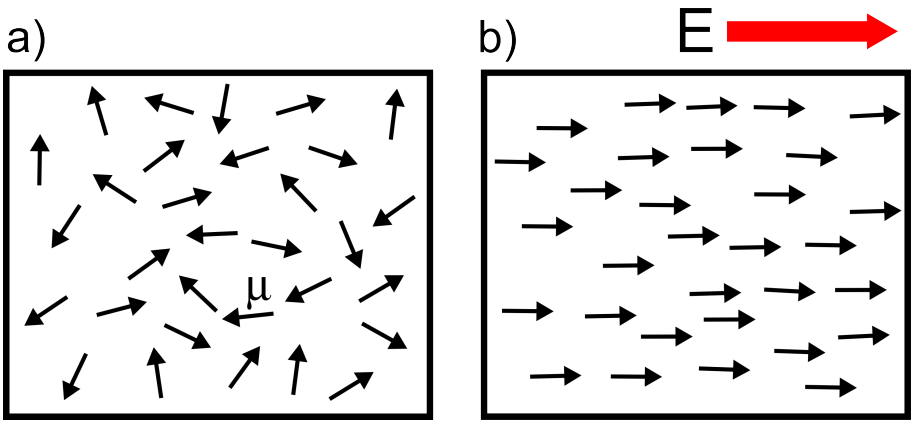

Figure 1.11: *a) A collection of disordered dipole moments. b) At a certain moment an electric field is applied. The dipole moment reorient within a certain time to this external field.*

The Debye model considers that the rate of change of the displacement vector is proportional to its difference with its final value ($\vec{D_f}$). This change occurs within the time scale of the relaxation time τ. Given that for a double plate capacitor the field lines are all perpendicular to the surface of the plates, vector notation can be dropped and the temporal evolution of the displacement vector reads:

$$\frac{dD}{dt} = -\frac{1}{\tau}\left(D - D_f\right) \tag{1.24}$$

In the frequency domain, equation 1.24 is used, considering a complex dielectric constant $\epsilon^*(\omega)$ and an external alternating field $E = E_0 e^{i\omega t}$. By replacing these terms in the *Debye model* and considering $D = \epsilon_0 \epsilon^*(\omega) E$ with a final displacement field given by $D_f = \epsilon_0 \epsilon_f E$, where ϵ_f is a constant, the following frequency dependent complex dielectric function is obtained:

$$\epsilon^*(\omega) = \frac{\epsilon_f}{1 + i\omega\tau} + \epsilon_\infty \tag{1.25}$$

The Debye model accounts only for dipole rearrangements, reason for which an ϵ_∞ term is added to equation (1.25), to include high frequency processes. In order

to find ϵ_f, a slow frequency dielectric constant ϵ_s is defined. For slow frequencies ($\omega \to 0$) equation 1.25 gives: $\epsilon_s = \epsilon_\infty + \epsilon_f$. This means, $\epsilon_f = \epsilon_s - \epsilon_\infty$, which is defined as the dielectric strength $\Delta\epsilon$. Using this relation, the complex dielectric constant in the frequency domain is rewritten as:

$$\epsilon^*(\omega) = \frac{\Delta\epsilon}{1 + i\omega\tau} + \epsilon_\infty \tag{1.26}$$

Such a solution considers a single relaxation time (τ). By separating the real and imaginary parts of this complex function the dielectric storage (ϵ_1) and loss function (ϵ_2) are obtained. These are plotted in figure 1.12a) and give the reader a general idea of what a dielectric spectrum looks like.

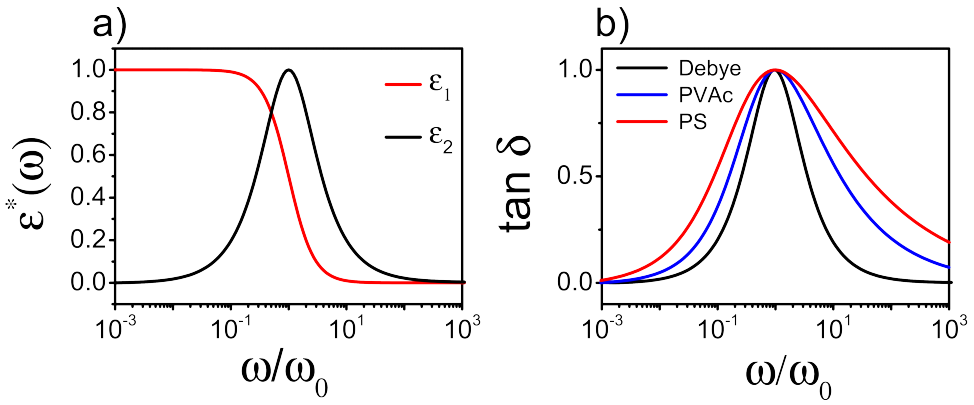

Figure 1.12: *a) Real and imaginary part of the complex dielectric function for a single relaxation Debye model. b) Normalized loss tangent (tan δ=ϵ_2/ϵ_1) for real polymers compared to the single relaxation time Debye model.*

The position of the maximum of loss functions gives the relaxation time of the dipoles within the polymer, in other words, how fast they can react to an external field. The position of the peak (ϵ_2) shifts to higher frequencies with increasing sample temperature. This peak is usually called the ***α-relaxation processes*** and is related to segmental motion of the polymer chain.

In figure (1.12b) loss tangent functions (tan $\delta = \epsilon_2/\epsilon_1$) are shown for real polymers, such as Polystyrene (PS) and Polyvinylacetate (PVAc), and compared to a single Debye process. As seen from this figure, the Debye model, although successful in qualitatively interpreting data, fails to fit real spectra, which are broader and asymmetric. [12, p.94]

Empirical models have been developed in order to fit such broadened and asymmetric spectra. A commonly used model to fit polymer dielectric spectra is the

Havriliak-Negami function (Eq. 1.27), which is a modified version of equation 1.26:

$$\epsilon^*(\omega) = \frac{\Delta\epsilon}{[1 + (i\omega\tau_{HN})^m]^n} + \epsilon_\infty \tag{1.27}$$

where m and n are shape parameters that control the symmetric (m) and asymmetric ($m \cdot n$) broadening of the peak. The frequency at the maximum (ω_{max}) is related to the relaxation time (τ_{HN}) by:

$$\omega_{max} = \frac{1}{\tau_{HN}} \left[\frac{\sin(\frac{\pi m}{(2+2n)})}{\sin(\pi \frac{mn}{(2+2n)})} \right]^{1/m} \tag{1.28}$$

and the relaxation time at the maximum can be calculated given $\omega_{max} = 2\pi\tau_{max}$. From such fits, the temperature dependence of the relaxation time can be investigated ($\tau_{max}(T)$). The notation ***max*** is dropped from hereon, given that all relaxation times shown in further chapters are the relaxation at the maximum ($\tau \equiv \tau_{max}$). In order to fit temperature dependent relaxation times for the α-process, the Vogel-Fulcher-Tammann (VFT) equation is used:

$$\tau = \tau_0 e^{\frac{B}{T - T_0}} \tag{1.29}$$

where τ_0 is the relaxation time at high temperatures ($\tau_0 \sim 10^{-13}$ Hz), B is called the activation parameter, and T_0 is called the ideal glass transition temperature of the system. Relaxation versus temperature plots, with corresponding VFT fits, are shown in the next section (Fig. 1.18). Given that there is no signature of a glass transition in relaxation time versus temperature plots, the glass transition temperature can only be defined by complimentary experiments, e.g. specific volume or differential scanning calorimetry (DSC). By comparing the glass transition temperature obtained in specific volume or DSC measurements with BDS, the relaxation time at the glass transition temperature is by definition $\tau(\mathrm{T}_g) =$ 100 s. The main advantage of extrapolating the T_g from relaxation plots using VFT fits, is that the T_g is not dependent on cooling rates, since relaxation data is obtained from a series of experiments at constant temperature.

Although Havriliak-Negami functions model dielectric peaks arising from dipolar motion, it is an empirical function and the physical nature of broadening spectra is still a matter of debate. One of the most popular explanations is that broadened dielectric spectra are due to spatial and temporal ***heterogeneities*** within the probed volume of the material. Heterogeneities consist of mesoscopic regions within the sampled volume that have different relaxation times. Broadening of tanδ spectra are attributed to measuring a distribution of different Debye relaxations processes within the volume, which are averaged out by the double plate capacitor. Although recent experimental evidence have been found that support

heterogeneities for small molecules [13], single Debye relaxation regions have not yet been measured in polymer materials. The main difficulty has been that such single relaxation regions are not long lived and are believed to be small ($\sim$ 3 nm). [14]

The small length scales on which spatial heterogeneities may be distinguishable, motivated the first groups to combine Scanning Probe Microscopy (SPM) with dielectric relaxations experiments in order to probe small volumes of material. [15] More details over how to combine SPM with dielectric spectroscopy, or local dielectric spectroscopy (Local-DS), shall be given in chapter 2.

Although Local-DS has not been successful in unveiling underlying spatial and temporal heterogeneities within polymer materials, it remains a promising technique given the possibility of combining spectroscopy with the imaging capabilities of SPM. Within chapter 4, this technique is applied on a miscible polymer blend. It is shown that this technique can be used in order to measure variations in local composition and relate them with topographical information.

1.1.5 Polymer Blends

Polymer blends are materials composed of different polymer species that are mixed together. When the mixture is uniform and the polymers are intermixed down to a molecular level, the blend is called homogenous and the polymers are *miscible*. On the other hand polymer blends that do not form a homogeneous mixture, but phase separate into regions of different species, are called *immiscible*.

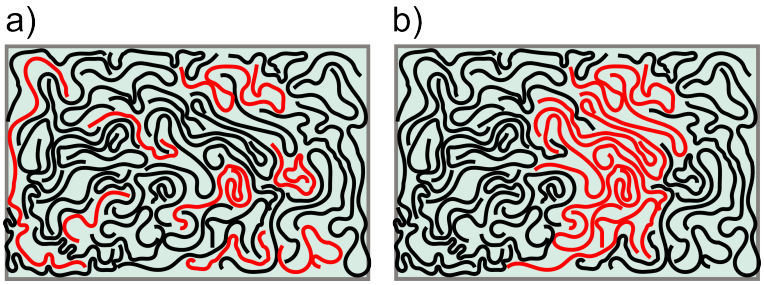

Figure 1.13: *a) Miscible binary polymer blend. b) Immiscible binary polymer blend.*

The miscibility of a polymer blend depends on the volume fraction, temperature and interactions between its components. Although blends can be made out of several polymers, in this work only two component mixtures are used. Therefore from hereon the term polymer blend refers only to the mixture of two polymers species. The majority of polymers are immiscible, this means that when mixed, individual species tend to phase separate. This reflects the fact that in most cases, the interaction of a polymer molecules with its own species is more favorable than with the other one.

A widely used way to model polymer blends is the Flory-Higgins equation (eq. 1.30), which describes the thermodynamic process of mixing of a blend as a function of the occupied fraction volume (ϕ), temperature (T) and an interaction parameter (χ). The Flory-Higgins equation is derived from a lattice model [16, p.137], in which polymer chains are allowed to occupy n positions within the lattice and N_A (N_B) is the number of positions occupied by a single molecule of the the species A (B). The change in *Helmholtz free energy* (F), from a phase separated regime to a homogeneous mix of polymers A and B is:

$$\begin{aligned} \Delta\bar{F}_{mix} &= \Delta\bar{U}_{mix} - T\Delta\bar{S}_{mix} \\ &= k_B T \left[\frac{\phi}{N_A} \ln\phi + \frac{1-\phi}{N_B} \ln(1-\phi) + \chi\phi(1-\phi) \right] \end{aligned} \tag{1.30}$$

where k_B is the Boltzmann constant and the change in Helmholtz free energy is defined per lattice site: ($\Delta \bar{F}_{mix} = \Delta F_{mix}/n$). The interaction parameter χ is:

$$\chi = \frac{z}{2}\frac{(2u_{ab} - u_{aa} - u_{bb})}{kT} \tag{1.31}$$

with u_{ab}, u_{aa} and u_{bb} the interaction energies between lattice sites occupied by different polymer species (A or B), and z the number of lattice nearest neighbors, i.e. for a square 2-dimensional lattice $z = 4$. The value of the interaction parameter depends on temperature. The interaction parameter (χ) is of importance because it gives information of the miscibility of the system at a certain temperature and volume fraction of composing species. A miscible blend has a $\chi < 0$, typically close to zero. Immiscible blends, on the other hand, have an interaction parameter $\chi > 0$.

In equilibrium, polymer mixtures try to minimize their free energy. For homogeneous mixtures (miscible), two major scenarios are distinguishable when plotting free energy versus volume fraction: locally concave (Fig. 1.14a) and locally convex (Fig. 1.14b) regions. When the curve is locally concave, a homogeneous mixture can lower its energy (F_{mix}) by phase separating into two phases (α, β). The energy of the phase separated mixture is $F_{\alpha\beta}$ with a composition ϕ_0. For locally convex curves, phase separated regions will always have a greater free energy ($F_{\alpha\beta}$) than the homogeneous mixture (F_{mix}), therefore mixing of the phase separated region is energetically favorable.

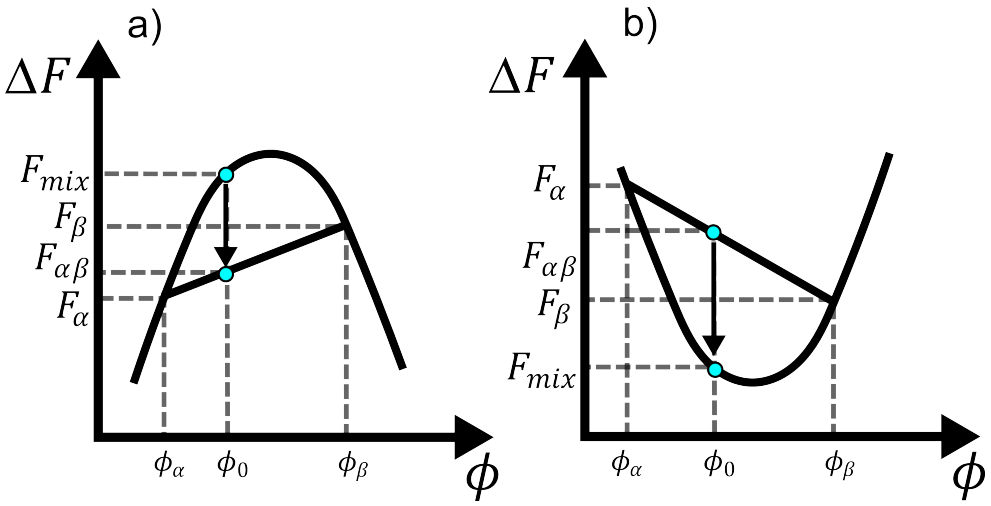

Figure 1.14: *a) Concave free energy: A homogeneous mixture (cyan circle) can lower its free energy from F_{mix} to $F_{\alpha\beta}$ by phase separating into two regions with different energies (F_α, F_β) and volume fractions (ϕ_α,ϕ_β). b) Convex free energy: A phase separated mixture (cyan circle) with energy ($F_{\alpha\beta}$), composed of two region (ϕ_α, ϕ_β) can lower its energy by mixing to F_{mix} with a volume fraction ϕ_0.*

When plotting the Flory-Huggins equation as a function of composition (ϕ) the appearance of concave or convex features in the free energy depends on temperature. The symmetry of such curves also depends on the differences between chain lengths. In figure 1.15(a), the free energy for two polymers with $N_A = 100$ and $N_B = 200$ are shown as the temperature is varied. For high temperatures, the curve is always convex, therefore mixing is always favored. As temperature is lowered, local concave maximums arise, this means phase separation is possible depending on volume fraction.

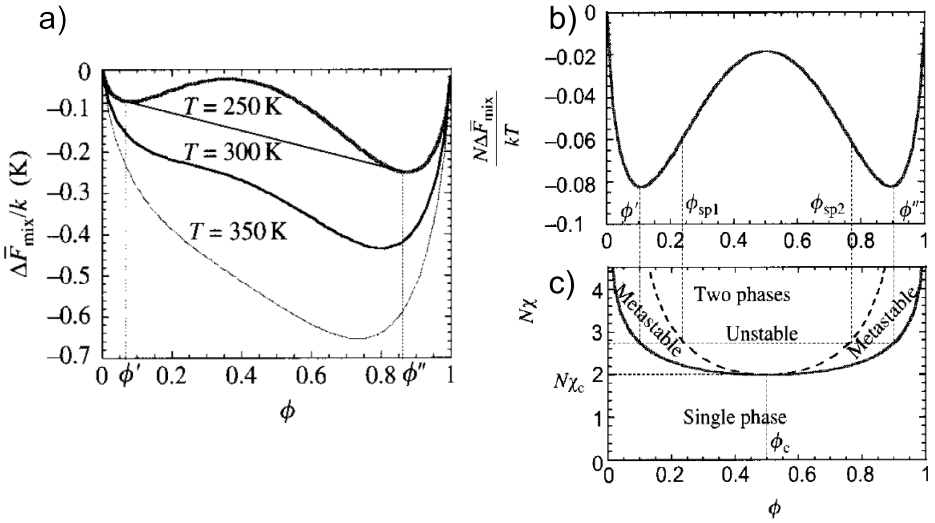

Figure 1.15: *a) Flory-Huggins equation as a function of composition (ϕ) for an interaction parameter χ=5 (K)/T. (Adapted from [16, p.149]) b) Free energy of mixing and c) phase diagram for a polymer blend of equal length chains. (Adapted from [16, p.151])*

Stability in polymer blends is analyzed from the energy minima ($\partial\bar{F}_{mix}/\partial\phi$=0), curvatures ($\partial^2\bar{F}_{mix}/\partial\phi^2 > 0$ or $\partial^2\bar{F}_{mix}/\partial\phi^2 < 0$) and the inflection points of such curves ($\partial^2\bar{F}_{mix}/\partial\phi^2 = 0$). In figure 1.15(b) the free energy is shown for a polymer blend with equal chain lengths. Equal chain lengths produce a symmetrical curve. By connecting the local minima (ϕ' and ϕ''), the interaction parameter (χ) for the binodal phase boundary is obtained (solid line fig.1.15c). The binodal curve separates one phase mixtures (homogeneous) from two phase mixtures (phase separation). Although the free energy is in general lowered by phase separation between local minima (ϕ' and ϕ''), there is a region between the minima and the inflection points ($\partial^2\bar{F}_{mix}/\partial\phi^2 = 0$), where homogeneous mixtures are possible. The inflection points of the curve defines the spinodal curve (dashed line fig.1.15c). Between the binodal and spinodal curves, metastable homogeneous mixtures are found, this means large fluctuations in volume fraction are required

in order for the homogeneous mixture to phase separate.

In general, polymers tend to avoid mixing homogeneously and usually try to phase separate by clustering or crystallizing. A way of testing experimentally blend homogeneity is using differential scanning calorimetry (DSC). In this experiment, two samples are heated at a same rate. One sample is the polymer and the other sample is a calibration material which has a constant heat capacity over a wide range of temperatures. The polymer and calibration sample are heated at the constant rate and the heat flux needed to achieve a constant heating rate for each sample is measured. Any difference in heat flux between polymer and reference sample has to be due to some additional endo- or exothermic process in the polymer. Therefore, DSC gives information over the glass transition temperature, crystallization or melting of the system. Some common features (or transitions) seen with DSC are depicted in figure (1.16).

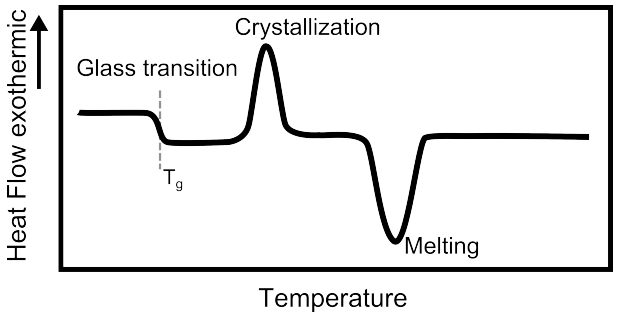

Figure 1.16: *Differential Scanning Calorimetry curves showing common features of polymers such as glass transitions, crystallization and melting.*

In order for a polymer blend to be miscible, no crystallization features are expected in DSC scans. When a crystal peak appears, it means that one of the components has clustered partially crystallized, forming i.e. lamellar structures.

Typically the glass transition of a polymer is shifted several degrees when mixed with another polymer. Shifts in T_g due to blending are commonly used in industrial applications in order to tune the material's properties. In order to estimate the effective glass transition (T_g) of a polymer blend with components A and B, a commonly used empirical expression is the Fox equation:

$$\frac{1}{T_g} = \frac{\phi}{T_g^A} + \frac{1-\phi}{T_g^B} \tag{1.32}$$

where ϕ is the volume fraction of the polymer A and T_g^A and T_g^B is the glass transition temperatures of the pure homopolymers. Another recently developed

model to describe polymer blends, is the self-concentration Lodge-McLeish model (LM) [17]. In this model, the average effective composition (ϕ_{eff}) around a local environment of the polymer chain is enriched in the same species by:

$$\phi_{eff,i} = \phi_{S,i} + (1 - \phi_{S,i}) \langle \phi \rangle \tag{1.33}$$

where i indicates the components A or B, $\langle \phi \rangle$ is the average composition of the blend and $\phi_{S,i}$ is the self concentration of the component i. In this model the relevant length scale is of the order of the Kuhn length (l_K). The self concentration (ϕ_S) is the volume fraction occupied by the monomers inside one Kuhn length in a volume $V_K = l_k^3$:

$$\phi_S = \frac{C_\infty M_0}{k \rho N_{Avo} V_K} \tag{1.34}$$

where C_∞ is the characteristic ratio, M_0 the molar mass of the repeat unit, ρ the density, k the number of backbone atoms per repeat unit and N_{Avo} the Avogadro number. The macroscopic glass transition of the polymer is then written as a modified Fox equation using the effective concentration:

$$\frac{1}{T_g(\phi_{eff})} = \frac{\phi_{eff}}{T_g^A} + \frac{1 - \phi_{eff}}{T_g^B} \tag{1.35}$$

A polymer blend that will be studied throughout this work is the blend of polyvinylacetate with polyethylene oxide (PVAc/PEO)(Fig.1.17a-b). Such a blend is miscible within enriched PVAc blending ratios (Fig. 1.17c).

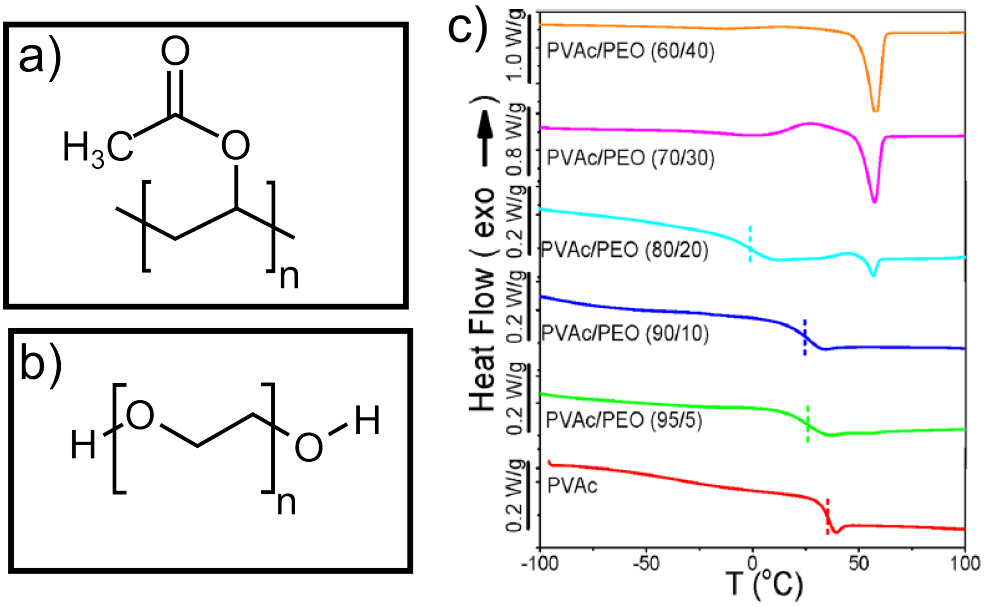

Figure 1.17: *Chemical structures of a) polyvinylacetate (PVAc) and b) polyethylene oxide (PEO). c) Differential Scanning Calorimetry for PVAc/PEO blends. (Adapted from [18]).*

For enriched PVAc blending ratios, the T_g of PVAc is lowered with increasing concentrations of PEO. This is seen up to ratios of PVAc/PEO 80/20 (4 buttom curves Fig. 1.17c). For PVAc/PEO 80/20 a crystal melting peak is observed, indicating the onset of phase separation. For higher concentrations of PEO the melting peak grows, which means that for blending ratios $\geq$20% PEO, phase separation takes place (3 top curves Fig. 1.17c).

It is of interest to study dynamics within miscible polymer blends because, even though both polymers species are intermixed down to a molecular level, the movement of both chains are still distinguishable. Dual dynamics in miscible blends is called ***dynamic heterogeneity*** and can be observed using BDS. [19] Furthermore, the dynamics of the different components are affected by each other. This means, the faster moving chain produces faster segmental dynamics in the slower component, and the slower one reduces the segmental dynamics of the faster chain. This effect is more pronounced if difference between glass transition temperatures of the composing homopolymers is large (Δ $T_g \sim$ 100 K). In the case of PVAc/PEO blends, PEO has a greater mobility than PVAc chains within the blend (Δ $T_g \sim$ 100 K). This produces a shift towards faster segmental dynamics, or relaxation times, of the PVAc chains. Such effect is shown figure 1.18, where maximum relaxation times are obtained using BDS for: pure PVAc, PVAc/PEO 95/5 , PVAc/PEO 90/10 and PVAc/PEO 80/20, are plotted as a function of inverse temperature (1000/T). Furthermore this plot shows the relaxation times for bulk PEO.

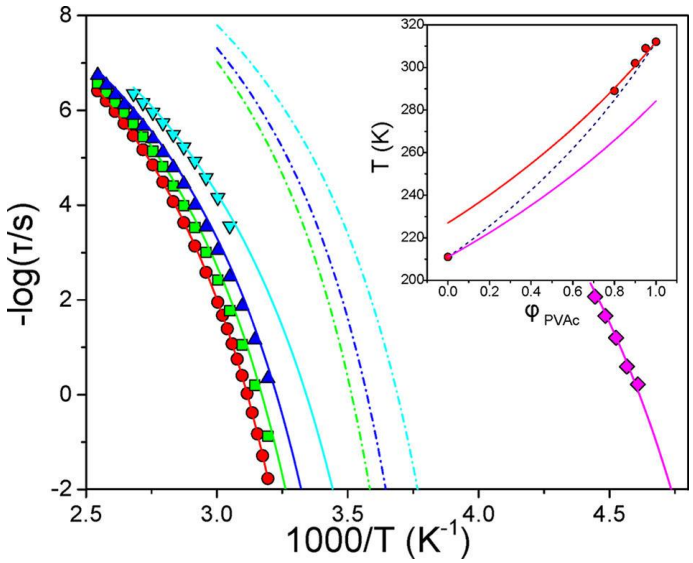

Figure 1.18: *Relaxation map obtained using BDS for: pure PVAc (red circles), PEO (pink rhombi) and PVAc/PEO blends of 95/5 (green squares), 90/10 (blue triangles) and 80/20 (cyan triangles) composition. Solid red and pink lines represent VFT fits for PVAc and PEO respectively. Solid lines for the blends represent fits using the LM model. Dashed dot lines represent the PEO relaxation times simulated with the LM model (the same color code applies). Inset shows the extrapolated T_g for the different blend compositions (red circles) plotted together with the LM model (solid lines) for each polymer species and Fox equation (dashed line).(Adapted from [18]).*

Relaxation times for pure bulk PVAc and PEO data are fitted using the VFT model (red and pink solid lines Fig.1.18). For blended samples, the shifted α-relaxation times of PVAc is fitted by modifying the VFT fit with the LM model. In order to do so, parameters B and τ_0 of the VFT equation are fixed at homopolymer value, and the ideal glass temperature (T_0) is modified by the LM model, which becomes a function of the composition ($T_{0,i}(\phi_{eff})$):

$$T_{0,i}(\phi_{eff}) = T_{0,i} + (T_{g,i}(\phi_{eff}) - T_{g,i}) \tag{1.36}$$

Here $T_{0,i}$ and $T_{g,i}$ are the ideal glass and glass transition temperatures of the homopolymers. On the other hand $T_g(\phi_{eff})$ is given by the LM-modified Fox equation (Eq. 1.35). VFT fits using the LM model are shown as solid green blue and cyan lines for the PVAc shifted peak (Fig.1.18) and the predicitons for the PEO shifted peak for the same corresponding concentration are shown as dashed dot lines using the same color code. The PEO α-relaxation process is not observed in such experiments due its low dielectric strength. The inset of figure (1.18) shows the extrapolated T_g for pure PVAc and the blends (solid points) as a function of PVAc concentration (φ_{PVAc}). Solid and dashed lines of the inset represent the LM model and Fox equations respectively.

Another effect of dynamic heterogeneity in polymer blends is that the peak broadens with increasing mixing ratio, in the case of miscible PVAc/PEO, the increase of PEO concentration broadens the α-relaxation peak for PVAc. This process can be explained by theories that involve fluctuations of local concentration within small volumes within the blend. [20]

In this work results regarding the study of PVAc/PEO miscible blends using local-DS are shown (Chapter 4). The motivation for studying such blends was initially to probe the effects of dynamic heterogeneity within small nanoscale volumes. But, as shall be shown, it is also of interest to study phase separation in such blends by combining local-DS with the imaging capabilities of AFM.

1.2 Colloids and Colloidal Particles

Colloids are defined as systems where particles are suspended within a medium that surrounds them (Fig. 1.1). The lengths scales of colloidal particles which are considered to form colloids is referred to as the colloidal domain and spans dimensions that go from 10 nm up to $\sim$10 μm. Possible dispersing mediums for colloidal particles can be a liquid, gas or a solid. The suspended colloidal particles within the medium can be liquid droplets, solid particles or gaseous bubbles. Depending on the nature of the particle and the medium, colloids are defined as: aerosols (liquid or solid particles within a gas), foams (gas bubbles within a liquid or solid), emulsions (liquid droplets within another liquid or solid) and sols (solid particles within a liquid or solid).

Colloidal systems have great relevance within industrial applications, like dispersion paints, but are also used in basic research as model systems to simulate atoms within a crystals or glasses. [21, 22] Interactions of the colloidal particles with each other and the medium in which they are dispersed control their macroscopic physical properties. Such interactions can be tuned by modifying the colloids, i.e. by changing their surface chemistry, introducing charged groups or attaching polymer chains. Further possibilities to control the interaction of charged colloids is the addition of ions within the dispersing solution.

Over recent years attention has been growing on not only controlling colloidal particle interactions, but also their shape. It is currently accepted that particle shape is relevant in the interaction of colloidal particles with biological samples. [23] Although the relevance of shape is widely regarded as a control parameter for tuning colloidal interactions, methods to produce large quantities of anisometric solid particles have not been reported until now.

In a recent publication, Friedemann *et al.* [24], reported a method to produce, in a facile way, large quantities of micron-sized colloidal particles made of silica (SiO_2). The main achievement of this work is that such colloidal particles are not spherical, but highly anisometric (Figure 1.19a).

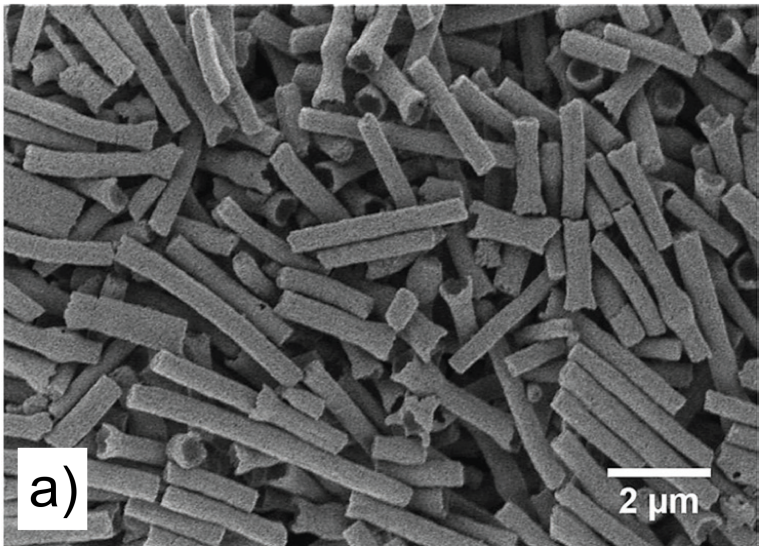

Figure 1.19: *a) Large quantity production of anisometric silica particles. (Adapted from [24]).*

Such particles are produced by an electrospnning procedure. Electrospinning is a technique where a syringe containing a polymer solution is used. The gap between the syringe and substrate is biased with a high electric voltage. Such a voltage produces a jet of polymer solution that accelerates towards the substrate sample. Using electrospinning, thin polymer fibers ($\sim$ 100 nm) are drawn from a solution (Figure 1.20 a))

In order to produce the final anisometric particles, the polymer solution is filled with silica (SiO_2) particles of 20 nm diameter, and a smaller amount of polystyrene (PS) particles of defined size, which can range between 60 nm - 600 nm. The polymer within the solution is polyvinylalcohol (PVA). After electrospinning, a final fiber containing densely packed silica nanoparticles in a PVA matrix with randomly distributed PS particles is obtained (Fig. 1.20b)). After a sintering step at 873 K the PVA matrix and PS particles are burned off, leaving behind sintered silica particles with voids where the PS particles had been. In a final step, such fibers are put in an ultrasonic bath. Given that there are voids of controllable sizes, the fibers are ruptured presumably at the void position by sonication. After sonication a rod-like anisometric silica particle is obtained (Fig. 1.20c)).

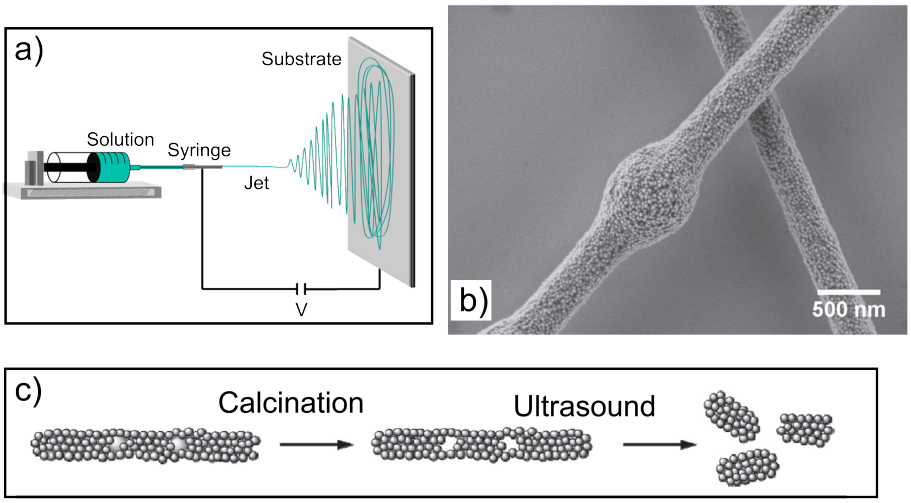

Figure 1.20: *a) Electrospinning technique. b) SEM image of fibers after electrospinning. c) Procedure to obtain anisometric particles.*

Although the production of rod-like colloidal particles after ultrasonication was empirically demonstrated by Friedemann *et al.* [24], the forces involved their production was unclear. In chapter 5 a method to mechanically test sintered silica fibers with voids is developed. Using the force sensing capabilities of SPM, the mechanical properties and rupture forces for these fibers are measured.

1.3 Biominerals

Biomineralization is the process in which living organisms produce skeletal structures from inorganic material. These structures grow aided by their interaction with organic macromolecules, i.e. proteins, molding inorganic minerals into intricate shapes. Scientists still battle to understand and recreate synthetically these types of biomineral structures. An example of an inorganic mineral that is found in many skeletal structures is calcite ($CaCO_3$), which can be synthetically produced (Fig. 1.21a)), but is also found in deep sea sponges (Fig. 1.21b-c). [25] Calcite structures are found in many other living organisms, a beautiful example are Coccoliths found in plankton algae (Fig. 1.21d). [26]

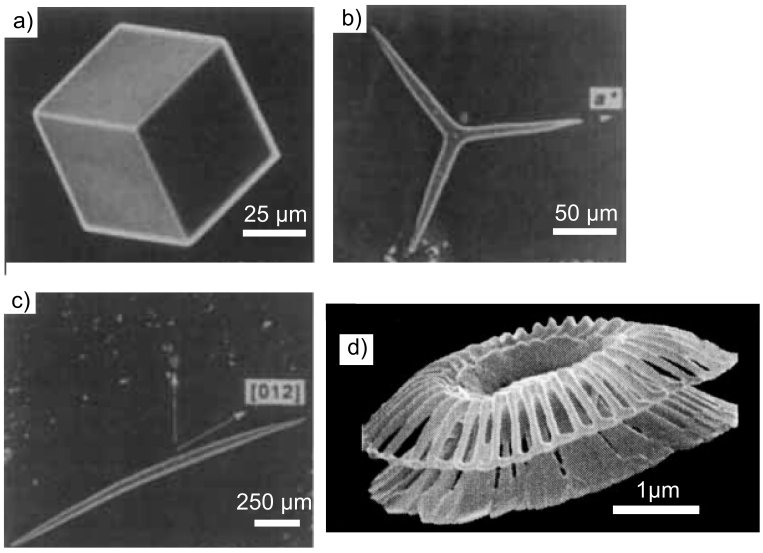

Figure 1.21: *a) Pure calcite crystal. b) Calcereous triradiate from sea sponge "Clathrina contorta" c) Curved monoaxon spicule from "Kebira uteoides" sponge. d) The calcereous Coccolithophorid "Emiliania huxleyi".*

Recent efforts have been made to grow biominerals synthetically, showing great advances in producing minerals with diverse shapes [27]. Furthermore, in a recent publication, Natalio *et al.* , have demonstrated the production of biomimetic calcite spicules. [28] In order to produce such spicules, a protein known in the production of silica spicules was employed (*Silicatein-*α). [31] The final result were synthetic spicules of around 100 μm in length and 5 μm in diameter. The lengths compare well to natural calcite spicules found in the *Sycon* deep sea sponge (Fig. 1.22a-b).

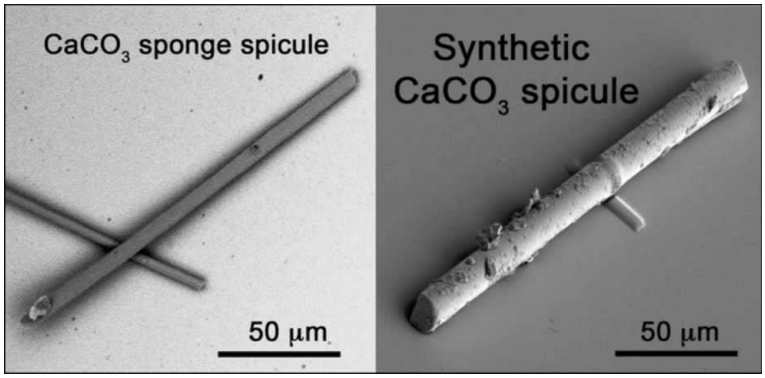

Figure 1.22: *a) Natural calcite spicule from "Sycon" see sponge.b) Sythetic calcite spicule.*

Main characteristics of biominerals is their mesocrystallinity. [29] A mesocrystal is a structure composed of nanocrystals embedded within an amorphous matrix (Fig. 1.1). Although the mesocrystalline structure of biominerals is usually probed with conventional techniques, i.e. x-ray scattering [30], complimentary measurements of their mechanical properties, surface structure and organic content is fundamental in order to build a complete picture of their physical properties.

In Chapter 6, new SPM related methods are shown, which allow the measurement of biomineral properties that cannot be inferred from x-ray scattering or measured with conventional thermal or mechanical testing experiments, e.g. TGA and flexural testing. SPM methods prove to be valuable specially when the size of the biomineral is small (100 μm) or if they cannot be produced in large quantities (>10 mg), which is a requisite for bulk TGA experiments. The properties measured and shown in chapter 6 are the Young's modulus, maximum stress before fracture and the amount of organic content of both individual natural and synthetic spicules. From such measurements a deeper understanding of the mesocrystalline structure of natural and synthetic spicules is reached.

Chapter 2

Measurement Fundamentals

In this chapter the operating principles behind flexural and dielectric measurements employing *scanning probe microscopy* are discussed. First, the working principles behind the operation of a scanning probe microscope are presented (2.1), followed by the basics of *force spectroscopy* used in the mechanical study of colloidal nanofibers and needle-like biominerals (2.2). Afterwords, frequency modulation AFM (FM-AFM) shall be described (2.1.1), which is the basis for local dielectric spectroscopy (2.3), used to study polymer dynamics.

2.1 Scanning Probe Microscopy

Scanning Probe Microscopy (SPM) refers to a family of related techniques in which a probe is scanned across a sample surface in order to obtain certain topographical information from it. The first SPM developed was the Scanning Tunneling Microscope (STM), where an atomically sharp conductive tip is scanned in close proximity to a conductive surface, producing a tunneling current between tip and sample. [32] Shortly after STM, the first Atomic Force Microscopy (AFM) was developed by Bining, Quate and Gerber. [33] AFM was first conceived as a method to obtain topographic information of insulating surfaces. From then on various variations of AFM have appeared, including nearfield scanning optical microscopy (NSOM), Kelvin probe force micrsocopy (KPFM), Electric force miscrospy (EFM), magnetic force microscopy (MFM), friction force microscopy (FFM) and colloidal probe techniques. This family of related instruments is referred to as Scanning Probe Microscopy (SPM).

The main components behind the operations of the simplest SPM, the AFM, are depicted in figure 2.1 (a). The AFM tip (Fig. 2.1 b-c) is generally attached to a silicon micro-beam which acts as a force sensor to detect the interaction of the tip with the surface. The deflection of the silicon beam, or cantilever from hereon, is optically monitored by a laser focused on its backside. Although other

cantilever detection schemes are available, optical detection methods are dominant in commercial setups in air and liquid environments. [34] In this detection scheme, the cantilever reflects the focused laser beam, which is then collected on a *Photodiode detector* (PD). The PD typically used in AFM is a four-quadrant photodetector, composed of 4 photosensitive regions (A,B,C and D). The PD generates a photo-current proportional to the amount of photons collected on each of its region, which is converted into a respective voltage (V_A, V_B, V_C, V_D) by a preamplifier. As the cantilever deforms, the position of the reflected laser spot on the four quadrant PD detector changes accordingly. If the cantilever beam is deformed perpendicular to the surface, this displacement is recorded by the vertical displacement signal coming from the PD: $(V_A + V_B) - (V_C + V_D)$. Torsional movements of the cantilever are proportional to the lateral movements of the laser spot: $(V_A + V_C) - (V_B + V_D)$. Vertical and torsional cantilever deformations yields information over mechanical and frictional properties of the sample.

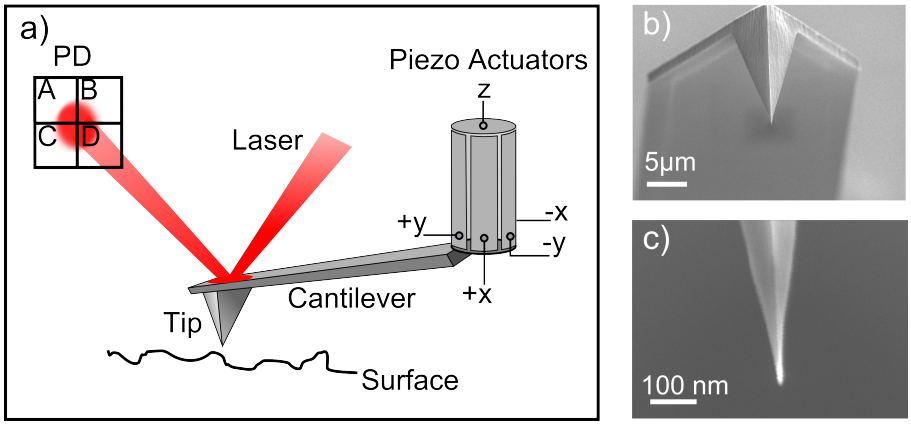

Figure 2.1: *a) Basic components of an AFM. b) SEM images of a commercial cantilever with its respective tip apex and c) a zoom image of the tip. Tip radii of commercial probes range from 5 nm to 50 nm.*

The last basic component in order to operate an AFM are piezoelectric actuators, which are used in order to scan the tip across the surface. Piezoelectricity is the generation of electrical charge within a crystal by mechanical deformation. The most famous piezoelectric crystal is quartz, used in a variety of electrical resonators, e.g. for timing and monitoring films depositions. For AFM applications, piezoelectric scanners are designed in order to move the cantilever across the surface (x-y axis) and control the tip-sample distance (z-axis). Cantilever movements are controlled using the inverse piezo-electric effect, in other words, a voltage is applied to a piezo-crytal in order to deform it. A very common ceramic used in scanning applications, such as AFM, is *Lead Zirconate Titanate* (PZT).

Piezoelectric scanners for AFM come in several geometries, being a usual configuration the tube scanner, where a cylindrical PZT tube is segmented into 4 regions (Fig. 2.1a). Each region is contacted on the tube's exterior with electrodes that apply controlled voltages to each piezo region (+x, -x, +y, -y Fig. 2.1a). By feeding each piezo region with defined voltages, the tube is bent in specific direction, allowing, i.e. x-y scanning. An extra pair PZT piezoelectric elements are placed in the center of the tube to control tip-sample distances (z-piezo). [35] Typical calibration values for PZT actuators are $\sim$ 10 nm per volt bias in the x-y axis and $\sim$ 1 nm per volt of bias in the z-axis.

To image the surface of a sample with any SPM related technique, a tip-sample interaction is required. For instance, in STM, the tunneling current between an atomically sharp tip and a conductive sample surface is used to sense tip-sample distance. Tunneling currents in STM are usually of the order of nanoamperes (nA), and highly dependent on tip sample separation. [36] Such currents only increase within a small range of distances from the sample surface. Therefore, tunneling currents can be used within a feedback loop with the z-piezo in order to keep this tip-sample interaction constant. [37] This means, that as the STM tip scans the surface, the z-piezo moves it towards or away from the surface, in order to keep tunneling current constant. This movement produces the final topographical map. In the case of an atomically flat surface, e.g. highly oriented pyrolytic graphite (HOPG), the STM image represents a map of the density of electronic states of the sample surface. [38, 39] In general, STM images represent a convolution of topographical and electronic states of the surface.

An AFM generates a topographical image by recording the z-piezo displacements required to keep a the tip-sample force constant. Unlike STM, interaction between an AFM tip and a surface (F_{ts}) are a combination of short and long range forces. Such interactions are summarized in a Lennard-Jones type potential ($\phi(z)$) (Fig. 2.2), where the tip-sample force is: $F_{ts} = -d\phi(z)/dz$.

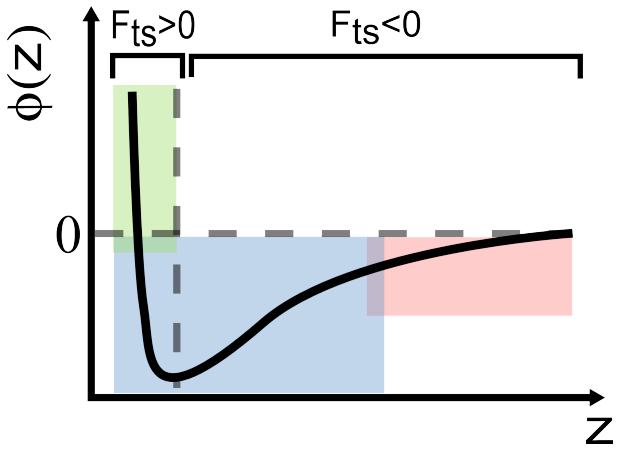

Figure 2.2: *Lennard-Jones potential. Highlighted regions correspond to the operation regimes of 3 major AFM imaging modes: Contact (green), intermittent contact (blue) and non-contact (red).*

Attractive forces may arise from a sum of various effects such as van der Waals forces or, i.e. if a voltage is applied to the tip, by long range electrical forces. Repulsive forces are mainly caused by chemical interactions, utterly controlled by electron cloud interactions which follow Pauli's exclusion principle. By using the Lennard-Jones potential as a generic example, three different AFM imaging modes can be classified: contact, intermittent contact and non-contact modes.

In contact mode, the mechanical contact with the surface ($F_{ts}(z) > 0$ Fig.2.2) is used as the reference setpoint for the z-piezo feedback loop. Mechanical contact with a defined force applied to the tip, produces the deflection of the cantilever, which in turn is measured by the vertical deflection signal in the PD. This imaging mode was the first to be developed and termed *contact mode* (Fig. 2.3). Contact mode is also the basis for force spectroscopy as described in section 2.2.

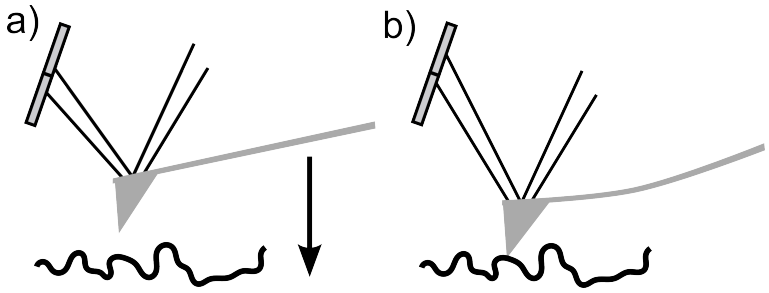

Figure 2.3: *Contact mode AFM. The vertical deflection of the cantilever is used as the reference setpoint. a) the laser spot hits the middle of the PD when far away from the surface. b) When the tip mechanically contacts the surface, the cantilever beam is deformed, making the laser spot move upward on the PD.*

The two other AFM modes, intermittent and non-contact, employ the active oscillation of the cantilever beam to measure attractive and intermittent contact force regimes within the Lennard-Jones potential. Such modes are commonly referred to as *dynamic* imaging modes. Although attractive forces are measurable using soft static cantilevers, dynamic modes are more stable, given that they avoid the jump-in to contact regime (Section 2.2). Furthermore, it is found that dynamic modes are more sensitive to attractive regime forces [40], and allow the sensing of force gradients between tip and sample.

The mechanical motion of a free cantilever (x) is modeled as a forced harmonic oscillator with a damping term (μ). The damping term arises from the interaction of the cantilever with its surrounding environment, e.g. air or liquid. This can be written as:

$$m\ddot{x} = -kx - \mu\dot{x} + F(t) \tag{2.1}$$

where k is the spring constant of the cantilever and $F(t)$ the external force. This equation can be rewritten by introducing the natural frequency of the cantilever $\omega_0^2 = k/m$ and the quality factor of the resonance peak $Q = m\omega_0/\mu$. This way, equation 2.1 reads:

$$\ddot{x} + \frac{\omega_0}{Q}\dot{x} + \omega^2 x = \frac{F(t)}{m} \tag{2.2}$$

If the cantilever is externally driven by $F(t) = F_0 \cos(\omega t)$ and its movement follows the excitation with a certain phase lag $x(t) = x_0(\omega)\cos(\omega t + \varphi)$, then solutions to equation 2.2 are (Eq. 2.4): [41, p.10]

$$x_0(\omega) = \frac{F_0/m}{\sqrt{\omega_0^2\omega^2 + Q(\omega_0^2 - \omega^2)^2}} \tag{2.3}$$

$$\varphi(\omega) = -\arctan\left(\frac{\omega_0\omega}{Q(\omega_0^2 - \omega^2)}\right) \tag{2.4}$$

By introducing an external drive amplitude A_d and using the relation $F_0 = m\omega_0^2 A_d$, equation 2.4 can be written only in terms of ω/ω_0. Furthermore, the amplitude ($x_0(\omega)$) can be normalized by introducing x_{min}, which is defined as the minimum amplitude within frequency sweep. Normalized amplitude ($A = x_0/x_{min}$) and phase (φ) are then plotted as a function of ω/ω_0 (Fig. 2.4) for different damping conditions in which AFMs usually operate: ultra high vacuum (UHV) (Q ~10000), air (Q ~100) and liquid (Q ~5)

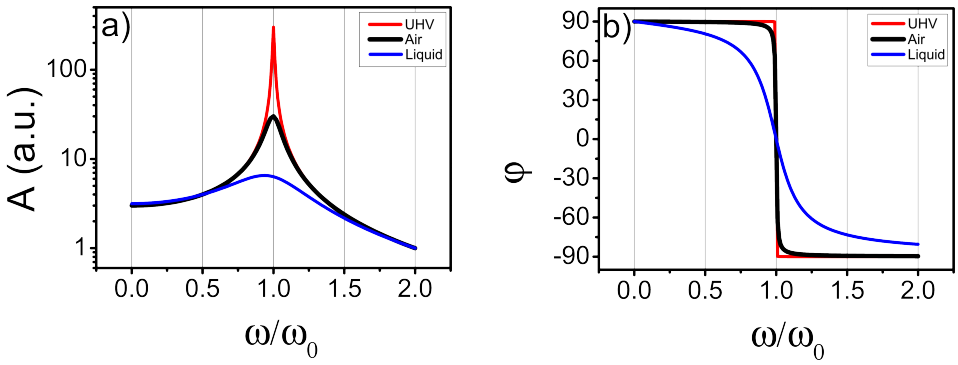

Figure 2.4: *a) Amplitude and b) phase of a driven cantilever for different operating conditions.*

Cantilever vibrations are usually achieved by driving the cantilever holder with an extra piezo stack. The oscillation of the cantilever is then detected as a modulation of the vertical deflection by the PD. The cantilever's resonance peak position and amplitude are sensitive to tip-sample interactions, this is used to operate the AFM in non-contact and intermittent contact modes (Fig. 2.5). In particular, attractive non-contact forces shift the cantilever's resonance peak to lower frequencies. If the tip periodically switches from the attractive to the repulsive regimes, called intermittent contact, the resonance peak shifts its position and its amplitude is damped by the mechanical "tap".

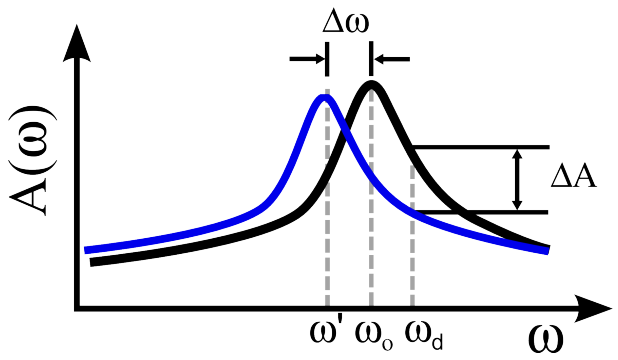

Figure 2.5: *Dynamical modes: In intermittent contact mode the amplitude change is the feedback (ΔA). In non-contact mode the change in peak position is set as feedback ($\Delta\omega = \omega_0 - \omega$).*

In intermittent contact mode, usually termed amplitude modulation AFM (AM-AFM), the vibrating cantilever approaches the surface at a fixed driving frequency ω_d that is slightly off the natural frequency of the cantilever (ω_o). As the tip interacts with the sample, changes in the amplitude of oscillation are measured and used as a feedback (ΔA Fig. 2.5). Intermittent contact modes are widely used in the study of soft matter given the reduced tip-sample interaction and no shear forces which produce surface wear. In intermittent contact mode, the reaction time of a cantilever due to a change in interaction forces is τ=2Q/f, where Q is the quality factor and f the resonance frequency of the cantilever. [42] Therefore, intermittent contact modes are suitable for the low Q conditions such as in liquids or air, but not for UHV conditions.

In non-contact operating modes, changes in the cantilever's resonance frequency, that arise from long range forces, are measured ($\Delta\omega$ Fig. 2.5). [43] This method is called frequency modulation AFM (FM-AFM) (Section 2.1.1). FM-AFM is mostly used in UHV setups because the reaction time is independent of the Q factor (τ=1/f). [42] FM-AFM can also be used in air conditions when long range interactions are present due to electric or magnetic fields. In section 2.3, FM-AFM shall be discussed as a method to measure relaxation dynamics in thin polymer films.

2.1.1 Frequency Modulation-AFM

In frequency modulation AFM (FM-AFM), the cantilever is vibrated at a certain frequency. As the tip interacts with the sample a change in its resonance frequency is produced, as shown in figure 2.5. Such changes in frequency change can be measured using a special electronic amplifier called phase lock loop (PLL). [44, p.428] The change in resonance frequency (Δf) measured with the PLL is used in a feedback-loop with the z-piezo of the AFM in order to image the surface, this is referred to as FM-AFM mode. The frequency of an interacting cantilever can be written as:

$$f = \frac{1}{2\pi}\sqrt{\frac{k^*}{m}} \tag{2.5}$$

where m is the mass of the cantilever (k^*) and its effective spring constant, which includes tip-sample interactions. For an interacting cantilever, it shall be assumed that all changes in the resonance frequency are produced by changes in the effective spring constant ($f \equiv f(k^*)$). By performing a Taylor expansion of equation 2.5 around the non-interacting frequency (f_0) and spring constant k_0, which are related by $4\pi^2 f_0^2 = k_0/m$, then the change in resonance frequency is:

$$\begin{aligned} f &= f_0 + \frac{1}{4\pi m}\sqrt{\frac{m}{k_0}}k^* \\ \Rightarrow \Delta f &= \frac{f_0}{2k_0}k^* \\ \Rightarrow \frac{\Delta f}{f_0} &= \frac{1}{2}\left(\frac{k^*}{k_0}\right) \end{aligned} \tag{2.6}$$

If the non-contact tip-sample interaction is considered to be linear for small displacements around a fixed position ($F = -k^*(z - z_0)$) then:

$$\frac{\Delta f}{f_0} = -\frac{1}{2k_0}\frac{dF}{dz} \tag{2.7}$$

This last result is important because it shows that the changes in resonance frequency (Δf) are proportional to force gradients (dF/dz). It is known that force gradients are usually much higher at the small tip-sample separations than at the larger cantilever sample distances [50], therefore FM-AFM is a preferred method to isolate tip-sample interactions from cantilever contributions. This is relevant for non-contact measurements where long-range forces can be set by applying different biases to the cantilever, e.g. electrical or magnetic. Along this line, the measurement of Δf signals can be used to obtain quantitative dielectric relaxation information of polymer samples as shall be detailed in the section 2.3.

2.2 Force Spectroscopy

Apart from imaging, AFM has gained new terrain in past decades given its force sensing capabilities. AFM probes (cantilever and tip) are versatile tools, which can be used to deform surfaces by pressing against them with AFM tip; and also, measure the adhesion force of a surface by withdrawing the tip from mechanical contact. The main idea behind force spectroscopy is to approach an AFM tip onto a single position of the sample's surface, while measuring the cantilever's vertical deflection as mechanical contact is produced. After this, the tip is retracted until it is left far apart from the surface, where attractive forces are negligible. Such approach and retraction is performed by the z-piezo drive and recorded by the vertical deflection signal of the PD detector. The total force acting on the cantilever obeys a simple Hookean law for small cantilever deflections:

$$F = -k_c\delta \tag{2.8}$$

where k_c is the spring constant of the cantilever and δ its deflection. It is known that the cantilever's spring constant is dependent on the geometry of the lever and the mechanical modulus of the material. [45] Typical spring constants for silicon cantilevers cover values from $\sim$0.01 N/m up to almost 100 N/m. For force spectroscopy, usually soft cantilever are employed ($k_c \leq 1$ N/m). From approach-retract force curves, mechanical and adhesion properties of materials can be extracted. In principle, for an infinitely hard substrate, approach-retract force curves should resemble a Lennard-Jones taking into account $F = -d\phi/dz$.

A raw force versus piezo-movement curve is shown in figure 2.6 for approach (black line) and retraction (red line) of an AFM tip to a surface. Two major regions are identifiable in these curves, the zero force region, where the cantilever senses no interaction force far from the surface, and the constant compliance region, where the tip is being pressed against the sample. Between these two regions, the tip is attracted to the surface ($F_{ts} < 0$). When the force gradients in the attractive region are greater than the spring constant ($dF_{ts}/dz > k_c$) a mechanical instability occurs and the tip is snapped into the constant compliance regime. This mechanical instability is usually called the *jump-in* (black arrow Fig. 2.6). Upon retraction, the tip adheres to the surface requiring a certain force to separate. The moment at which the separation happens is termed *jump-out* of contact (red arrow Fig.2.6). The jump-out force gives information over the adhesion properties of the surface.

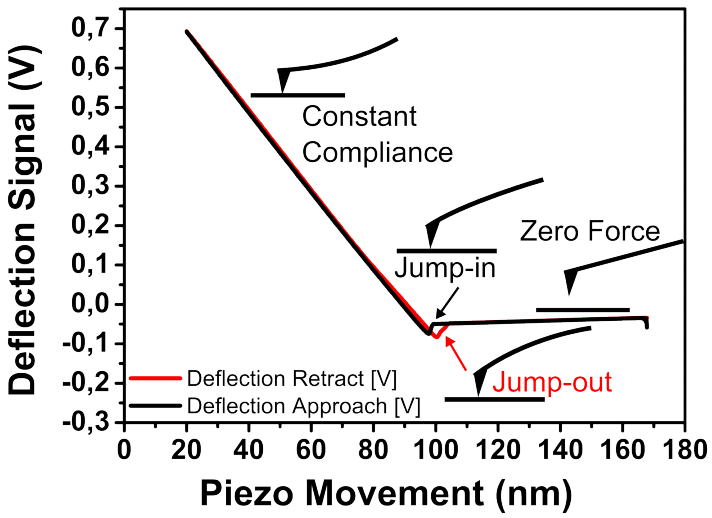

Figure 2.6: *Raw force versus piezo movement curve as the AFM tip is approached (black) and retracted (red) from a surface. The vertical axis represents the deflection signal from the PD detector.*

The horizontal axis (piezo movement) is converted to tip-sample distance by linearly fitting both zero force and constant compliance regions. The intersection of these fits is the point where the tip starts pressing against the surface and is defined as the zero tip-sample position. For hard samples that do not deform, the tip-sample distance reaches a minimum at the zero tip-sample position. In samples that deform upon mechanical contact, the tip-sample distance goes below the zero tip-sample position. For a deformable sample, the system is modeled as two springs in series, where the spring constant of the cantilever k_c and the

equivalent total spring constant k_t of the system are considered. The deformation of the sample (δ_s) is the total deformation of the two spring system (δ_t) minus the deformation of the cantilever (δ_c), which in turn can be written as a function of k_c and k_t (Eq. 2.9):

$$\begin{aligned} \delta_s &= \delta_t - \delta_c \\ \delta_s &= \delta_t \left(1 - \frac{k_t}{k_c}\right) \end{aligned} \tag{2.9}$$

In order to covert the horizontal axis into sample deformation (Eq. 2.9) and the vertical axis into force ($F = k_c\delta_t$), the cantilever's spring constant (k_c) is required. The cantilever's spring constant is obtained using a thermal noise method [46], where its thermal noise is recorded at room temperature. After applying a Fourier transform to this noise measurement, the frequency response of the cantilever is obtained. The thermal resonance of the cantilever is modeled by a Lorentz fitting function using the desired cantilever spring constant as a parameter (k_c).

To obtain mechanical information from a soft surface, a reference force curve on a hard sample must be recorded. By taking a reference measurement on a hard sample, all the deflection of the system comes solely from the cantilever deformation (δ_c). Force curves on hard reference samples give the sensitivity of the microscope, in other words, how much the cantilever is deflected per volt of signal coming from the PD detector. From this step, the PD signal from the vertical axis of a raw force curve (in volts), is converted to deflection in nanometers. The deflection is then transformed to force using the cantilever's spring constant. Raw force curves on a hard reference and soft samples are depicted in figure 2.7(a). After transforming the vertical and horizontal axis of raw force curves into force vs tip-sample distance, results such as shown in figure 2.7(b) are obtained. For a force curve taken on a hard reference sample, the curve reaches a minimum at zero tip-sample distance (dashed lines Fig. 2.7b). For soft samples, the tip-sample distance goes below zero, which represents the mechanical deformation of the sample (solid lines Fig. 2.7b).

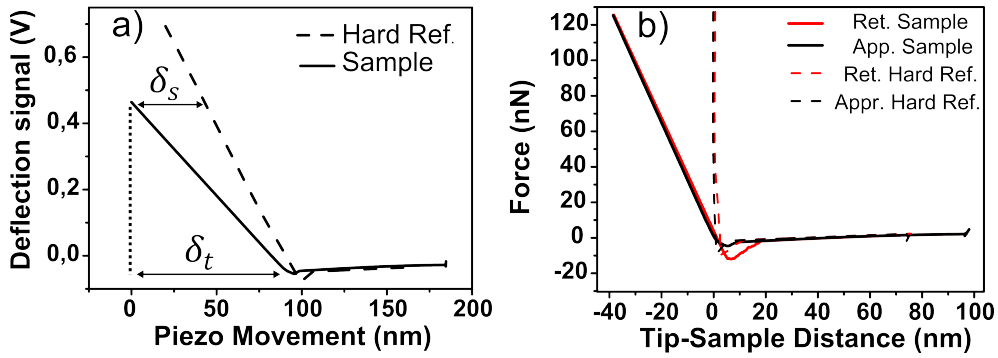

Figure 2.7: *a) Raw deflection versus piezo position curves on a hard reference sample and on a softer deformable sample. b) Final converted force curves on a deformable (solid lines) and hard samples (dashed lines) upon approach (black) and retraction (red) of the tip from the surface.*

The constant compliance part of the force curve need not be as linear as in the example shown in figure 2.7. Typically, if a flat soft surface is deformed by a sphere, the constant compliance part follows a $F \sim \delta_s^{3/2}$ dependence . Such a dependence is described by the Hertz model. [47] [48, p.231] Furthermore, force curves typically show hysteresis between approach and retraction. Hysteresis can be produced by several factors, i.e. mechanical indentation or sliding of the tip across the surface. The exact scaling between force and sample deformation will depend on the geometry of the interacting objects, their material properties and will, in general, involve more elaborate contact mechanics models than the Hertz model. Figure 2.7b) is an example where force and deformation scale linearly ($F \sim \delta_s$) and no considerable hysteresis is seen between the approach retract

of the cantilever tip. These curves were taken on structures that are artificially created in order to act as clamped beams, as discussed in following chapters 5, 6. Some clamped beam models used throughout this work shall be described in the following section (2.2.1).

2.2.1 Bending Mechanics

Within this work, two mechanically deformable geometries are studied using SPM: built-in beam (Fig. 2.8 a) and cantilever beam (Fig. 2.8b). In chapter 5 experiments on a suspended piece of nanofiber with a built-in geometry are performed. Such an experiment is analogous to a three point flexural test done on bulk materials. In chapter 6 experiments on biomineral spicules using a cantilever beam geometry are carried out. This last experiment is analogous to a two-point flexural mechanical test. In such experiments the SPM tip exerts a force (F) at distance x from the clamping position. The force produces a deformation (δ) at the position x.

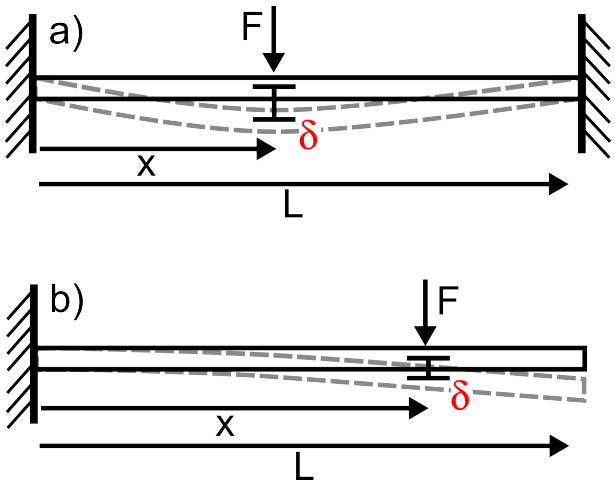

Figure 2.8: *A solid beam of length L is deformed in two different geometries. a) Built-in beam, fixed at both sides b) Cantilever beam, which is only fixed on one side while the other side moves freely.*

Such experiments are modeled using standard beam mechanics. For a built-in beam geometry, the force and deformation at the position where the load is applied are described by the *double clamped beam model* (DCBM): [49, p.339]

$$F = \frac{3L^3EI}{(L-x)^3x^3}\delta \tag{2.10}$$

where E is the Young's Modulus of the beam and I is its second moment of inertia. In a cylindrical beam the second moment of inertia is $I = \pi r^4/4$ where r

is the cylinder radius.

For the case of a cantilever beam, force and deformation at the loading position are related by: [49, p.301]

$$F = \frac{3EI}{x^3}\delta \tag{2.11}$$

In the following chapters, force measurements on micro- and nano structures are modeled using equations 2.10 and 2.11. In particular, the position dependent stiffness ($k_{sample}(x) = F/\delta$) is fitted in order to obtain mechanical information (Young's modulus) from these structures .

2.3 Local Dielectric Spectroscopy

By measuring the change in resonance frequency of a cantilever (Δf) as it interacts electrically with a sample, dynamic relaxations processes in dielectric materials can be measured. This technique is referred to as Local Dielectric Spectroscopy (Local-DS) and is analogous to broadband dielectric spectroscopy described in chapter 1 (1.1.4). Local-DS can be implemented using a conductive AFM cantilever positioned in close proximity to the sample (non-contact). DC and AC bias voltages are applied between the conductive tip and polymer sample. Polymer samples are prepared by spin coating over a conductive substrate which acts as a counter electrode as detailed in chapter 3. The applied electric field polarizes a sample volume near the tip as shown in figure 2.9.

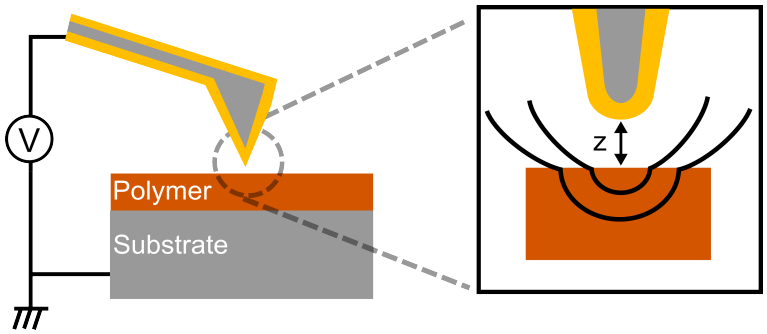

Figure 2.9: *A conductive AFM tip is positioned at a distance z from a polymer film, supported by a conductive substrate. The tip interacts with the polymer via an applied voltage V*

Local-DS is based on measuring the frequency dependence of the tip-sample capacitance. The energy of a capacitor (C) is: $U = CV^2/2$, where V is its voltage.

The applied voltage produces an attractive force between tip and sample:

$$F = -\frac{1}{2}V^2\frac{dC}{dz} \tag{2.12}$$

where z the tip-sample distance. [51] This force can be measured either directly from the cantilever deflection signal or by measuring force gradients (dF/dz). The force field due to the interaction of the charged tip with the polarized sample volume results in a small but measurable change in cantilever resonance frequency (Δf). Force gradients are related to the change in the cantilever resonance frequency as shown in equation 2.7. When an alternating voltage (V_{AC}) is applied between the tip and the counter electrode, a modulation of the Δf signal is produced by the dielectric response of the material. By combining equations 2.12 and 2.7 the following equation is obtained (Eq. 2.13):

$$\Delta f = (V - V_0)^2\frac{f_0}{4k}\frac{d^2C}{dz^2} \tag{2.13}$$

where V_0 is introduced to account for charges generated on the surface due to several processes, e.g. ion diffusion, electronic cloud rearrangements and dipolar motion within the polymer chain. If the alternating voltage is written as: $V = V_{AC}e^{i\omega t}$, then by expanding the quadratic term of 2.13 it can be shown that the term that depends only on the capacitance of the system is the second harmonic of Δf. The first harmonic is a coupled term ($V_0 \cdot V_{AC}$), containing dynamic information of the surface and probed volume. The second harmonic ($\Delta f_{2\omega}$) from equation 2.13, is experimentally measured, and relates to the capacitance by:2.14 [52, 53]

$$\Delta f_{2\omega} = V_{AC}^2\frac{f_0}{4k}\frac{d^2C}{dz^2} \tag{2.14}$$

The phase-lag (δ_ν) between the applied alternating voltage V_{AC} and the observed frequency shift $\Delta f_{2\omega}$ contains the information on the dynamics of the system. This information is obtained by filtering the Δf signal using a lock-in amplifier [44, p.628] locked on the the second harmonic (2ω). Phase lag data are presented as loss tangent functions throughout this work:

$$\begin{aligned}\tan\delta_\nu &= \frac{Im(\Delta f_{2\omega})}{Re(\Delta f_{2\omega})} \\ \tan\delta_\nu &= \frac{d^2C''/dz^2}{d^2C'/dz^2}\end{aligned} \tag{2.15}$$

where C' and C'' are the real and imaginary part of the complex capacitance.

The measured loss tangent can be analyzed using a capacitance model. According to Fumagalli *et al.* [54] the tip-sample capacitance for a dielectric film of thickness h can be approximated by:

$$C^*(z,\omega) = 2\pi\epsilon_0 R \ln\left[1 + \frac{R(1-sin\theta)}{z + h/\epsilon^*(\omega)}\right] \tag{2.16}$$

where R is the effective tip apex radius, θ its half cone angle, ϵ_0 the dielectric permittivity of vacuum and $\epsilon^*(\omega)$ the complex dielectric function of the polymer film. Given the form of the capacitance model, the loss tangent function (tan δ_ν) is not equal to that measured using a double plate capacitor. In a double plate capacitor, loss tangent is simply the ratio between complex and real part of the dielectric function (tan $\delta = \epsilon$"$/\epsilon$'). Nevertheless, loss-tangents measured with AFM (tan δ_ν) give similar peak shapes as with a double-plate capacitor. Furthermore, relaxations times are obtained by writing tan δ_ν (Eq. 2.15) in terms of the tip-sample capacitance model (Eq. 2.16) and the empirical Havriliak-Negami function described in chapter 1 (Eq. 1.27). From the obtained relaxation time (τ_{HN}), relaxation time at maximum loss, τ_{max}, is calculated analytically following equation 1.28 shown in chapter 1.

Experimental loss tangent (tan δ_ν) data obtained with local-DS are fitted combining equations 2.15, 2.16 and 1.27 taking h, R, θ,ϵ_0, ϵ_∞, and z as fixed parameters. Example data from local-DS experiments fitted with this procedure are shown in figure 2.10.

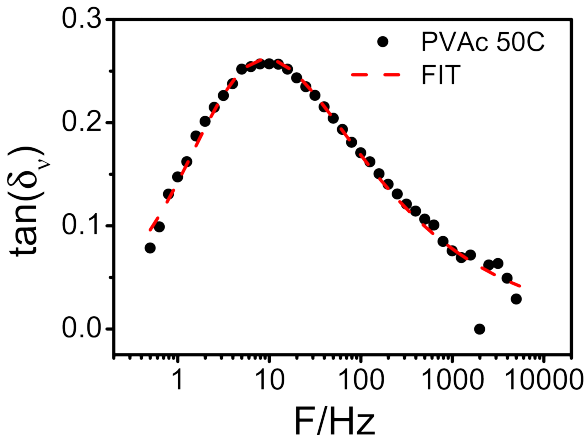

Figure 2.10: *Measurements (black circles) done with Local-DS on a 1 μm thick PVAc film coated on a gold substrate. By combining the definition of tan δ_ν (Eq. 2.15) with the tip-sample capacitance model (Eq.2.16) and a Havriliak-Negami equation (Eq.1.27), experimental data is fitted (red dashed line).*

Chapter 3

Experimental Setups and Procedures

In this chapter, the experimental setups used for studying the dynamics and mechanics of mesostructured materials with SPM are described. In the first section, experimental details about local-DS shall be given, in particular how films are prepared and which type of setup is used in these experiments. Afterward, experimental details on the mechanical studies of biominerals and sintered colloidal fibers are presented. Details on how clamped beam configurations are achieved, such as the ones shown in chapter 2, shall be presented.

3.1 Local Dielectric Spectroscopy Setup

A commercial Enviroscope AFM (Bruker, Santa Barbara, USA) is employed for local-DS. This AFM works within a hermetically sealed sample chamber that is flushed with dry nitrogen (N_2) before all experiments in order to obtain a controlled dry atmosphere. This AFM setup is equipped with a sample heating stage controlled by a commercial temperature controller (Lakeshore 331), that has an accuracy of 0.1 K and a maximum temperature of 458 K. Silicon cantilevers (Olympus OMCL-AC160TS-W2) with a 300 kHz resonance frequency, a spring constant k = 42 N/m and a tip radius R $<$ 5 nm are employed. The cantilevers used for local-DS are rendered electrically conductive by metal evaporation (5 nm chromium adhesion layer followed by 25 nm of gold). All metal coatings are produced using a modular high vacuum coating system (Bal-Tec MED020). Final tip radii are R$\sim$ 30-40 nm as determined from SEM images (LEO 1530 Gemini) (Fig. 3.1).

To minimize thermal drift due to the bimetallic effect and improve reflectivity from the backside of the cantilever, metallic coatings are deposited on both

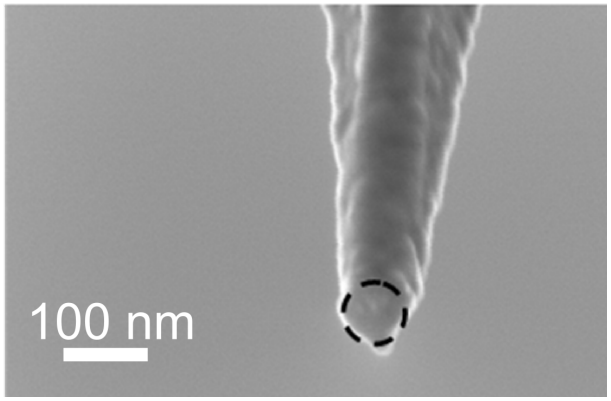

Figure 3.1: *SEM image of an AFM rendered conductive after evaporation of metallic coatings. The radius of the tip shown here is R= 38 nm.*

sides of the cantilever. Oscillation of the AFM cantilever is enforced by applying a driving voltage to a small piezo stack integrated in the commerical cantilever holder. This driving voltage is provided by a phase locked loop amplifier (PLL-Pro 2, RHK Technology, Troy, USA) connected to an AFM controller (Nanoscope IIIa, Bruker) through a signal access module (Nanoscope SAM, Bruker). Using the PLL, samples are also imaged in frequency modulation mode (FM-AFM). Additionally, the PLL electronics is used to detect changes in the resonance frequency of the cantilever (Δf) due to the dielectric response of the polymer to an alternating voltage (V_{AC}). The Δf signal from the PLL is then fed into an external lock-in amplifier (7280 DSP Signal Recovery, Ametek) to filter out its second harmonic amplitude and phase ($A_{2\omega}$, $\delta_{2\omega}$). As explained in chapter two, the second harmonic ($A_{2\omega}$ and $\delta_{2\omega}$) of the modulated signal is solely related to the capacitance of the probed volume of polymer ($C(z)$), and therefore, contains the dynamic response of the polymer chains. The alternating voltage (V_{AC}) applied between AFM tip and counter electrode is generated by the same lock-in and amplified before being applied to the cantilever. A schematic of the experimental setup is shown in figure 3.2.

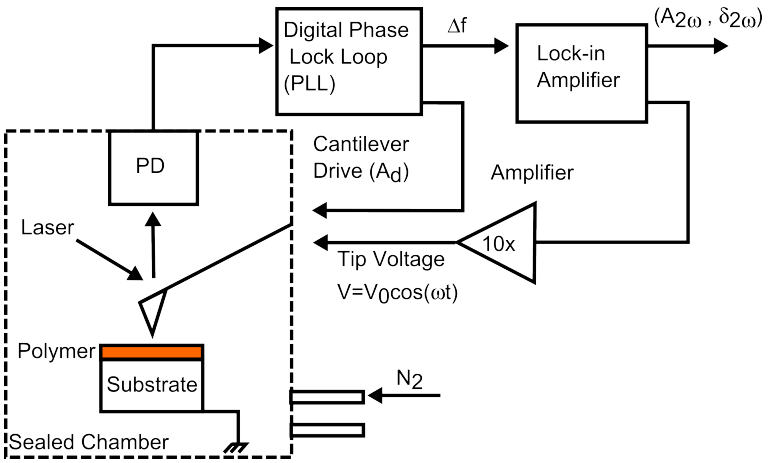

Figure 3.2: *Schematic of the experimental setup used for local-DS.*

The lock-in amplifier used here, detects modulations as low as 0.5 Hz. This sets the lower detection limit of the local-DS frequency sweep. The high frequency limit is given by the PLL electronics and the response time of the electrically interacting cantilever, which acts as a first order filter. [55] By using a stiff cantilever (300 kHz) and a broadband input filter for the PLL (100 kHz bandwidth) the reaction time of PLL is optimized to track changes in Δf with a time resolution of 100 μs. Given that the second harmonic of the Δf signal is measured in local-DS (see Eq. 2.14), the maximum frequency that can be reached with this setup is half of the inverse time resolution, i.e. 5 kHz. Therefore local-DS, as shown in this work, has a final bandwidth limited to 4 decades (0.5 Hz 5 kHz). Although Schwartz *et al.* have recently reported a broader frequency bandwidth [56], this method is based on the direct measurement of tip-sample forces instead of force gradients. It is generally accepted that force gradients ($dF/dz \sim \Delta f$) are more sensitive to tip-sample interactions than direct force measurements. [50] This is why local-DS is chosen to operate in frequency modulation (Δf) for experiments shown in this work.

3.1.1 Preparation of Polymer Films

In order to prepare thin polymer films of polyvinylacetate (PVAc) and blends of PVAc with polyethylene oxide (PEO) by spin coating (Delta 80 μ_B, Süss MicroTec). The PVAc (M_w=59400 g/mol) and PEO (M_w=32500 g/mol) used in this study are purchased, respectively, from Alfa-Aesar and Polymer Source Inc.. PVAc/PEO blends with 5 and 10 weight percent PEO (noted below as 95/5 and 90/10) are prepared from chloroform solutions, whereas toluene is used to dissolve pure PVAc samples. Films of PVAc and PVAc/PEO blends are prepared by spin coating the solution onto flat surfaces. Final film thicknesses are controlled by varying rotation speeds (ω) between 2000-4000 rpm and solution concentrations from 1 to 10 mg/ml. In figure 3.3 (a-c) the film preparation procedure is shown.

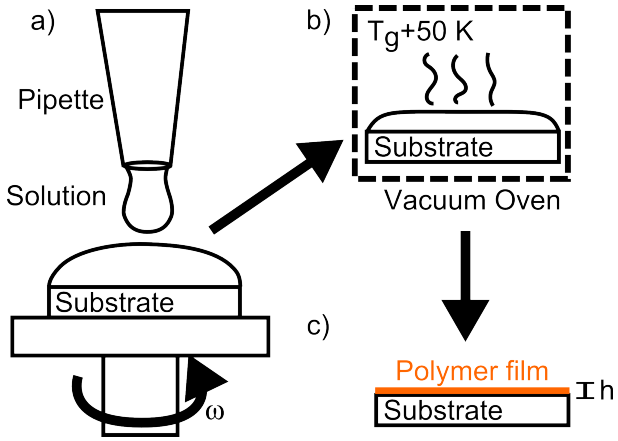

Figure 3.3: *Preparation of films. a) Films are prepared by spin coating polymer solutions using toluene or chloroform as a solvent. b) Polymer films are annealed at T_g+50 K over a period of several days in order to remove all remaining solvent. c) A smooth film with a thickness h is obtained.*

For pure PVAc and the 95/5 blend gold-coated silicon substrates prepared by physical evaporation are used. A 5 nm chromium adhesion layer is first evaporated on a silicon substrate after which, 50 nm of gold are evaporated on top. In general, gold is a suitable substrate for thick samples when that are spin coated from toluene or chloroform. For thinner films (h $<$ 200 nm), it is hard to obtain smooth films on gold, since samples tend to dewet. Therefore highly-doped commercial silicon wafers Si(100) are used for all thin film samples to obtain uniform and stable films of PVAc and PVAc/PEO blends. In both cases the conductive substrates served as counter electrodes to allow application of a defined voltage between tip and sample.

All samples are annealed in vacuum at T_g+50 K for several days (3 to 6 days) to

assure the complete removal of solvent (toluene or chloroform). Films prepared from toluene or chloroform over gold or silicon with different thicknesses (1 μm and 60 nm) do not show significant differences in loss-tangent peak position as long as the films are correctly annealed (Fig. 3.3).

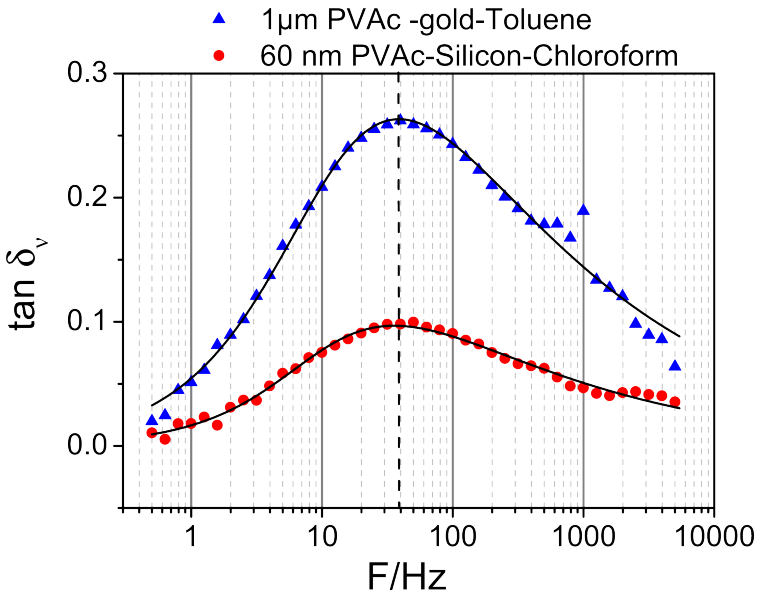

Figure 3.4: *Loss tangent curves (tan δ_ν) at 327 K for two PVAc films prepared on either silicon or gold using different solvents and with different film thicknesses. Blue triangles correspond to a 1 μm PVAc film on gold, coated from a toluene solution. Red circles correspond to a 60 nm PVAc film coated from chloroform on silicon. Solid black lines represent fitting functions.*

In particular, shifts in peak position are not expected in PVAc films that are coated on silicon or gold for h>20 nm, if they are annealed for several days at T_g+50 K. [57] As seen in figure 3.4, the height of the peak considerably decreases with film thickness. This is taken into account within the Fumagalli tip-sample capacitance model (Eq. 2.16). By combining this capacitance model with the Havriliak-Negami equation, loss tangent data are fitted for different film thicknesses (solid lines Fig. 3.4). From the fitting functions, the frequency at peak maximum is 38 Hz for the 1 μm thick film and 35 Hz for the 60 nm thick film.

Changes in loss tangent peak height with film thickness can be qualitatively explained using a partially filled capacitor model (Fig. 3.5a), where each plate has a constant surface area (A) . In this model, the air-gap (layer 1 Fig. 3.5a) represents the tip-sample distance (z) in local-DS. A dielectric film (layer 2 Fig. 3.5a) of thickness h and relative dielectric constant ϵ is used. Using double plate capacitor equations, the total force (F) on the upper plate and the contribution of the film (F_2) to this force are:

$$F = \frac{V^2}{2}\left[\frac{A\epsilon_0}{(z+h)(h/\epsilon+z)}\right] \tag{3.1}$$

$$F_2 = \frac{V^2}{2}\left[\frac{A\epsilon_0}{\epsilon(h/\epsilon+z)^2}\right] \tag{3.2}$$

The derivatives of F_2 and F with respect to z, are the proportional to change in resonance frequency in local-DS due to the film (Δf_2) and to the total air-film system (Δf). The ratio between these two signals is:

$$\frac{\Delta f_2}{\Delta f} = \frac{2(z+h)^2\epsilon}{(h+2z\epsilon+\epsilon h)(h+z\epsilon)} \tag{3.3}$$

By plotting this ratio (Eq. 3.3) as a function of film thickness (h) for a constant air-gap distance (z), it is shown that the contribution of the film (Δf_2) to the total force gradient (Δf) measured by local-DS decreases with film thickness (Fig. 3.5b).

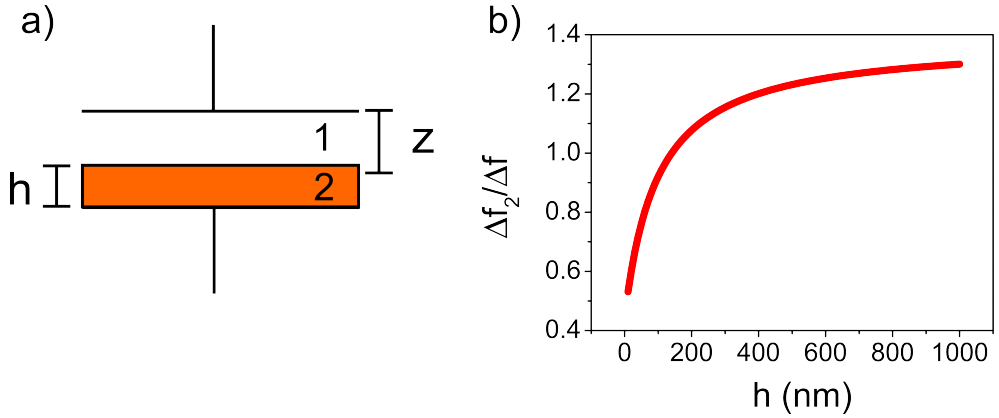

Figure 3.5: *a) Double plate capacitor model. b) Ratio $\Delta f_2/\Delta f$ as a function of the film thickness (h). Tip sample distance is kept constant (z=40 nm) and ϵ=2.24.*

This ratio explains the smaller peak heights seen in thinner films. In particular, the change in the contribution from a 1 μm to 60 nm film is 38% (Fig. 3.5). This agrees with the experimental results, where the peak height in the 60 nm film corresponds to 37% of the thicker 1 μm film (Fig. 3.4).

3.2 Bending of Biomineral Spicules

Biomineral Spicules are glued to the edge of a silicon wafer, for bending experiments, using a two component epoxy resin (UHU endfest 300). Natural and synthetic spicules are ∼100 μm in length and ∼5 μm in diameter. In order to glue them to the edge of a sample, they must be first placed individually on a hard surface. Natural spicules are suspended in water an then drop-casted onto a silicon wafer, while sythetic spicule are produced directly on a glass slide. By gently pressing them with a stiff sacrificial cantilever (k_c = 42 N/m), mounted on a three-axis oil hydraulic micromanipulator (Narishige MMO), single spicules are maneuvered and placed near the edge of a silicon wafer (cantilever 1 Fig. 3.6a). Sacrificial cantilever and spicule samples are monitored by an optical microscope as they are maneuvered by the micromanipulator. After placing the single spicule near the edge of the wafer, cantilever (1) is dipped into a two component epoxy resin glue and a drop of it is placed at the edge of the silicon wafer (Fig. 3.6b). Next, a fresh cantilever (2) is mounted to the micromanipulator. Cantilever 2 is used to move the transported spicule towards the drop of glue. After one end of the spicule is pushed into the drop of glue by cantilever 2 (Fig. 3.6c), its free end is rotated until most of it is suspended over the edge of the silicon (Fig. 3.6d). After this step cantilever 2 is dipped in epoxy glue and a second drop of epoxy is placed on top of the previous one, in order to leave the spicule well clamped to form a single sided clamped beam.

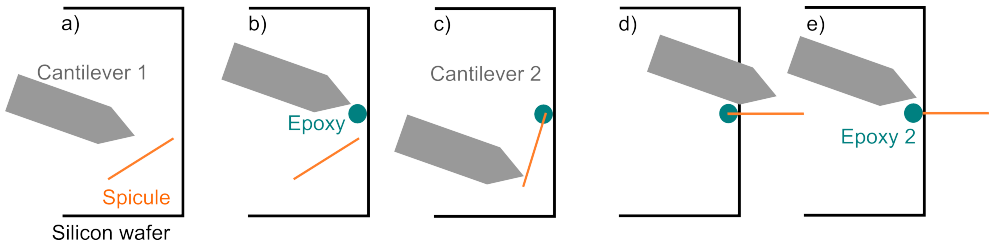

Figure 3.6: *a)-e) Procedure to produce clamped beam configuration from a single spicule. For details see text.*

The epoxy-clamped spicule is left over a period of two days in order to harden the glue, obtaining in the end a cantilever geometry (Fig. 3.7a). After preparing clamped structures from natural or sythetic spicules, they are mounted in the sample stage of a commercial AFM (Dimension 3100). Using a tipless AFM cantilever (μmasch NSC12) the flexural response of the spicule beam is measured by taking force distance curves at defined positions along its main axis (Fig. 3.7b). Nominal values of the employed tipless cantilevers are k_c=14 N/m and f_0=315 kHz. Precise values of the spring constant are obtained using the thermal noise

method [46] prior to every experiment.

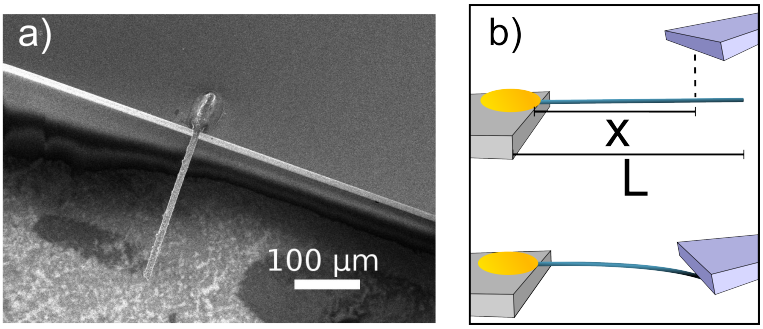

Figure 3.7: *a) SEM image of a clamped spicule. b) AFM bending experiments on clamped single spicules.*

In order to move cantilever along several positions of the spicule's main axis, the voltage applied to the AFM's x-axis scanner is changed. Doing so, steps of 2 μm are produced along the suspended piece of spicule. By comparing these force curves with ones taken on the hard silicon wafer itself, the effective spring constant k_s of the spicule is obtained (chapter 2 2.2). This effective spring constant is position dependent ($k_s \equiv k_s(x)$). For each loading position, between 30 and 40 force-distance curves are recorded. The applied load is kept constant along single spicules (150 nN - 300 nN).

Given that the spicule is usually longer than the maximum range the cantilever scan is allowed to move laterally (100 μm), the beam deflection versus position curves are taken in two steps. During the first series of steps, probing started at the free end of the spicule, proceeding towards the clamped end exploiting the full piezo scan range of the AFM. For the second step, the motorized sample stage of the AFM was employed to reposition the spicule along its axis by a defined distance to allow full coverage of the remaining part by a second piezo scan (including an overlap of at least 10 μm to facilitate overlay of the two data sets).

It is not possible to probe the full length of neither synthetic nor natural samples since, close to the clamping point, sufficient linear bending of the spicule ($\delta > 5$ nm) is harder to achieve within the linear deflection regime of the AFM cantilever. SEM images of the samples are taken after the AFM measurements in order to determine length L and radius R of the spicules, as shown in figure 3.7(a). It is assumed that spicules are well represented by a homogeneous cylinder. This assumption of course implies that the values of the Youngs modulus obtained are effective ones for the whole composite structure, which might differ from that of a single homogeneous cylinder. Effective stiffness vs loading position

are fitted using using equation 2.11, where an additional offset parameter x_0 is introduced. This additional fit parameter is necessary to adjust for uncertainties in the determination of the clamping point.

3.2.1 Protein Content of Spicules

In order to determine the protein content of single spicules, an SPM based thermogravimetric analysis (nano-TGA) procedure is developed. Such an experiment consists in detecting mass changes of a sample placed on the backside of a cantilever by measuring changes in the resonance frequency of the sample-AFM cantilever system. It is well known that changes in mass of a cantilever beam are inversely related to the square of its resonance frequency ($\Delta m \sim 1/f^2$). [58] Furthermore, microcantilever based mass detection schemes have reported sesitivities of $\sim 10^{-12}$ g/Hz. [59, 60]

In this work, nano-TGA is implemented using a commercial JPK Nanowizard AFM (JPK Instruments, Berlin). The advantage of this AFM is that it has an all glass cantilever holder that can be annealed at high temperatures. Initially, the resonance frequency (f_0) and spring constant (k_C) of the bare tipless cantilever are determined by the thermal noise method. Natural and synthetic spicules are then transferred onto this cantilever (cantilever 1) (Fig. 3.8a). Spicules are maneuvered and placed on cantilever 1 using a sacrificial cantilever tip (cantilever 2) mounted on the same micromanipulator system described in the previous section (Narishige MMO). After loading the spicule on the backside of cantilever 1, the resonance frequency of the cantilever is measured again (f_1). The spicule-loaded cantilever, including cantilever holder, are calcinated in an oven at 773K for 10 minutes to remove the organic content within the sample (Fig. 3.8b).

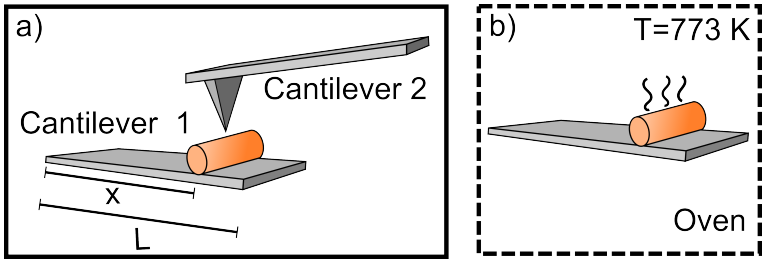

Figure 3.8: *Nano-TGA experiment. a) A single biomineral spicule is loaded on the backside of an SPM cantilever. b) The spicule loaded cantilever is then calcinated within an oven at 773 K to remove the spicules organic content.*

After cooling down to room temperature, the resonance frequency of the spicule-cantilever system is measured again (f_2). If organic content is lost during calci-

nation, f_2 should be greater than f_1. The change in mass of the system (Δm) relates to the resonance frequencies of the cantilever by:

$$\Delta m = \frac{k_c}{4\pi^2}\left[\frac{1}{f_1^2} - \frac{1}{f_2^2}\right] \tag{3.4}$$

Equation 3.4 holds when the mass loaded on the cantilever is placed at its end. In most of experiments, samples are not loaded precisely at the end of the cantilever. Therefore a correction factor must be added to equation 3.4. If the spicule is placed a distance x from the fixed side of a cantilever of length L_c, then the cantilever stiffness at x relates to the stiffness at the free end, $k_c(L_c)$, by:

$$k_c(x) = \left(\frac{L_c}{x}\right)^3 k_c(L_c) \tag{3.5}$$

In chapter 6 results using this nano-TGA procedure to obtain the protein content within single natural and synthetic spicules are presented.

3.3 Bending of Colloidal Nanofibers

3.3.1 Sample preparation

Nanofibers for bending experiments are prepared by colloid electrospinning (ES) followed by a calcination step as described previously by Friedemann *et al.*. [24] Before calcination, nanofibers are composed of 20 nm diameter silica particles embedded in a polyvinyl alcohol (PVA) polymer matrix. In addition, PS particles of defined sizes can be introduced within the nanofiber. Three types of nanofibers are prepared: without PS particles, with 60 nm PS particles and 260 nm PS particles. The mass concentration of PVA and silica particles in the electrospinning feed was kept constant (70 g/L). PS particles are added to the electrospinning dispersion with the same mass concentration (24 g/L). The size of PS particles is determined by dynamic light scattering (DLS) at a fixed angle of 90^o using a Nicomp 370 Submicron Particle Sizer (Nicomp).

The nanofibers are electrospinned directly onto a commercial HS-500 MG silicon calibration grids (Budget Sensors) with rectangular trenches that have a pitch of 5 and 10 μm and a depth of 500 nm. This fabrication procedure leads to nanofibers, with suspended segments above the trenches. A subsequent calcination step of the fiber material at 873 K yields sintered silica fibers without or with voids left by the removal of the sacrificial PS particles (Fig. 3.9a-b). The final fiber morphology was visualized by scanning electron microscopy (SEM) at low acelerations voltages of 1-2 kV (LEO 1530 Gemini, Zeiss).

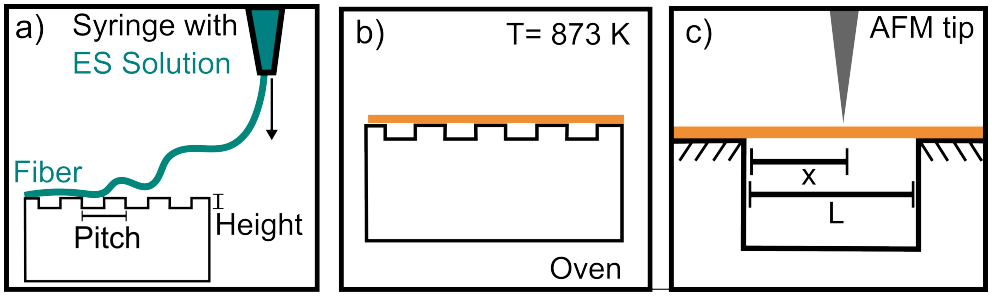

Figure 3.9: *a) Electrospinning (ES) fibers are directly deposited on an AFM calibration microgrid. b) Fibers and microgrid are consequently calcinated at 873 K in order to remove organic content and sinter silica particles. c) AFM bending experiments on the suspended pieces of sintered colloidal fibers.*

3.3.2 Mechanical Testing

AFM imaging and mechanical bending experiments are performed using a Dimension 3100 AFM (Veeco) with an XY closed loop piezo translation system. The XY closed loop system is important in order to achieve precise positioning of the tip on top of the fiber. Force curves at 20-30 equidistant positions over suspended segments of fiber are recorded. At each position, 50 force curves are obtained with a defined maximum load set by the trigger mode of the AFM. For fibers without voids, typical loads of 600 nN are applied to achieve more than 5 nm of deformation along the whole fiber using stiff OMCLAC 160 TN-W2 cantilevers (Olympus), which have a nominal spring constant of k = 42 N/m and 300 kHz resonance frequency. For fibers with 60 nm and 260 nm voids, smaller loads are required to produce more than 5 nm of fiber deformation (30 nN and 100 nN respectively). In these two cases, softer OMCLAC 240 TS cantilevers (Olympus) with a nominal spring constant of $k_c = 2$ N/m and 70 kHz resonance frequency are used. Before measurements, precise spring constants are determined using the thermal tune method. To verify that force distance curves are

taken on well-defined positions along the top of the fiber, the suspended piece of fiber is imaged by tapping mode AFM, where the cantilever is oscillated over the sample making only intermittent contact. When changing from imaging to force measurements, the oscillation of the cantilever is switched off by setting the corresponding drive amplitude (A_d) to zero. The acquired raw data, i.e. the detector voltage versus piezo position curves, are converted to force versus distance curves using a self-written LabView program. For the conversion, the spring constant of the respective cantilever and the deflection sensitivity, i.e. the conversion factor between detector voltage and cantilever deflection in nanometers, need to be previously known. Deflection sensitivity was derived from reference force curves recorded on a hard substrate, such as the surface of the silicon micro-grid onto which the fibers are electrospinned. Fracture experiments are carried out using the same arrangement, with the only difference that increasingly higher forces are applied at the center of the suspended segment of fiber until a rupture of the fiber is observed. After rupture, the nanofibers are imaged again in tapping mode to examine at which position the fracture took place.

Chapter 4

Dynamics of Polymer Blends

In this chapter, results regarding the dynamics of a PVAc/PEO polymer blend are presented and discussed. [61] This blended system is studied using the local dielectric spectroscopy (local-DS) setup described in section (3.1). In the first section of this chapter (4.1) the procedure to obtain loss-tangent curves ($\tan\delta_\nu$) using local-DS is described. The technique's resolution is also discussed within this section. In the second part of this chapter (4.2), local DS spectra for pure PVAc and two PVAc/PEO blends are shown and compared to bulk broadband dielectric spectra. In the third section (4.3), phase separated regions of a 90/10 PVAc/PEO film are studied by correlating AFM imaging with local spectra taken at different positions relative to phase separated structures. In the last section of this chapter (4.4) the growth of phase separated regions is analyzed by combining AFM imaging with local-DS.

4.1 Raw measurements and resolution

Local-DS experimental spectra are obtained by first taking a reference measurement over a bare substrate and then over the polymer film. The reference spectrum is then subtracted from the one taken over the polymer at every temperature. To obtain a reference spectrum, a scratch is made with a sharp syringe needle to locally remove the polymer film and uncover the bare substrate (inset Fig.4.1a). Raw phase lag spectra of the $\Delta f_{2\omega}$ component for the film ($\delta_{2\omega film}$) and bare substrate ($\delta_{2\omega bare}$) are shown in figure 4.1(a). Each of these raw curves corresponds to an average of 6 frequency sweeps from 0.5 Hz to 5 kHz, taking 8 minutes to complete one. By modeling the mechanical motion of the cantilever as the tip interacts electrically with the surface, it can be shown that the frequency response of the force, and force gradient, resembles that of a first order filter. [55] This explains the strong roll-off in frequency seen in raw curves at around 200 Hz. The difference between the bare substrate and film $\delta_\nu = \delta_{bare} - \delta_{film}$ (Fig.4.1b) gives a peak which is associated with the relaxation of the polymer film.

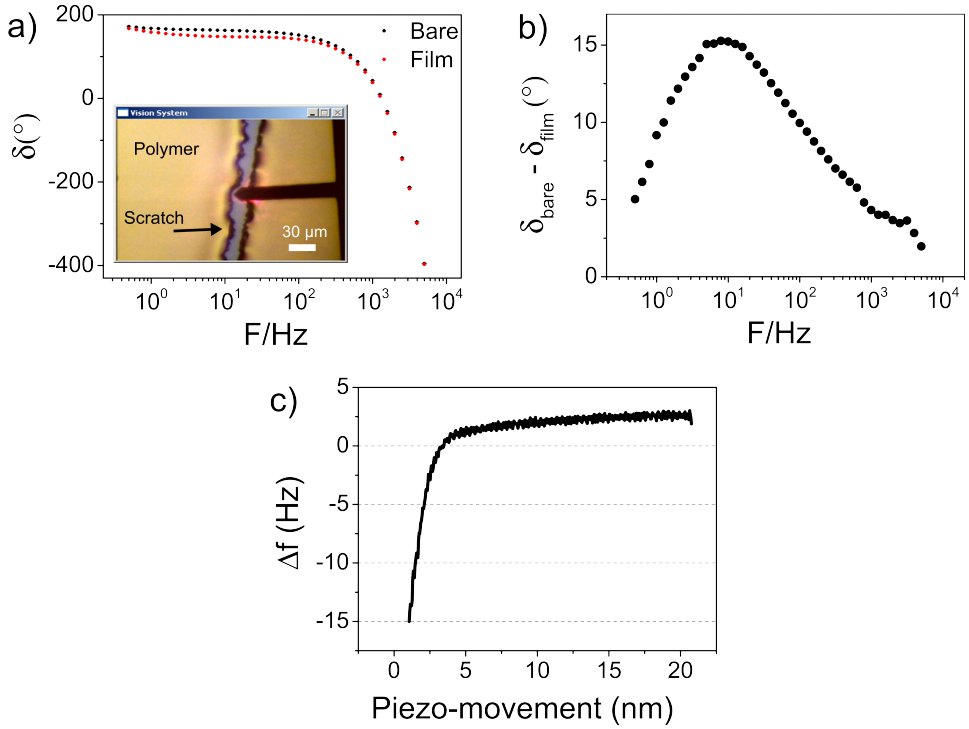

Figure 4.1: *a) Phase lag signal versus frequency plots for the bare substrate and polymer film at $T = 323$ K. Inset: Top-view from AFM optical microscope. b) Difference between phase lag signals from bare substrate and film ($\delta_{bare} - \delta_{film}$). c) Δf vs piezo displacement curve to position tip.*

In order to position the tip at a fixed height (z) above the sample surface it is first approached to the surface in imaging mode (FM-AFM) using the Δf signal as the setpoint feedback for the z-piezo, without applying an electrical bias to the tip. Typical approach set-points are Δf ∼-5 Hz. This set-points ensures a soft intermittent contact of the tip with the sample. After imaging the region in FM-AFM mode, the instrument is switched to spectroscopy mode, where Δf is recorded as a function of the vertical piezo-position while the tip is ramped towards and back from the surface. In order to position the tip at a defined distance from the surface, Δf versus piezo movement curves are recorded with a defined ramp size (r) of the vertical movement. Using the trigger function of the force spectroscopy mode, the ramp is reversed from $\Delta f \sim$ -5 Hz, similar to the set-point used for imaging. This leaves the the tip at a retracted position being the tip-sample distance $z = r + A$, where A is the amplitude of oscillation of the cantilever. Typical oscillation amplitudes used in local-DS are A = 20 nm. Tip-sample distances of z = 40 - 50 nm are typically used (Fig. 4.1c). To position the tip above the bare substrate for a reference spectrum, the film thickness h

is added to the total height ($z_{bare} = z + h$), in order to record all spectra at the same distance from the substrate (i.e. supporting counter electrode). Once the tip was positioned at the correct height, all AFM feedbacks are turned off and an alternating voltage (V_{AC}) is applied and sweeped in frequency. Alternating voltages with amplitudes between 2 and 4 Volts were used. After each frequency sweep, the tip-sample distance is readjusted by another piezo-movement ramp to compensate for possible drifts.

The resolution of this technique is estimated using a finite element model (FEM) simulation implemented on COMSOL multiphysics. In figure 4.2 (a) the geometry of the model is shown using a 50 nm film. The AFM tip is modeled as a sphere of radius R = 40 nm attached to a cone with a 30 degree opening angle (white area). In this model the tip is placed 40 nm above the surface of a 50 nm thick film. A bias voltage of 4 V is applied to the tip relative to the grounded substrate. The polymer film starts at the horizontal dash-dot line and extends 50 nm below, being grounded at its bottom side (V = 0). A static dielectric constant of $\epsilon^{'}$=2.24 is assumed, corresponding to that of PVAc. Calculated equipotential lines shown in figure 4.2(a) go between 0.5 to 0.1 V in steps of 0.1 V. Using this model, the voltage drop along the surface of the polymer (dash-dot line Fig. 4.2a) and inside the film (dashed line 4.2a) are plotted for different film thicknesses (Fig. 4.2 b and c). Since Local-DS is a force gradient measurement, i.e. it senses changes in potential, the probed volume is estimated by the voltage drop along the surface and within the film. For a 50 nm film the voltage drops to two-thirds of its maximum value within a lateral distance of ∼150 nm from the tip's axis along the surface of the film. This is defined as the lateral resolution of the probe for a 50 nm film. For the penetration depth, the voltage drops two thirds of its maximum along the vertical axis at ∼30 nm beneath the film's surface. This means that for a 50 nm thick film most of the local-DS signal comes from a volume that spans laterally ∼150 nm around the tip's center and penetrates 30 nm into the film. Probing volumes grow with the film thicknesses as shown by the other curves in figure 4.2(b-c). It is found that probing volumes do not change much when the tip radius varies between 30 and 40 nm.

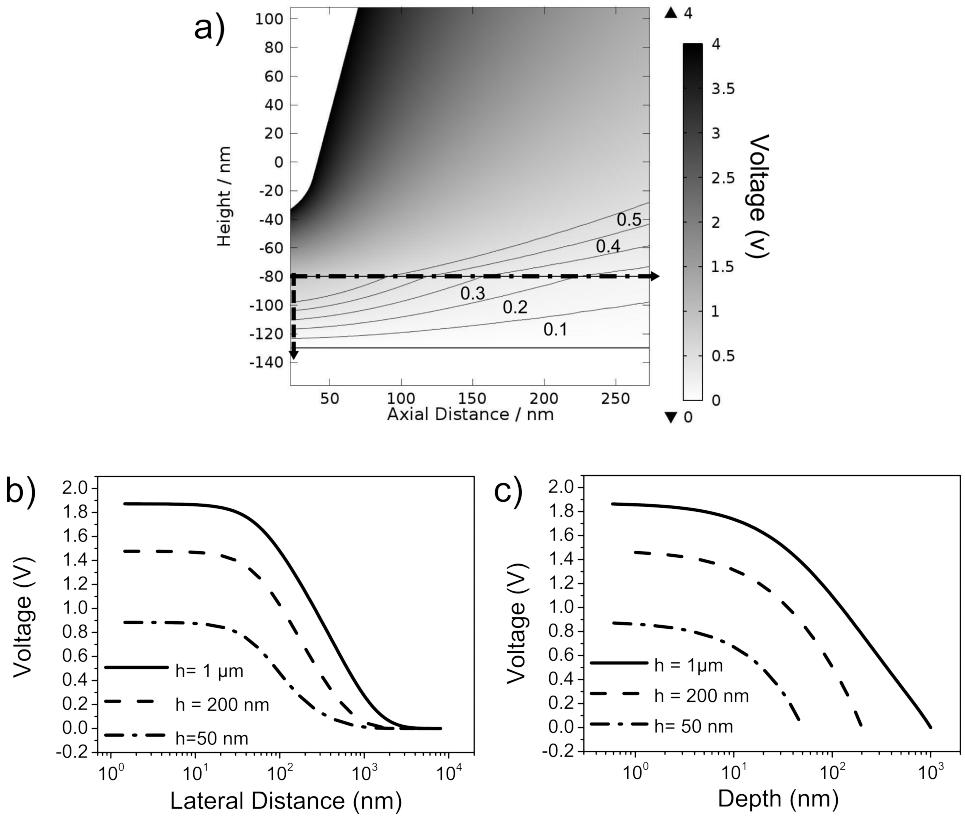

Figure 4.2: *a) Finite element simulation using COMSOL Multiphysics. b) Voltage along the surface of the polymer measured as distance from the tip's axis for several film thicknesses. c) Voltage along the tips axis within the film for several film thicknesses.*

4.2 Dynamic heterogeneity in PVAc/PEO

Loss tangent curves for a pure 1 μm thick PVAc film and 200 nm thick PVAc/PEO blends (95/5 and 90/10) are shown for several temperatures (Fig. 4.3) with their respective fits. All curves are fitted with HN-function combined with Fumagalli's capacitance model as described in chapter 2 (2.3). The blending of PEO into PVAc leads to a shift of the loss tanget peak to higher frequencies for a given temperature. This speed-up of the dynamics with increasing PEO content under isothermal conditions, e.g. T = 323 K (red data Fig. 4.3), is a direct consequence of dynamic heretogeneity, as discussed in chapter 1 (1.1.5). The relaxation processes reflecting PVAc and PEO segmental dynamics in the blend are shifted relative to those of the homopolymers. [18] Because of temperature limitations of our local-DS setup, only PVAc segmental dynamics in PVAc-rich blends is accessible.

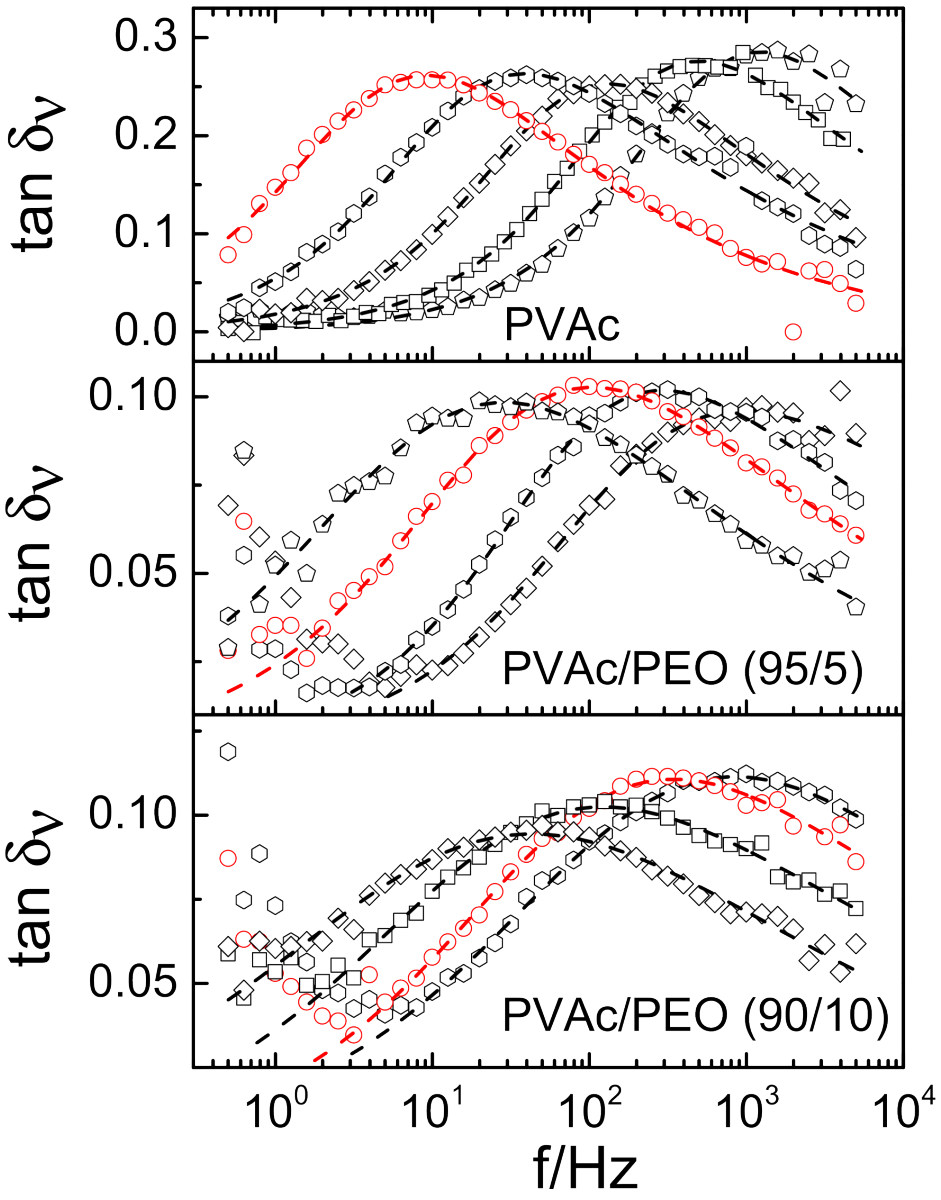

Figure 4.3: *Loss tangent spectra for a pure PVAc film and two films of PVAc/PEO blends with different mixing ratios. a) Pure PVAC at 323, 327, 331, 335 and 339 K b) PVAc/PEO 95/5 at 319, 323, 327, 329 K. c) PVAc/PEO 90/10 at 315, 319, 323 and 325 K*

The shape of loss-tangent curves, shown in figure 4.4, exhibits a systematic broadening with increasing PEO concentration. The curves (Fig. 4.4) are shifted in the vertical direction in order to make their maximums match. The broadening is evident both for the low and high frequency sides of the peak. This is a manifestation of increasing concentration fluctuations in the blend [20]. Concentration fluctuations are spatial heterogeneities of the blend's composition. Such fluctuations in local composition are thought to occur on length scales of around 10 nm near T_g and contribute with different relaxations times to the α-process. This leads to the broadening of the peak, which is the second key signature of dynamic heterogeneity.

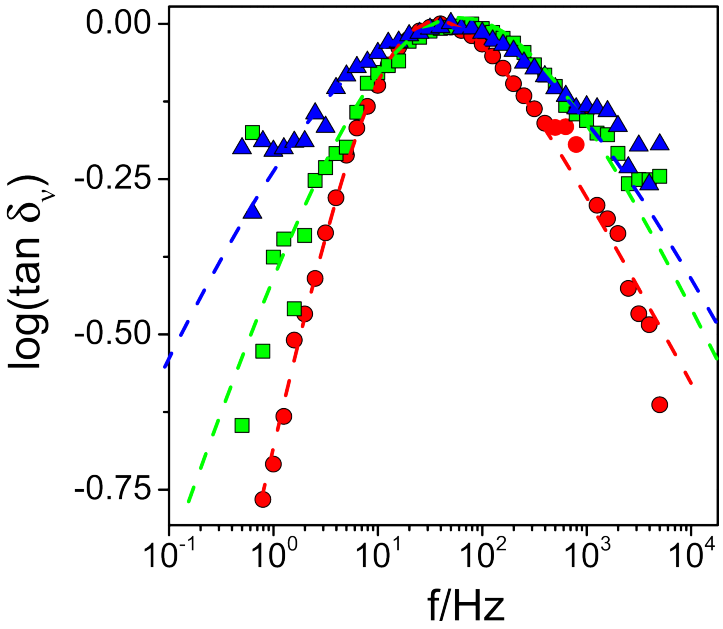

Figure 4.4: *a) Broadening of α-relaxation process with increasing PEO content for pure PVAc at 327 K (red circles), PVAc/PEO 95/5 at 321 K (green squares) and 90/10 at 315 K (blue triangles).*

Using the procedure outlined in the chapter 2 (2.3), the PVAc segmental relaxation times (τ) at peak maximum loss are extracted and plotted in figure (4.5) in the Arrhenius representation. The temperature dependence of the relaxation time $\tau(T)$ conforms to the Vogel-Fulcher-Tammann (VFT) equation as $\tau = (\tau_0 \exp B/(T - T_0))$, where τ_0 is the relaxation time in the limit of high temperatures, B is the activation parameter and T_0 the ideal glass transition temperature. The PVAc relaxation times in the PVAc/PEO blends are systematically shifted towards lower temperatures with increasing PEO content. This conforms to earlier measurements on bulk samples obtained by BDS. [18]

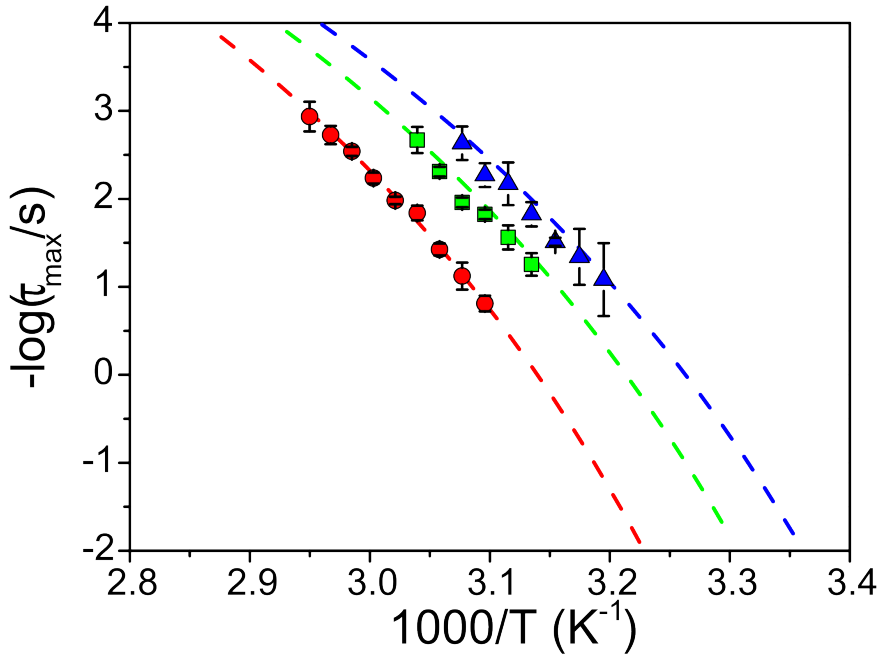

Figure 4.5: *Arrhenius representation with relaxation times for pure PVAc (red circles), PVAc/PEO 95/5 (green squares) and 90/10 (blue triangles). Dash lines represent VFT fits for the corresponding data.*

Relaxation times of Local-DS experiments are compared to broadband dielectric spectroscopy (BDS) results on bulk polymer samples (Fig. 4.6). [18] Relaxations times from local-DS show a slight enhancement of dynamics in blended films compared to their bulk counterpart (dashed green and blue lines), while pure PVAc relaxation times follow closely its bulk values (red dash line).

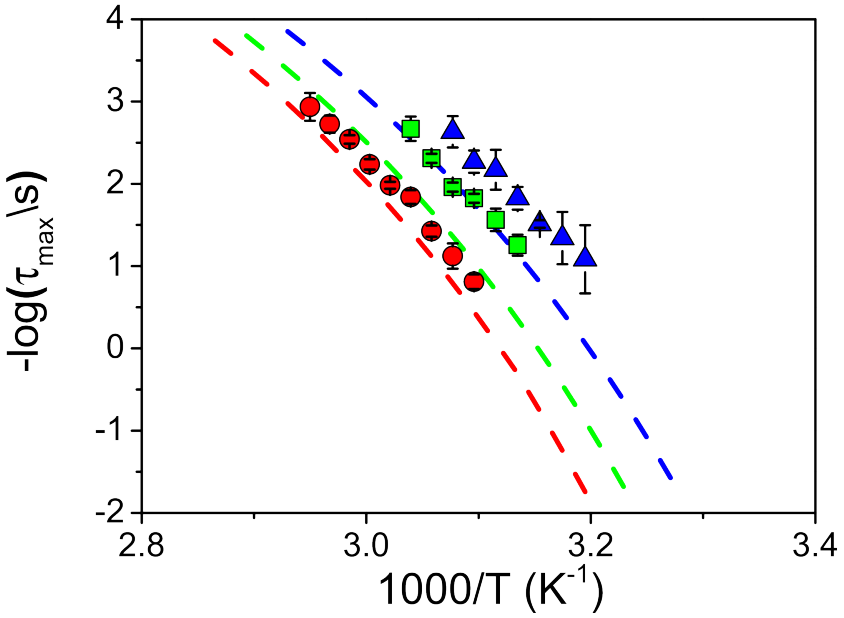

Figure 4.6: *Comparison between relaxation times obtained using local-DS (solid points) and bulk data obtained with BDS (dashed lines). Red, green and blue points represent pure PVAc and PVAc/PEO blends, 95/5 and 90/10, respectively. The same color code applies to the bulk BDS measurements (dashed lines).*

The enhancement of dynamics seen by local-DS in blends is believed to be due to the limited resolution of the technique (Chapter 3.1) and the model used to fit the peaks instead of a physical effect, i.e. a thin surface layer with faster dynamics. This last scenario is discarded, given that changes in dynamics are not expected for thick PVAc films h$\geq$ 35 nm. [62] Furthermore, no changes in local-DS peak position are observed in a 50 nm thin PVAc/PEO 90/10 film compared to the 200 nm film (see section 4.3), which suggests all measurements shown here should indeed exhibit bulk-like dynamics. The second option to explain mismatch between BDS and local-DS results for blends is the model used to fit loss tangent peaks. The model used here does not consider mobile charge carriers, which would describe the low frequency tail of dielectric spectra. Mobile charge carriers, i.e. ions, are incorporated into the complex dielectric function (1.27) as an imaginary term (ϵ_2=-i$\sigma_0/\epsilon_0\omega$), where σ_0 is called the d.c.-conductivity. [12, p.81] The complex

dielectric function with the mobile charge carrier term, should be used in Fumagalli's tip-sample capacitance model (2.16) to fit the complete curve, including low frequency tail. This could in principle contribute to changes in the τ_{max} value, given the non-linearity of the tip-sample capacitance model. Although Arrhenius plots for blends measured with local-DS do not match exactly with bulk BDS results, loss tangent peak position can still be used as a compositional probe for thick films, given that the peak position is sensitive to PEO concentration and it does not change, under isothermal conditions, for films with h = 200 nm or 50 nm.

Shape factors (m,n) for local-DS measurements are also compared to bulk measurements (Fig.4.7a-c). Pure PVAc and PVAc/PEO 95/5 shape factors follow closely to the bulk measurements (dashed lines). Shape factors for the 90/10 blend show more scatter, due to the broadness of the peak, which is comparable to the size of the available frequency range of local-DS (4 decades in frequency). The broadness of the 90/10 loss tangent peak produces an even greater uncertainty in the determination of symmetric (m) and asymmetric (m·n) broadening of the peak.

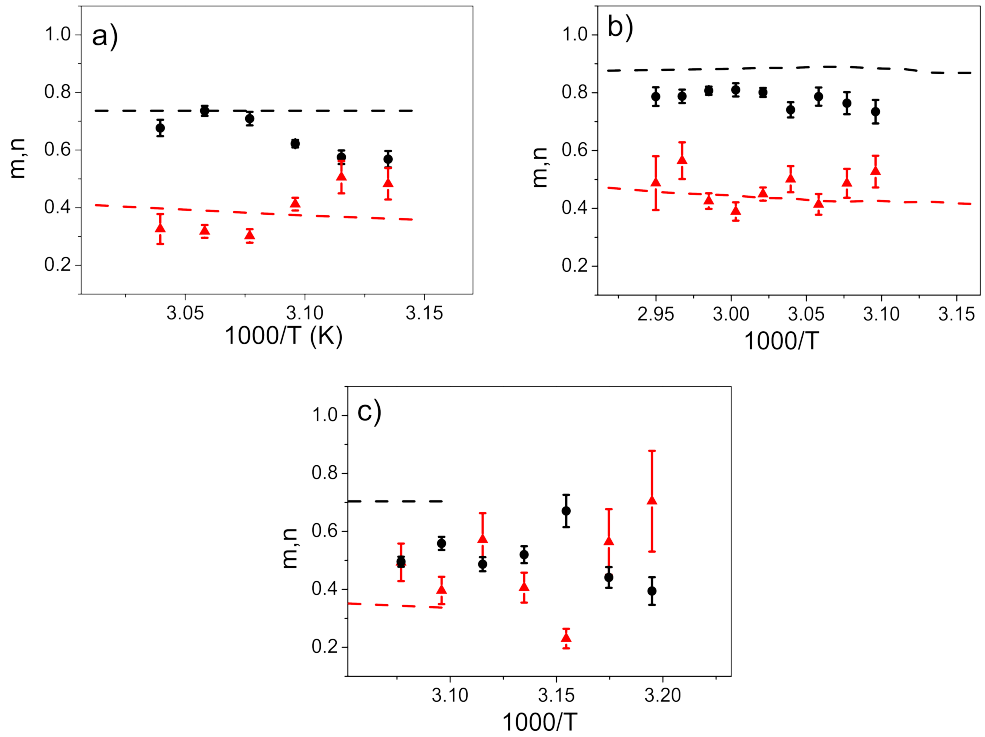

Figure 4.7: *Local-DS shape parameters m (black circles) and n (red triangles) compared to bulk BDS measurements (dashed lines) for: a) pure PVAc b) PVAc/PEO 95/5 and c) PVAc/PEO 90/10 blends*

Although segmental relaxation times in immiscible polymer blends were studied earlier by local-DS, [63] it is the first time that the same method is employed to detect segmental dynamics and dynamic heterogeneities in miscible polymer blends. According to the self-concentration model of Lodge and McLeish (LM), [17] chain connectivity enhances the local composition of the chains and the segmental dynamics of a given component in a miscible blend are biased towards the corresponding homopolymer. This theory predicts the shift of the relaxations times towards higher frequencies. The relevant length scale for evaluating the self-concentration (ϕ_S) is the Kuhn length of PVAc (l_K=1.36 nm) as explained in chapter 1 (1.1.5).

4.3 Crystallization and phase separation

In the thinner (h=50 nm) PVAc/PEO 90/10 films, indications of phase separation driven by the local crystallization of PEO are found. Crystallization and phase separation in this case are induced by the syringe scratch made on the film in order to obtain the bare substrate reference spectra. Imaging of the polymer film adjacent to the scratched area in amplitude modulation AFM (AM-AFM) reveals seaweed and dendrite-like fingers that are 4 nm in height (Fig. 4.8 a). Given that no significant contrast in the AM-AFM phase signal image on dendrite regions is seen, the measured topographical height (4 nm) is believed be close to the actual height of the dendrite structures. Such fingers are stable within temperatures ranging from ambient to 323 K (Fig. 4.8b). On heating to even higher temperatures, the already formed fingers start disappearing at 328 K (Fig. 4.8c), which agrees with the melting temperatures of PEO dendrites (337 K). [69] This transition temperature together with the seaweed and dendritic-like appearance is a strong indication that the dentrites are in fact PEO crystals growing on top of the PVAc/PEO blend. After the dendrites of this sample where partially melted at 328 K, the same sample is stored at room temperature for 2 months. The dendrites are seen to reappear after this period of time (Fig. 4.8d).

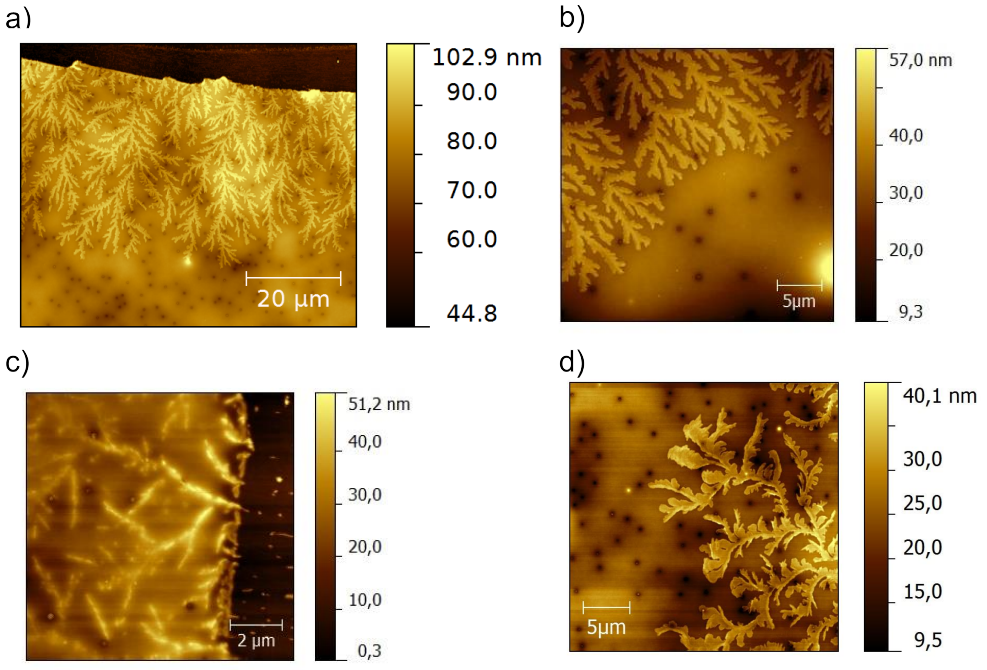

Figure 4.8: *a) AM-AFM image along the scratch at room temperature. b) Dendrites at 323 K and at c) 328 K. d) Subsequently stored at room temperature for 2 months*

The reappearance of dendrites on the film surface could mean either that the PEO chains diffuse from the blend back to the surface at room temperature; or that the PEO chains after partial melting stay on the surface of the film and slowly recrystallize at room temperature. In any case, it is shown that the syringe scratch of the sample provides a defect that induces the (heterogeneous) nucleation of PEO crystals. The PEO crystallization in miscible polymer blends has been studied earlier. In particular the PEO crystallization has been studied in blends with PMMA, where dendritic growth of PEO crystals was observed as well. [68, 70, 71, 72]

The composition around PEO dendrites is studied combining local-DS and FM-AFM imaging. First a region with dendrites is imaged using FM-AFM at 323 K. After this, the AFM tip is placed on three different positions relative to PEO dendrite, recording local-DS loss tangent curves: on top (red triangle), 1 μm away (green circles) and 5 μm away from the dendrite (blue squares) as shown in figure 4.9(a). Loss tangent curves are shown for the corresponding positions in figure 4.9(b). For comparison, local-DS spectra obtained at the same temperature but from thicker homogeneous films are shown for pure PVAc and PVAc/PEO 90/10 (dashed lines Fig. 4.9b).

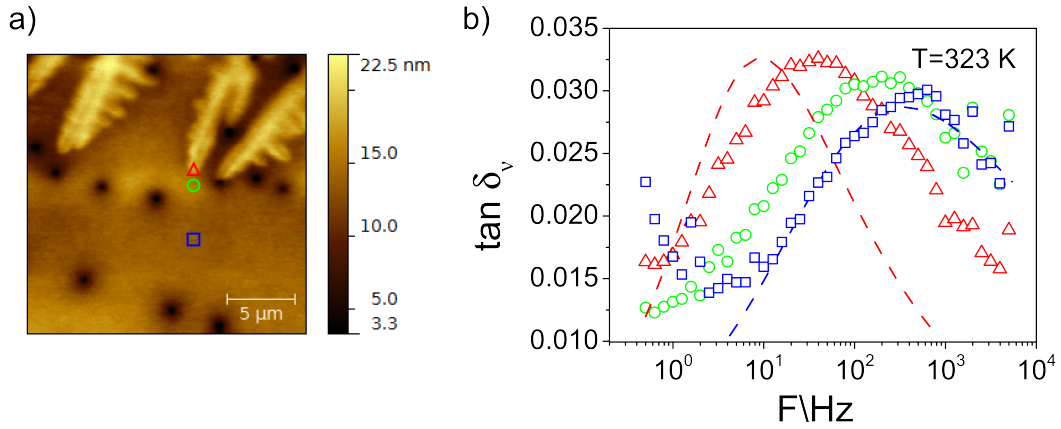

Figure 4.9: *a) FM-AFM image of PEO dendrites at 323 K and the local-DS probing positions: On top of dendrite (red triangle), 1 μm below (green circle) and 5 μm below it (blue square). b) Corresponding local-DS spectra at 323 K for the different probing positions. Dashed-lines indicate local-DS measurements on pure PVAc (red dashed line) and PVAc/PEO 90/10 (blue dashed-line) at 323 K for thicker films (h>200 nm).*

The loss tangent curve on top of the PEO dendrite has a maximum at ∼30 Hz, which is a frequency clearly below that expected for a 90/10 blend composition (200 Hz). This suggests that PEO crystallization drives the phase separation in

the vicinity of the dendritic-like fingers. Since the dielectric strength of the segmental process of PEO is negligible as compared to that of PVAc, the film under the PEO dendrite is probed at this position. As inferred from the spectrum on top of the dendrite, the underlying film region is enriched in PVAc. As the tip is positioned further away from the tip of the PEO dendrite (1 μm and 5 μm below) the loss tangent maximum significantly shifts towards higher frequencies regaining the original 90/10 composition 5 μm away from it.

In order to estimate the blend composition from position dependent spectra, first relaxation times (τ_{max}) must be estimated by using the fitting procedure described in previous chapters. These relaxation times are then plotted on an Arrhenius map together with the VFT fits for local-DS measurements on thicker samples (Fig. 4.10).

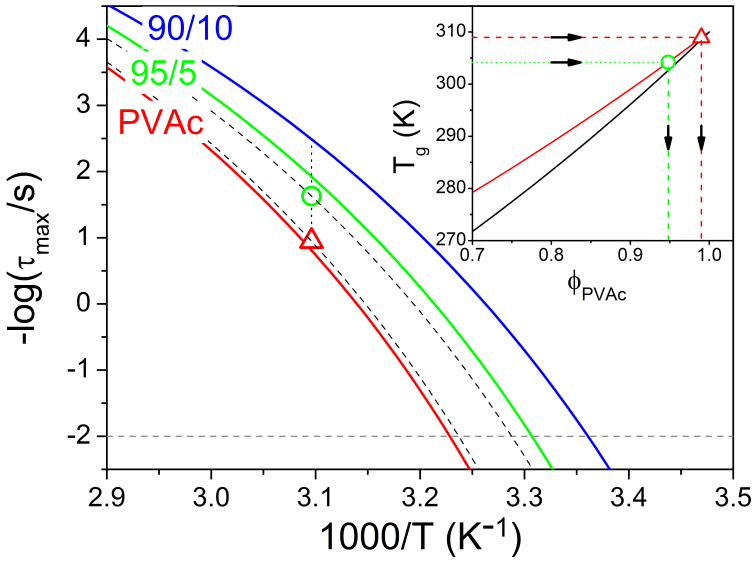

Figure 4.10: *Arrhenius plot with VFT fits for local-DS measurements on thick PVAc, 95/5 and 90/10 PVAc/PEO films represented by solid red, green and blue lines respectively. Relaxation times on top of the dendrite (red triangle) and 1 μm below (green circle) are plotted in this map. inset: Glass transition extrapolated from the Arrhenius map intersects the Lodge-Mcleish model (red curve) at the corresponding concentration (ϕ_{PVAc}). Foxx equation is represented by the solid black line.*

For the peak recorded on top of the PEO dendrite (red triangle 4.10), VFT fit parameters (B and τ_0) used for thick pure PVAc are maintained, while T_0 is varied. Doing so, a new VFT curve is generated (dashed black line), which matches the relaxation time measured on top of the PEO dendrite (red triangle). From

this new VFT curve, the glass transition temperature (defined at τ_{max} =100 s) is extrapolated. The obtained glass transition temperature is then compared to the composition dependent glass transition temperatures (T_g (ϕ_{PVAc})) shown in the inset of figure(4.10). The inset contains the Fox equation (black line) as well as the prediction from the Lodge-McLeish self-concentration model (red line) for different PVAc blend concentrations (ϕ_{PVAc}). [73, 18] The intersection of the estimated glass transition temperature with the Lodge-Mcleish model (horizontal dashed red line) gives the composition measured by local-DS. For the measurement on top of the PEO dendrite a composition of about 99/1 is estimated by the procedure. Spectra taken on top of other PEO dendrites using different cantilevers, suggest a blend composition in the range from 100/0 to 99/1. The second AFM-tip position, indicated with the blue square in figure 4.9, is located some 5 μm away from the finger. The measured loss tangent at this position is nearly identical to that of the thick 90/10 PVAc/PEO film at the same temperature. On the other hand, placing the tip 1 μm away from the tip of the PEO dendrite (green circle Fig.4.9) gives a loss tangent with a peak at intermediate frequencies for which an effective PVAc/PEO composition of 95/5 is estimated using the Lodge-McLeish model.

The gradual shift in peak position of the loss tangent (tan δ_ν) with the relative AFM-tip distance to the dendrite suggests the presence of a composition gradient with a PEO depletion zone around the finger structure. The PEO depletion zone extends to about 2 μm away from the finger-like structures. It is only beyond such distances that the nominal composition is recovered. Similar results were obtained when this experiment was repeated on top of finger-like structures obtained from other 90/10 blends of comparable thickness using different cantilevers.

It is worth pointing out that such PEO dendrite structures grow with time at around 0.5 μm/h, as shall discussed below. Given that a single LDS frequency sweep takes 8 minutes, the finger front advances $\sim$60 nm during one single sweep. For each curve shown in figure 4.9 (b) 3 frequency sweeps are averaged, during which a maximum growth distance of $\sim$ 0.2 μm is expected. This growth distance is much smaller than the distances at which the neighboring areas of the PEO dendrite front are probed (1 - 5 μm). In effect, after taking spectra at 1 μm and 5 μm below the finger front, no significant finger growth is seen. Only several hours after the last frequency sweep, growth of the dendrite is clearly visible.

4.4 Kinetics of phase separation

Given the sensitivity of local-DS to blend compositions, it is used to probe the composition around dendritic PEO crystals as they grow at a certain temperature (323 K). For this purpose the surface near a PEO dendrite is imaged in FM-AFM mode. After each FM-AFM image consecutive Local-DS spectra are recorded at a fixed position under isothermal conditions (323 K). A small depression in the film is used as a reference landmark. Figure 4.11(a) depicts the depression position (white arrow), the chosen measurement point (white circle) and the growing PEO dendrite front (Fig. 4.11a i-iv). The measurement position is located 2 μm left to the reference depression and is initially 5 μm from the dendrite tip at time t=0 h. All temporal spectra were taken at this same measurement point. The recorded loss tangent spectra at different times are plotted in figure 4.11(b).

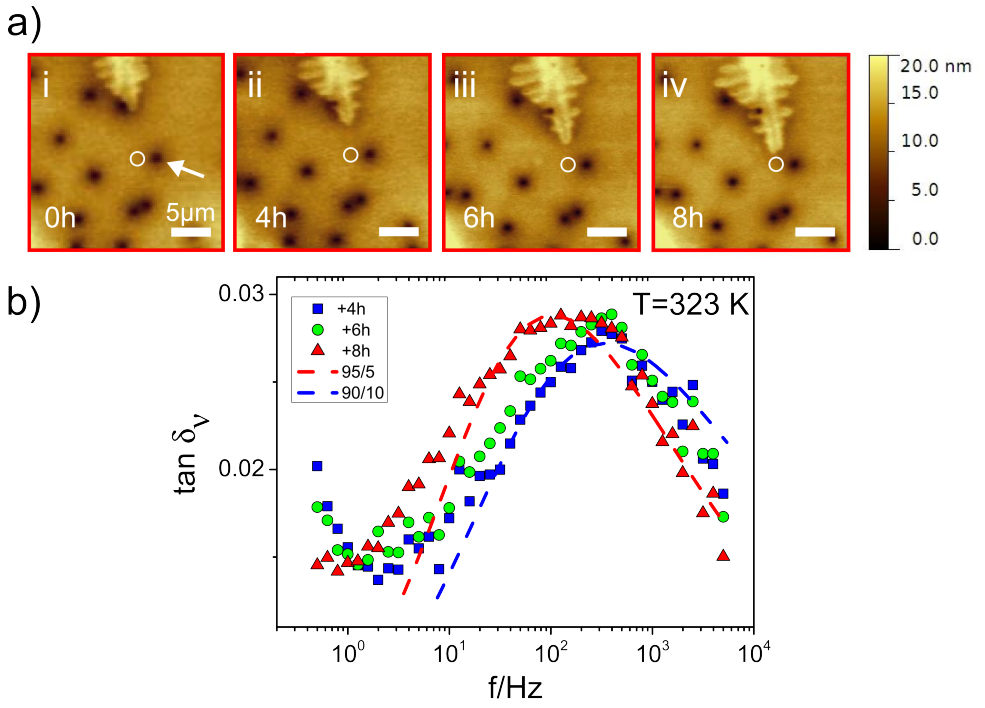

Figure 4.11: *a) FM-AFM images of a PEO dendrite at 323K which grows during several hours. The white circle marks the position at where consecutive local-DS measurements are performed. b) Local-DS measurements on the white circle position at 4h, 6h and 8h. Dash lines indicate peak positions of local-DS measurements made on pure PVAc (red) and 90/10 PVAc/PEO (blue).*

Evidently, the local blend composition changes as the finger approaches the measurement point. Each curve show in figure 4.11(b) corresponds to a time frame of

37 minutes, in which 4 spectra are averaged before the AFM image is taken. After 4 hours, when the finger tip is some 3 μm away from the reference point, loss tangent peak (∼300 Hz) and shape are reminiscent to that of 90/10 PVAc/PEO blend, i.e. the local composition is still identical to the nominal blend composition. As the finger stretches out further towards the reference point the loss tangent peak shifts to lower frequencies. When the front is around 1 μm the peak has shifted to around 100 Hz and both the peak position and peak shape roughly matches to that of 95/5 PVAc/PEO blend. These results suggest crystal dendrites of PEO are created by phase separation from the PVAc/PEO that forms the underlying film. The crystals grow slowly and give rise to regions surrounding the dendrites where the local blend composition changes in the course of time from the nominal 90/10 blend composition to environments locally enriched in PVAc.

The complete sequence of FM-AFM images recorded at 0, 3, 4, 5, 6, 7, 8 hours for the experiment described previously (Fig. 4.12) can be used to estimate the diffusion coefficient (D) of the PEO chains within the underlying film. To do so, first the distance (d) from the tip of PEO dendrite to an imaginary horizontal line (dashed line Fig. 4.12a), that crosses the landmark film depression, is measured. This distance (d) is found to decrease linearly in time with a speed of 0.5 μm/h (Fig. 4.12b). Given that the depression does not move during the experiment, it can be affirmed that the finger grows at G = 0.5 μm/h.

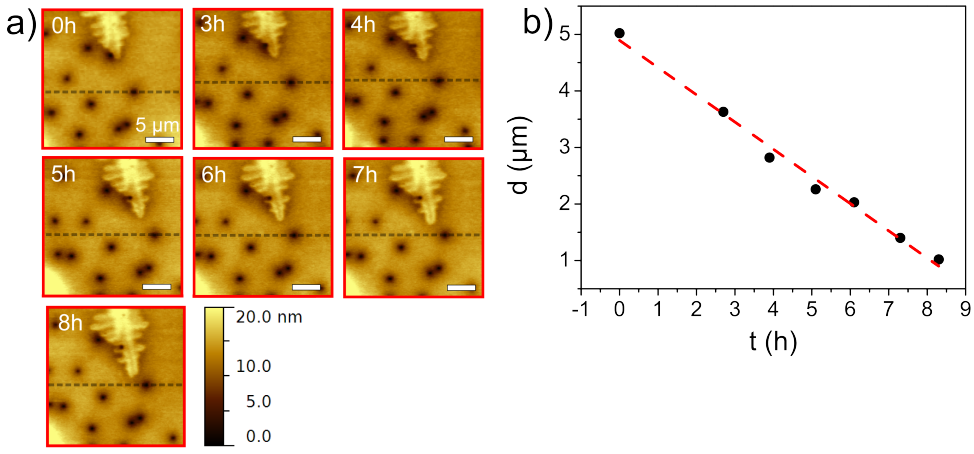

Figure 4.12: *a) Complete sequence of FM-AFM images of the growing PEO front. b) Distance from tip of growth front to dashed line against time.*

The length of the side-branch spacing of a dendrite relates to the diffusion coefficient (D) and growth rate (G) by: [74]

$$\lambda = 2.5\sqrt{d_0 \frac{D}{G}} \tag{4.1}$$

where d_0 is the capillary length. The side-branch spacing can be approximated by the dendrite tip radius ($\lambda \sim$ R). [72] The tip radius is measured from the FM-AFM image after 3 hours and is R = 250 nm. By using $d_0 = 10^{-10}$ m and a growth rate G=0.5 μm/h, a diffusion coefficient $D = 1.4 \cdot 10^{-14}$ m^2/s is obtained for the PEO chains in the blend at 323 K. This compares reasonably well to the reported diffusion coefficients found for PEO diffusion in PEO/PMMA blends above the glass transition temperature. [75]

Chapter 5

Colloidal Nanofibers

In this chapter results regarding the mechanical testing of silica nanofibers are presented. The aim of this work is to measure the forces and stresses involved in the production of nanoparticles from electrospinned nanobers reported by Friedemann *et al.*. [24] In a first part, the effective mechanical modulus of sintered colloidal fibers is measured in a three point bending experiment using AFM. In a second part, the fracture properties of the nanofibers are characterized. The results of the AFM experiments are finally compared to the forces and stresses produced within an ultrasonic bath, is used to rupture the fibers into anisometric colloidal particles.

5.1 Nanofiber Morphology

Electrospinned nanofibers are prepared on a calibration microgrid as detailed previously (Chapter 3). Directly after deposition, fibers are composed of 20 nm silica particles embedded in a polyvinylalcohol (PVA) matrix. Furthermore, these fibers contain polystyrene (PS) particles of defined size, which serve as a precursors for voids within the fiber. After heat treatment, silica nanofibers with diameters ranging between 200 to 400 nm (Table 5.1) are obtained. The diameter of the PS particles is measured by Dynamic Light Scattering before addition to the spinning solution. The final sintered fiber diameter is obtained by SEM imaging.

Table 5.1: Morphology

Sample	D_{PS} $[nm]$	D_F $[nm]$
1	–	371 ± 44
2	61 ± 16	239 ± 64
3	256 ± 10	374 ± 49

Fibers without voids are generally thick (Fig. 5.1a-d) whereas fibers with 60 nm voids were clearly thinner (Fig. 5.1b) and less uniform (Fig. 5.1e) than fibers without voids. In particular, superficial holes distributed along the fibers were observed. The fact that the latter fibers were thinner is explained by a higher stretching of the polymer jet experienced during electrospinning due to the higher solution conductivity. Fibers with 260 nm (Fig. 5.1c-f) voids presented diameters comparable to the fibers without voids (Fig. 5.1c), but showed superficial protuberances along the main axis generated by the embedded voids (inset Fig. 5.1c).

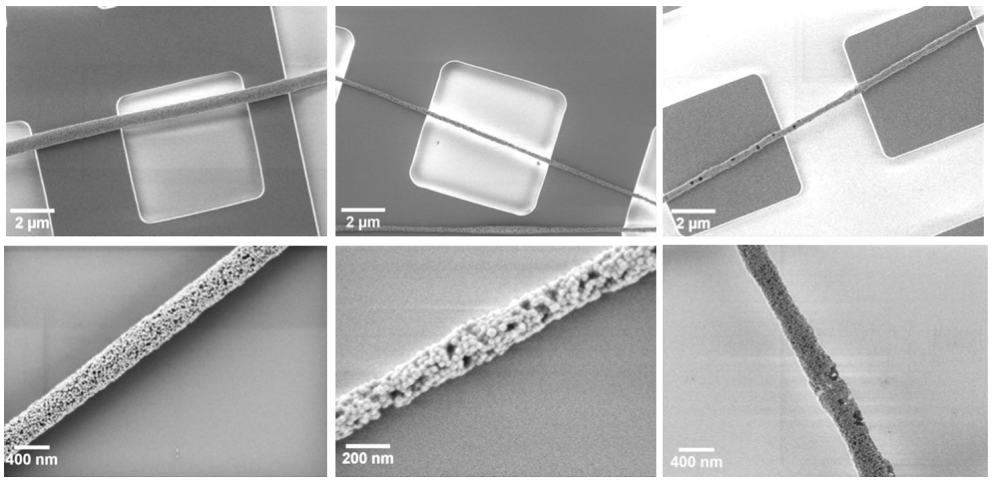

Figure 5.1: *SEM micrographs of colloidal fibers electrospun and sintered on a micro-structured silicon substrate a) without b) 60 nm and c) 260 nm PS generated voids. Images with higher magnification are also shown for each type of fiber: d) without, e) 60 nm and f) 260 nm voids.*

The fibers containing voids are produced using the same concentration of PS particles within the electrospinning dispersion (24 mg/ml) for both 60 and 260 nm PS particles. The final void volume ratio is estimated to be ∼42% of the total fiber for 60 and 260 nm voids, assuming bulk density for silica and polystyrene

particles. However, the voids have different sizes and are differently distributed along the fiber. Considering that 42% of a fibers segment volume consists of voids originating from the sacrificial PS particles, around 4 voids of 260 nm diameter are expected per 10000 sintered silica particles over a 5 μm segment. Therefore, it is expected that on average at least one localized protuberance corresponding to a PS generated void will be obtained over a 5 μm gap. For fibers with 60 nm voids, there are roughly 1000 voids per 3000 sintered silica particles along a 2.5 μm gap. Therefore, the nanofibers are expected to display different mechanical properties depending on the void type, given their different mesostructure.

5.2 Three-point Bending Experiments

After preparing and annealing the fibers over the microstructured grid, three point bending experiments as described in chapter 3 (Fig. 3.9c) are performed. The bending experiments are carried out on microgrids with 10 μm pitch (or 5 μm gap width) for fibers without voids and 260 nm voids. For fibers with 60 nm voids microgrids with a 5 μm pitch (2.5 μm gaps) are used given that these fibers are very brittle and usually break when imaged by AFM on larger freely suspended segments. In all cases the length of the suspended part of the fiber is always at least 10 times the fiber's diameter. Force distance curves are recorded on different positions along the fiber using an AFM cantilever tip (Fig. 5.2a). From such experiments force versus tip-sample distance curves are obtained. Negative tip-sample distances in these curves correspond to fiber deformation (δ_F) (Fig. 5.2b).

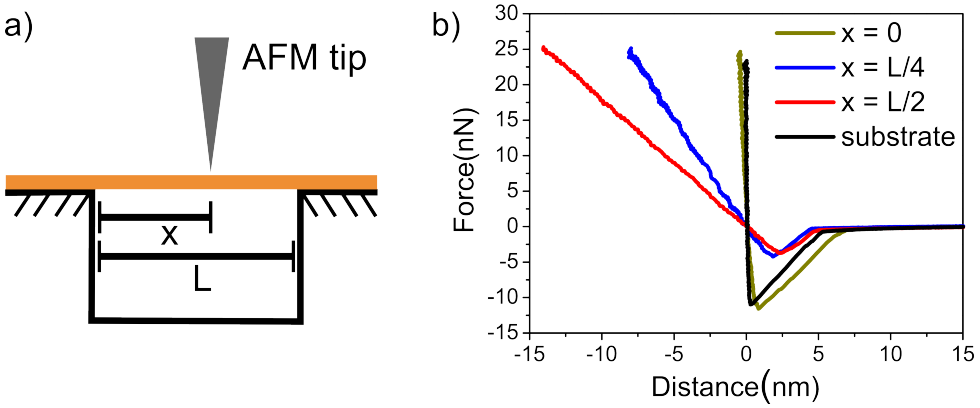

Figure 5.2: *a) Three point bending experiment on a nanofiber with a freely suspended part of length L. The loading position (x) is changed along the fiber and its deformation at that point measured (δ_F). b) Calibrated experimental force curves from such measurements on different positions (x)*

Results obtained with this bending procedure show a linear relation between applied force and fiber deformation. This is a strong indication that the whole fiber is bent rather than indented. Indeed, elastic fiber indentation would lead to force curves with a Hertzian load dependence ($F \sim \delta_F^{3/2}$). Furthermore, no significant hysteresis is observed between the approach and retract parts of the curves, which implies that no indenting nor sliding across the fiber surface takes place. The linear slope of force versus deformation curves for a given position x gives us the stiffness profile ($k_F(x) = F/\delta_F(x)$) of the suspended fiber segment. As expected from beam bending theory, the fiber stiffness decreases as the tip is moved from the supported edge to the center of the suspended fiber segment. This is another

strong indication that measured deformation is due to the bending of the entire suspended segment.

From calibrated force curves the effective position dependent stiffness of the fiber is obtained ($k_F(x)$). Fiber stiffness is plotted against normalized probing position (x/L) along the fiber. In figure 5.3 experimental data is shown for a nanofiber without voids (solid squares). These stiffness profiles ($k_F(x)$) are fitted using beam bending models to extract the fibers Youngs modulus (E). It should be pointed out that this is an effective Youngs modulus of the whole colloidal fiber structure. This effective modulus is expected to be lower than the value for single silica nanoparticles. Although the Youngs modulus in such experiments can, in principle, already be calculated from a single force curve in one defined position, stiffness profiles ($k_F(x)$) give valuable information on the boundary conditions of the suspended fiber and also shows the effects of the presence of the voids.

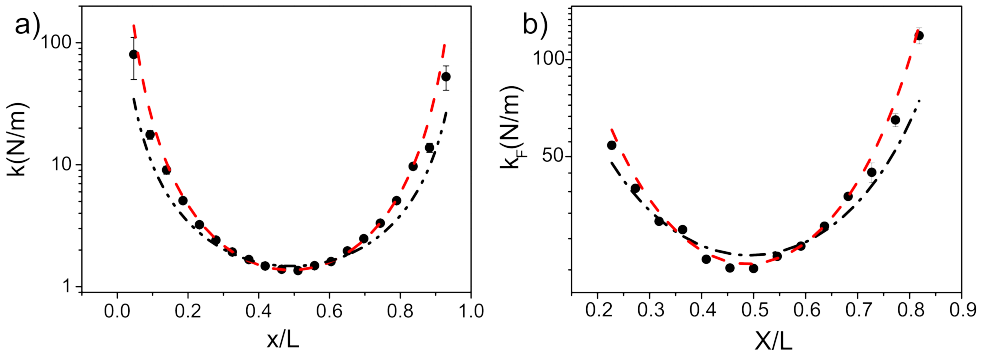

Figure 5.3: *a) and b) shows experimental data (solid circles) for stiffness vs normalized loading position (x/L) for two different nanofibers. Lines represent fits of the experimental data using the double clamped beam model (DCBM, red line) and simply supported beam model (SSBM, black line).*

Classical models used in mechanical three point bending experiments include the double clamped beam model (DCBM) and the simply supported beam model (SSBM), where the fibers are free to slide off the edges (SSBM) or are fixed onto the supporting substrate (DCBM). [76, 77] The DCBM model (Eq. 5.1) and SSBM model (Eq. 5.2) relate stiffness profile ($k_F(x) = F/\delta_F$) to the Young's modulus (E) by:

$$k_F = \frac{3L^3EI}{(L-[x-x_c])^3(x-x_c)^3} \tag{5.1}$$

$$k_F = \frac{3LEI}{(L-[x-x_c])^2(x-x_c)^2} \tag{5.2}$$

where L is the length of the suspended fiber segment and I its second moment of inertia. Assuming that the fiber is a homogeneous cylinder with a radius R, then the moment is given by $I = \pi R^4/4$. The suspended length L and second moment of inertia I can be measured by AM-AFM imaging, prior to bending experiments, and enter the fit as fixed parameters. Meanwhile, x_c is introduced as an additional fitting parameter that accounts for uncertainties in the exact clamping position of the fiber. Using these models fitting results over 4 suspended nanofibers without voids, measured with different cantilevers, are summarized in the following table (Table 5.2):

Table 5.2: Models Stiffness Profile

Fiber	Model	Young's Modulus (GPa)	x_c (nm)	R^2
1	DCBM	2.68 ± 0.03	-88±20	0.94
-	SSBM	11.56 ± 0.24	-68±74	0.84
2	DCBM	7.40 ± 0.09	-70±21	0.92
-	SSBM	31.49 ± 0.56	-47±52	0.84
3	DCBM	7.87 ± 0.23	-286±51	0.65
-	SSBM	34.07 ± 0.49	-382±49	0.92
4	DCBM	5.25 ± 0.16	-293±42	0.74
-	SSBM	23.98 ± 0.30	-302±33	0.95

As seen in table (5.2) the fit coefficient of determination (R^2) for the DCBM or SSBM is not enough to choose which of them is more suitable. On one hand, the DCBM gives Young's modulus values around 5 GPa, while SSBM yields considerably larger values of around 30 GPa. Additional experiments are required in order to rule out one of these models. For this purpose, a scratch experiment is performed. In this experiment stiff AFM cantilever is attached to a 3-axis oil

micromanipulator (Narishige) while recording optical images of the fiber as the cantilever's tip is passed across surface in mechanical contact. From optical images (Fig. 5.4a-b) it is seen that the sintered fiber is ruptured instead of being displaced. This indicates that the colloidal nanofibers are fixed onto the silica substrate on which it is sintered. The blue color of the fiber is produced by the elastic scattering of white light from the silica nanoparticles (20 nm diameter) that compose the nanofiber, i.e. Rayleigh scattering.

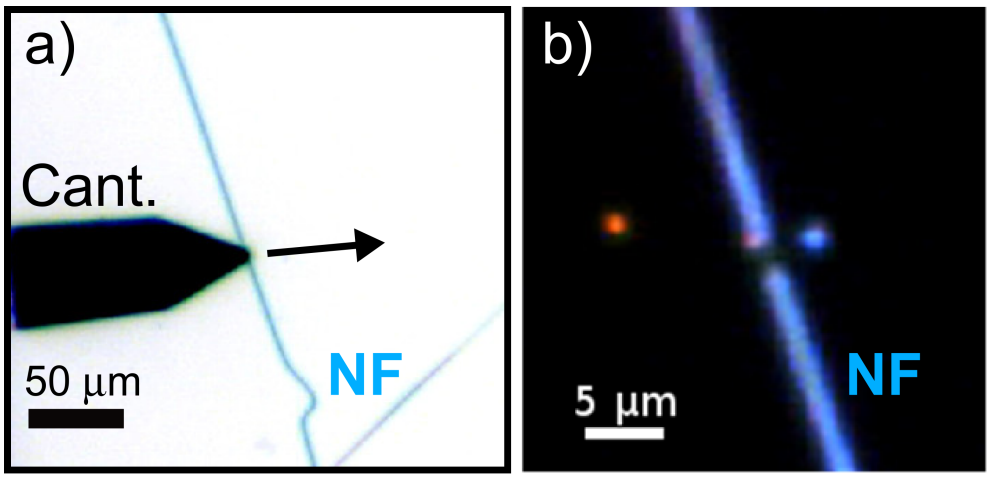

Figure 5.4: *a) Optical image of the colloidal nanofiber (NF), seen as a light blue colored line, supported on a silicon substrate (white background). An AFM cantilever (Cant.) is passed across it in mechanical contact. b) Darkfield optical image of the nanofiber (NF) after passing the cantilever.*

This last experiment (Fig. 5.4) yields evidence that the fibers are fixed on the substrate after sintering, which indicates that the DCBM is a more suitable description of the experimental data. Further results shown from hereon are obtained using the DCBM.

Differences in the shape of the stiffness profile ($k_F(x)$) are observed for the different types of voids. For each type of void, four different segments of fiber using different cantilevers are measured (Fig. 5.5). By normalizing the vertical axis by the curves minimum ($k_F(x)/k_{Fmin}$) and the horizontal axis by the suspended length (x/L), the different measurements are combined onto a single master plot. Differences in the shape of the stiffness profile ($k_F(x)$) are observed for the different types of voids. For each type of void, four different segments of fiber using different cantilevers are measured (Fig. 5.5).

For fibers without voids (Fig. 5.5a), the curves collapse on a single plot with

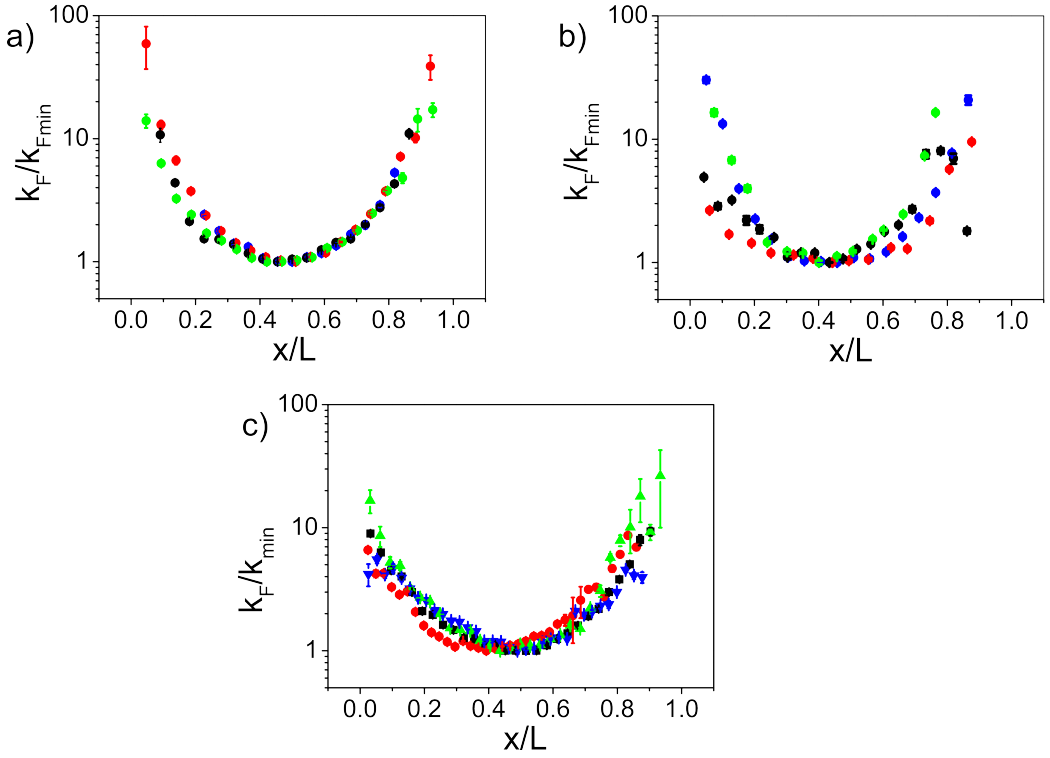

Figure 5.5: *Normalized stiffness profiles $k_F(x)/k_{min}$ for fibers a) without voids, b) 60 nm voids and c) 260 nm voids.*

minimal variations between the curves. By fitting each curve separately an average Youngs Modulus of E= 5.54 ± 2.14 GPa is obtained. This value is much lower than the ∼40 GPa [78] reported for single silica microcapsules sintered at 873 K. This lower value is expected because the effective modulus of the fiber was probed and not the modulus of the individual silica particles. For fibers with 60 nm voids (Fig. 5.5b), the master curve maintained the U-type shape centered at $(x/L = 0.5)$, but there is much more variation between the different curves than in the case of fibers without voids. An averaged Youngs modulus of 0.73 ± 0.27 GPa, is obtained for these fibers after fitting each curve separately. The introduction of 60 nm voids produced overall a much softer fiber than fibers without voids. For fibers with 260 nm voids (Fig. 5.5c), normalized curves broaden, but do not show as much variation between curves as in fibers with 60 nm voids. It is seen that 260 nm voids affect the shape and center position of the normalized curves. An average Youngs modulus of 1.3 ± 0.5 GPa was calculated for these samples. Although a 260 nm void is comparable to the fibers radius, the Youngs modulus of such samples is slightly higher than for samples with 60 nm voids. This is due to the fact that the 260 nm voids are not evenly distributed along the fiber, but act as localized defects. Such fibers are still homogeneous apart

from the positions where 260 nm voids are found. On the other hand, in samples with 60 nm voids, defects are evenly distributed along the fiber given the large concentration of voids. Indeed, roughly 1 void exists per every 3 silica particles as estimated from the concentration of PS particles in the electrospinning solution.

5.3 Fracture Properties of Nanofibers

In addition to the mechanical modulus, fracture properties of nanofibers are investigated. In order to fracture these fibers, increasingly higher forces are applied with the AFM tip at the middle of the suspended fiber segment ($x = L/2$). In order to apply increasingly higher loads on the suspended fiber, the z-piezo ramp size is kept constant and the center position of this ramp is moved closer to the surface of the substrate. This gives rise to higher loads on the fiber with each successive force curve. Doing so, the maximum force which the fiber resists before breaking is measured. In figure 5.6 the rupture happens after the maximum load is reached, as marked by the dashed circle (Fig. 5.6). Subsequent force curves become non-linear in the loading part, suggesting yielding of the fiber.

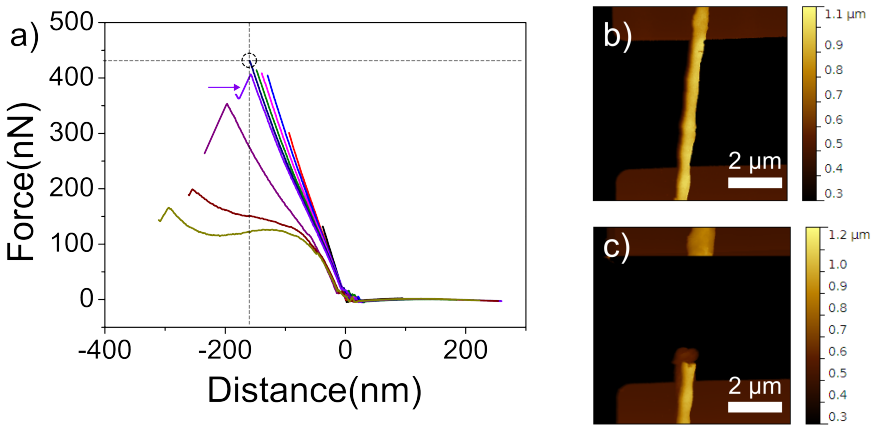

Figure 5.6: *a) Increasing force curves up until fiber rupture is achieved. The fiber is imaged b) before and c) after it is ruptured using AM-AFM.*

The maximum stress within the fiber can be estimated by assuming that it is equal to the surface stress at the clamping point. According to beam mechanics, the stress within a rigid beam (σ_F) is proportional to its radius of curvature ($\kappa = 1/R$). The radius of curvature can be in turn approximated by the second derivative of the deformation profile ($\delta_F(y)$), resulting in:

$$\sigma_F(y, z) = Ez\frac{d^2\delta_F}{dy^2} \tag{5.3}$$

where y is an arbitrary position along the fiber and z is the distance from the neutral axis of the beam. The deformation profile ($\delta_F(y)$) when a load is applied at the center of the suspended piece ($x_0 = L/2$) is:

$$\delta_F(y) = \frac{Fx_0^2}{48EI}(3L - 4y) \tag{5.4}$$

A value for the maximum stress right before the fiber is ruptured can be estimated by combining equations 5.3 and 5.4 and evaluating it at the surface of the clamping point ($\sigma_F(0, R)$), where the stress maximum occurs.

In the case of fibers without voids where two fragments of fiber are left after failure (Fig. 5.7a) a maximum stress of 44-51 MPa is calculated. When the fibers without voids ruptures leaving three fragments (Fig. 5.7b) the maximum stress is estimated to be 120 MPa, roughly the double of last case.

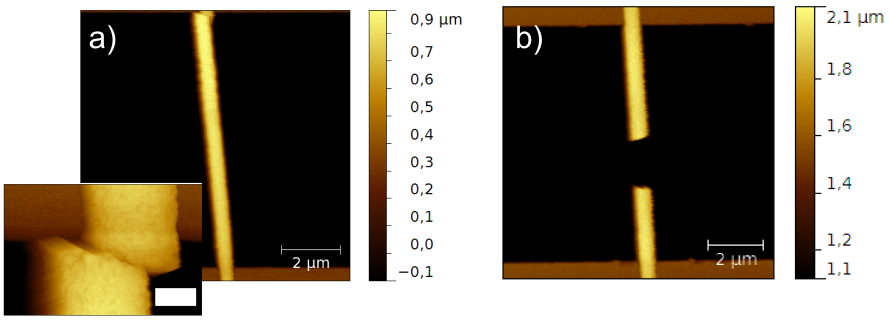

Figure 5.7: *Fiber without PS generated voids. Fibers may rupture leaving a) 2 or b) 3 segments. Scale bar of inset is 200 nm*

For fibers with 260 nm voids a maximum stress of 17 MPa is calculated before rupture, when two fragments are left (Fig.5.8a) and 30 MPa when three segments are produced (Fig. 5.8b). The fracture in such fibers is usually produced near the voids as seen in the inset.

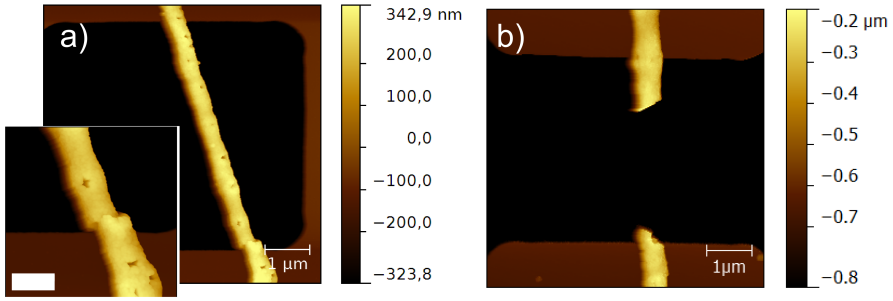

Figure 5.8: *Fiber with 260 nm PS generated voids. a) Rupture of the fiber leaves 2 (Inset scale bar is 500 nm) and b) 3 segments.*

Finally, for fibers with 60 nm voids, three segments of fiber are always obtained after their fracture (Fig. 5.9a). The maximum stress in this case is 25 MPa. The fact that nanofibers fracture into two or three pieces resembles the fragmentation of spaghetti rods which can also randomly break in two, three or even more pieces. [79, 80]

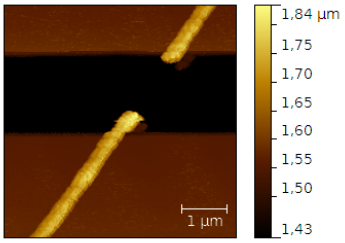

Figure 5.9: *Fibers with 60 nm PS generated voids.*

In a final calculation, the yield strength calculated from the AFM fracture experiments (∼50 MPa) are compared to pressures involved in sonication experiments previously described. [24] In such experiments, sintered colloidal nanofibers are dispersed in water and sonicated to produce fragmented rod-shaped anisometric particles. The sonicator consists of a cylindrical resonator, vibrating at 20 kHz, 0.3 cm radius immersed 2.5 cm within an aqueous solution. Given this geometry and the sonication power of 100 Watt, an intensity of I=20 Watt/cm^2 is estimated. This intensity relates to the maximum acoustic pressure P_m within the solution by: [81]

$$I = \frac{P_m^2}{2\rho c} \tag{5.5}$$

where ρ and c are the density and ultrasound wave velocity of water. Using this equation a maximum acoustic pressure of ∼0.8 MPa is estimated. This is clearly not enough stress to produce the fracture of fibers (∼50 MPa). Nevertheless, it is known that at ultrasonic frequencies of 20 kHz and intensities of 20 Watt/cm^2, transient cavitation bubbles are produced within the liquid. [82] Cavitation bubbles are known to generate pressures well over 100 MPa upon collapse and have sizes ranging from 0.1 μm to 100 μm. [83, 84] These pressures are then large enough to fracture the fibers. Reported bubble sizes are also comparable to the diameter size of our fibers (0.4 μm). Given that SPM three-point bending experiments give an estimation of the surface stress needed to rupture calcinated fibers (∼50 MPa) and that maximum ultrasound pressure is not large enough to rupture the fibers (P_m=0.8 MPa), it is concluded that the mechanical rupture of fibers within a sonic bath can be only induced by the cavitation effect.

Chapter 6

Biomineral Mechanics

Within this chapter, the mechanical properties and protein content of calcareous biominerals are studied. Needle-like biominerals, referred to as spicules, are synthetically grown using the protein silicatein-α, which is a surprising result given that silicatein-α is known to be involved in the mineralization of silica [31] and was not expected to work with calcium carbonate. Such synthetic spicules have similar dimensions as the ones found in the calcareous marine sponge *Sycon sp.*. Both natural and synthetic spicules have a length of 100 μm and diameters of around 5-10 μm. In the first part of the chapter (6.1) the mechanical properties, i.e. Young's modulus and fracture properties, of natural and synthetic spicules are studied using a clamped spicule setup described in previous chapters (3.6). In the second part of this chapter (6.2) the protein content within single spicules is measured by SPM based nano-TGA.

6.1 Spicule Mechanics

The mechanical properties of single spicules have been studied before; however, these studies have been limited to spicules large enough to allow macroscopic testing. The Young's modulus of siliceous sponge spicules is found to be close to 40 GPa in most cases [85, 86, 87], but values of 14 GPa [88] and 68 GPa [89] have also been reported. Little is known about the mechanical properties of calcareous spicules from marine species; a value of 36 GPa has been reported for spicules from echinoderm larvae [90].

The mechanical properties of natural and synthetic calcareous spicules are studied here with an SPM, given that their length ($\sim$100 μm) impedes macroscopic bending experiments. A procedure to clamp individual spicules to the edge of a silicon wafer is developed using a small drop of two-component epoxy glue, as described in chapter 3 (Fig. 3.6). In this configuration, the spicule acts as a flexible beam of length L. [92] A tipless AFM cantilever is then used to apply a

force F at a distance x from the wafer edge (inset Fig. 6.1). Force-versus-beam deflection curves are then recorded for a series of positions along the spicules as described in chapter 3 (Fig.3.7). According to beam theory, the applied force F and the induced beam deflection δ_s at the loading position x of a one-sided clamped beam are related by equation 2.11 (Chapter 2). If the beam is considered to be a homogeneous cylinder of radius R this equation reduces reduces to:

$$F_s = \frac{3\pi E R^4}{4x^3}\delta_S \tag{6.1}$$

Force versus deflection of clamped spicule beam are shown in figure 6.1 for 3 loading positions (x). In such experiments a linear relation between applied force and induced beam deflection is observed.

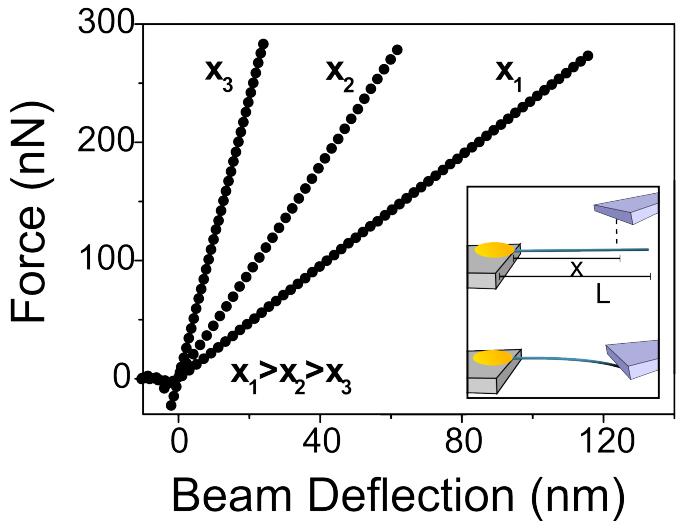

Figure 6.1: *Force versus beam deflection curves recorded at different positions along a clamped spicule cantilever. Inset: sketch of the measurement arrangement for spicule bending tests.*

As seen above, the slope of such force curves decreases as the position x approaches the free end of the spicule. Such slopes are defined as the effective stiffness of the spicule ($k_s = F/\delta_s$). By linearly fitting force curves at several positions (x) along the clamped spicule, the effective stiffness as a function of the normalized position x/L is plotted (Fig. 6.2a-b). The Young's modulus E of the spicules is then calculated by fitting such stiffness versus position curves using a cantilever beam model equation:

$$k_s = \frac{3\pi E R^4}{4(x - x_0)^3} \tag{6.2}$$

This last equation has been adapted from equation 6.1, where the Young's modulus E and x_0 are fitting parameters, while R is obtained from optical images of the clamped spicule. The parameter x_0 is introduced as an offset to correct for uncertainties in the of distance from the clamping point. Typical values of x_0 are in the range of 10 to 30 μm for both synthetic and natural spicules. Using this method, a Young's modulus for a natural spicule of 8.8±0.9 GPa is obtained (Fig. 6.2a). On the other hand, for synthetic spicules a Young's modulus of E= 14.2 ± 0.8 GPa is obtained for a spicule sample measured one month after its synthesis (Fig. 6.2b). The Young's modulus of synthetic spicules is lower than the one found in natural echinoderm spicules (36 GPa) [90] but higher than for spicules from the Sycon *sp.* monoaxons.

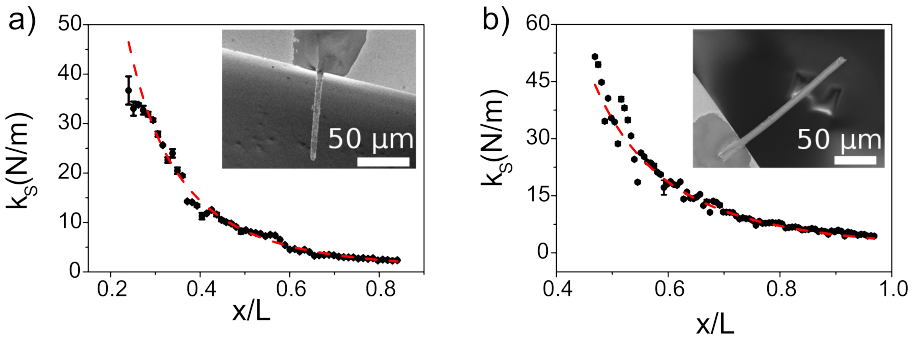

Figure 6.2: *Stiffness profiles (black solid circles) for a) a natural and b) a synthetic spicule, with their respective fits (dashed red lines). Inset shows an optical micrograph of the corresponding clamped spicule configuration.*

One important finding is that synthetic spicules age over months after their synthesis. The main signatures of this aging are seen by x-ray diffraction and polarized light microscopy, where fresh spicules show no clear crystal forming signatures when freshly prepared, i.e. diffraction peaks. As time passes (months), and synthetic spicule age, clear signs of crystalline structure show up in both polarized light microscopy and x-ray diffraction experiments. [28] Such aging time is estimated to be from 3 to 7 months and is also observed in the mechanical properties of the spicules. The mechanical modulus of freshly prepared and aged spicules is probed with SPM (Fig. 6.3). For a fresh synthetic spicule, less than a week old, a Young's modulus of E= 3.0±0.5 GPa is measured (Fig. 6.3a); while, for a 7-month-old sample a Young's modulus of E=19±4 GPa is obtained (Fig. 6.3b). This result shows that the Young's modulus of the synthetic spicules increases with time and that this is related to the formation of the calcite nanocrystals within them.

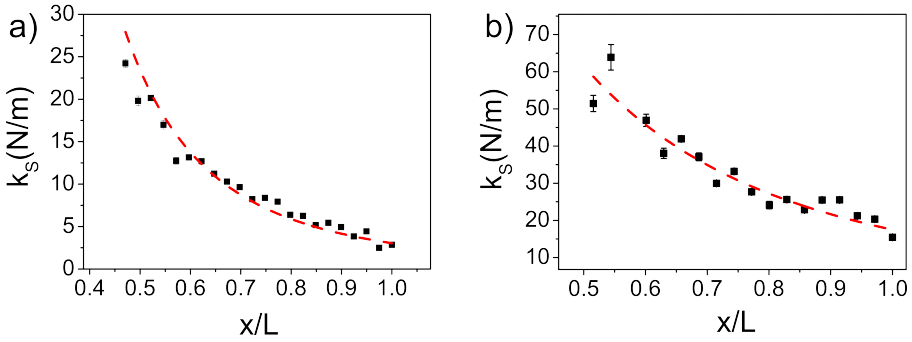

Figure 6.3: *Stiffness profiles for synthetic spicules that are a) fresh (less than one week old) and b) aged for 7 months. Dashed red lines are the respective fits using equation 6.2*

To probe the fracture properties of spicules, they are bent within a SEM using a micromanipulator (MM). Natural spicules (NS) fracture in a brittle way when deflected by $\delta_S/L = 11\%$. (Fig. 6.4).

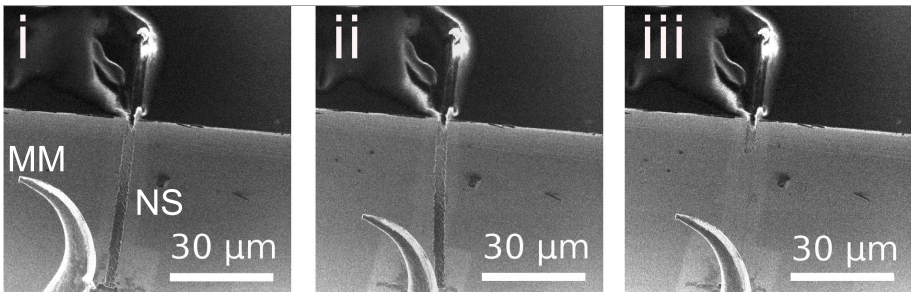

Figure 6.4: *(i-iii) Sequence of bending steps using a micromanipulator (MM) for a natural spicule (NS) recorded by SEM. The spicule fractures in iii.*

Assuming a linear stress-strain curve up to fracture and using the measured Young's modulus for the natural spicules, a maximum stress of σ=89 to 125 MPa is calculated at the clamping point before fracture. In order to estimate this value, the Young's modulus is measured using the SPM bending procedure previous to the fracture experiment. After frature, SEM analysis of the natural spicule shows, instead of a crystal fracture, a clear glassy conchoidal fracture (Fig. 6.5b-c). Similar behavior has been observed for glass sponge fibers and echinoderm spicules and attributed to a combination of mesocrystallinity and organic content. [91]

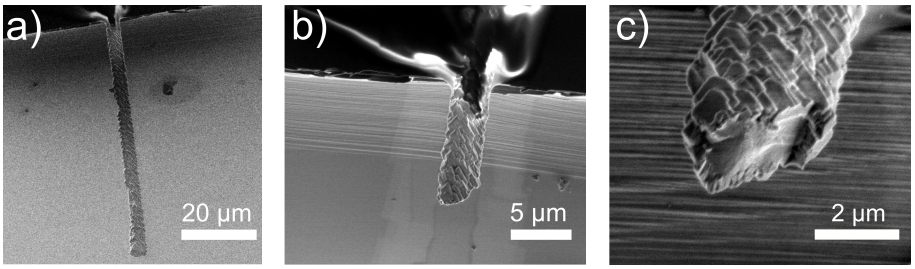

Figure 6.5: *SEM images of a Natural spicule a) before fracture and b), c) after fracture.*

On the other hand, synthetic spicules (AS) show no signs of fracture or plastic deformation, up to $\delta_S/L = 18\%$. This corresponds to a maximum applied stress of σ=170 MPa.

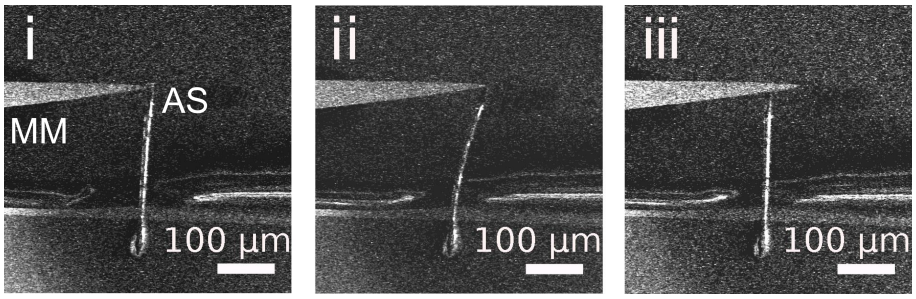

Figure 6.6: *(i-iii) Sequence of bending steps for a synthetic spicule (AS) seen with SEM. The micromanipulator (MM) slides over AS in iii.*

Even when bending a synthetic spicule to a U-shape (Fig. 6.7i-vi), no fracture is produced. Instead of brittle failure, only elastic bending with a small plastic component is observed, i.e. after 180^o bending and release, the spicule shows a plastic deformation of $\delta_S/L \sim 10\%$ (Fig. 6.7vi).

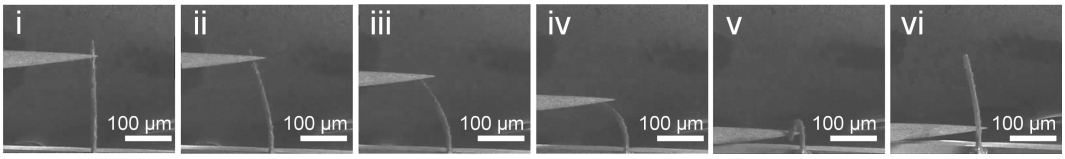

Figure 6.7: *Sequence of SEM images of synthetic spicule under extreme deformations.*

As seen, synthetic spicules are mechanically more resistant than natural ones. In order to understand such differences in bending properties, knowledge of the amount of organic content within single spicules is relevant. To measure this, a nano-TGA procedure is introduced.

6.2 Protein Content: Nano-TGA

In order to compare the protein content between natural and synthetic spicules, freshly prepared single spicules are loaded on the backside of a cantilever employing a micromanipulator. After this, spicule loaded cantilevers are heated to high enough temperatures in order to remove the organic content. Such a procedure is detailed in chapter 3 (3.2.1) and is referred to as nano-TGA, given the small changes in mass that are detectable (<1 ng). To rule out mass changes due to organic contaminants on the cantilever or growth of silicon oxide, a control experiment is first performed. A cantilever without spicule is used and its resonance frequency is measured prior to calcination (step 1 Fig.6.8), and after 2 successive calcination steps at 773 K (step 2 and 3 Fig.6.8). The resonance frequency of the unloaded cantilever is hardly affected by the 2 subsequent calcination steps. Only variations of ∼10 Hz are observed. Changes in the resonance frequency due to a loaded spicule are much larger than these variations as shall be shown next.

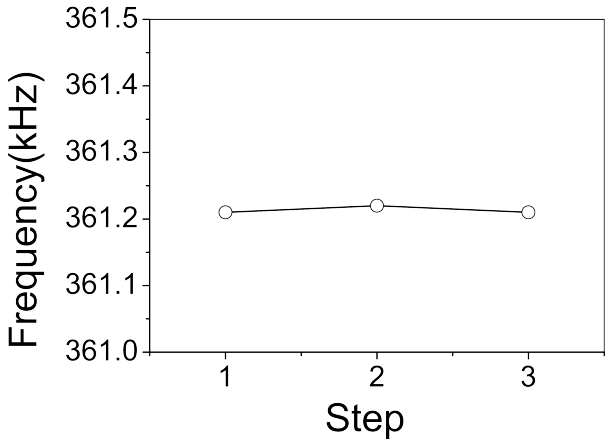

Figure 6.8: *Resonance frequency of a bare cantilever without spicule is measured before (step 1) and after 2 subsequent calcination cycles at 773 K (steps 2 and 3)*

Nano-TGA experiments are first carried out on a natural spicule (Fig. 6.9). The first resonance frequency measurement (step 1 Fig. 6.9a) is performed on a different AFM, where cantilever's spring constant is obtained using the thermal noise method. The different AFM employed in the first frequency measurement may explain the initial variation in the resonance frequency (∼1 kHz) between steps 1 and 2 . The following steps (2, 3 and 4) are measured on the same AFM without moving the cantilever from its holder. The resonance frequency of the cantilever-spicule system is measured after the spicule is loaded (step 3) and after calcination for 10 minutes at 773 K (step 4), as shown in figure 6.9(a). Using equations 3.4 and 3.5 from chapter 3, a mass of 17.3 ng is calculated for this natural spicule. Employing an optical image of the natural spicule before calcination (Fig. 6.9b) and assuming a cylindrical cross-section, a density of 2.5 g/cm^3 is calculated, which is close to that of pure calcium carbonate (2.7 g/cm^3). After calcination a rise in the resonance frequency is observed (step 3 to 4 Fig.6.9a), which corresponds to a mass loss of 0.26 ng. This loss corresponds to 1.5% of the original mass of the spicule and is attributed to its protein content. It it worth pointing out that no significant change in natural spicule shape is seen after calcination (Fig. 6.9c). This measurement is repeated for a second natural spicule, where a similar density result is obtained prior to calcination: 2.4 g/cm^3. The agreement between natural spicule density, measured with nano-TGA, and that of pure calcium carbonate validates the use of the AFM cantilever as a nano-balance.

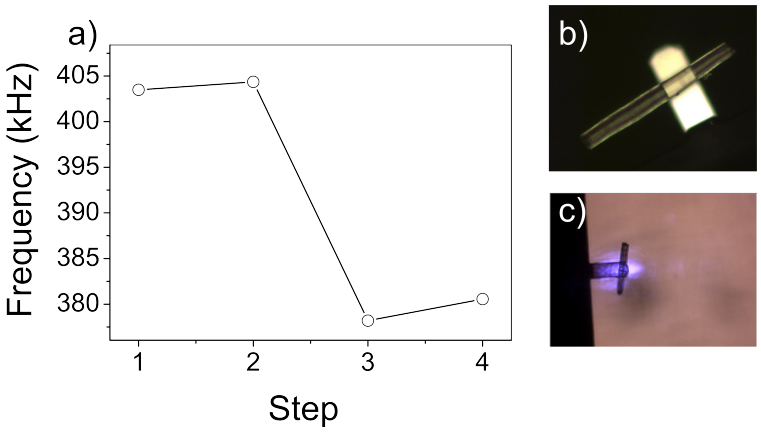

Figure 6.9: *Resonance frequency of a cantilever loaded with a natural spicule. Step 1 and 2: Original resonance frequency. Step 3: Spicule is loaded on the backside of the cantilever. The observed drop in frequency of 26 kHz corresponds to a mass of 17.3 ng. Step 4: Resonance frequency rises 2 kHz after the spicule is calcinated once at 773 K. This resonance shift corresponds to a change in mass of 0.26 ng.*

The same procedure is carried out with the synthetic spicule (Fig. 6.10). Variations between step 1 and 2 are attributed to the different AFMs used to measure these two frequencies. Steps 2, 3 and 4 are measured on the same AFM without moving the cantilever from its holder, as described before. An original mass of 10.2 ng is measured for the synthetic spicule after loading it onto the cantilever (step 3 Fig. 6.10a). Using an optical image before calcination, a density of 0.6 g/cm^3 is estimated. After calcination, a greater rise in the resonance frequency of the cantilever is measured, as shown in steps 3 to 4 (Fig. 6.10). Such rise in resonance frequency corresponds to a mass loss of 1.01 ng. This means 9.9% of the original mass is lost after calcination, which is attributed to its protein content. Optical images of the synthetic spicule before and after calcination shows that the spicule considerably shrinks after heat treatment (Fig. 6.10b-c). After calcination, a density of 1.7 g/cm^3 is estimated from optical micrographs. A densification of the synthetic spicule is observed after it loses its organic content.

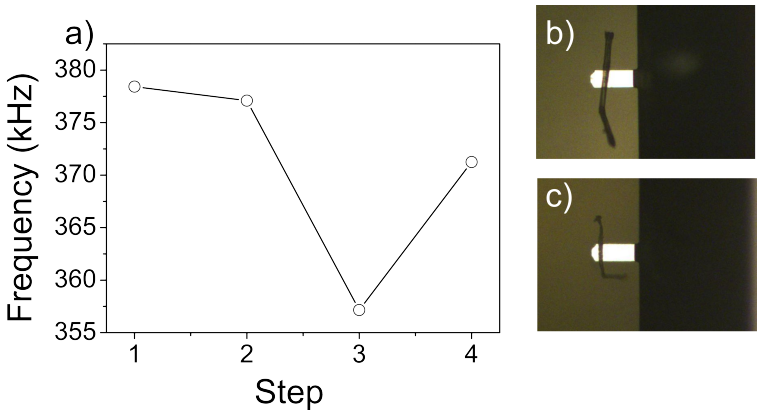

Figure 6.10: *Resonance frequency of a cantilever loaded with a synthetic spicule. Step 1 and 2: Original resonance frequency. Step 3: Spicule is loaded on the backside of the cantilever. Step 4: Resonance after the spicule is calcinated once at 773 K*

This experiment is repeated on another synthetic spicule and a similar density before calcination is obtained (0.6 g/cm^3). Furthermore, the protein content for this second synthetic spicule amounted to 15.6% of the original mass measured before calcination.

From these measurements it is concluded that synthetic spicules have around 10 times more organic content than natural spicules. This in part explains their higher mechanical resistance to extreme deformations, as found in the bending experiments (Figs. 6.7 and 6.4).

Chapter 7

Conclusions and Outlook

Throughout this work, it has been shown that *scanning probe microscopy* (SPM) is a powerful tool to extend classical macroscopic testing experiments, such as broadband dielectric spectrosocpy (BDS), flexural testing or thermal gravimetric analysis (TGA), to mesoscopic length scales. The main advantage of SPM is that it is possible to investigate samples that are spatially limited to length scales of the order of the SPM tip (5 nm) or the cantilever (50 μm). This is of interest in the field of mesostructured materials for several reasons, i.e. to probe molecular dynamics with local resolution (Chapter 4) or perform bending experiments on micrometer sized structures (Chapter 5 and 6).

In chapter 4, SPM has been combined with dielectric spectroscopy (local-DS) to measure molecular dynamics in a thermally activated polymer blend such as PVAc/PEO. It is shown that local-DS is sensitive to the presence of dynamic heterogeneity within miscible blending ratios of PVAc/PEO. Furthermore, with local-DS it is possible to deduce the local blend composition of the film with a mesoscopic lateral resolution (100 nm). The sensitivity of local-DS to blend composition is employed to quantitatively account for the kinetics of phase separation in thin PVAc/PEO films. It is shown that phase separation is driven by surface crystallization of PEO. These results open new possibilities for using local-DS to study polymer blend surface segregation, kinetics of phase separation, and even interdiffusion and adhesion at polymer-polymer interfaces as a function of annealing temperature. Relating topographical and compositional information is of major interest in the field of self-assembly[93], in order to unveil underlying materials which are not recognizable solely from topographical imaging. Although local-DS has proven useful for obtaining dielectric spectra of PVAc and miscible blends of PVAc/PEO, further improvements to the technique are still possible. A first improvement would be to extend the frequency sweep to cover broader frequency ranges. Currently, only 4 decades of frequency are accessible with local-DS. A second improvement would be to develop a way to keep the

tip-sample distance constant while sweeping in frequency. Constant tip-sample distance would help to access lower frequencies, which require longer acquisition times, and therefore study segmental dynamics near the glass transition temperature. Possible deviations from non-Arrhenius dynamics are expected to be more pronounced near the glass transition temperature and are attributed to growing length scales of mesoscopic heterogeneities.

SPM three point bending experiments are shown in chapter 5 for nanofibers with introduced voids. Voids within the nanofiber are created by the removal of sacrificial polymer particles. It is shown that size and distribution of the voids within the nanofiber play an important role in its Young's modulus and fracture properties. Furthermore, fracture stress is calculated and compared with previously reported experiments, in which nanofibers are sectioned using ultrasonication.[24] Using this comparison, it is shown that fragmentation of nanofibers within an ultrasonic bath can only be produced by the cavitation effect. The determination of the mechanical properties of nanofibers is helpful in order to develop new methods to fragment them into controlled anisometric sizes. Furthermore, these results open new ways of studying the mechanical effects of defects within nanofibers. Although SPM has been shown capable of measuring the effective Young's modulus and fracture properties of nanofibers, imaging the fiber after fracture is hindered by tip-contamination. Future experiments would be aided by using SPM setups working within a SEM chamber.[94, 95] This way, mechanical bending and fracture is performed by the SPM tip, while the imaging of the nanofiber after fracture is done with SEM. By doing so, a clearer picture on how colloidal nanofibers fracture could be obtained.

The mechanical properties of synthetic and natural biomineral spicules are measured using SPM in chapter 6. A procedure to study their bending mechanics is developed with SPM. It is found that, although Young's modulus of natural and synthetic spicules are comparable ($\sim$ 10 GPa), synthetic spicules mechanically stiffen with time, i.e. aging. It is found that mechanical aging of synthetic spicules coincides with the time required for these spicules to show x-ray diffraction patterns, in other words, the formation of nanocrystalline regions within the spicule.[28] Fracture properties of natural and synthetic spicules are also tested. Natural spicules typically fracture after deformations of around 10% of their total length. On the other hand, synthetic spicules are remarkably more resistant to deformation, showing no fracture and little plastic deformation after U-type bending. In order to understand such differences in mechanical resistance, a thermal gravimetric analysis (nano-TGA) procedure using SPM is developed. Using nano-TGA it is found that synthetic spicules have at least 10 times more protein content than natural spicules. It is shown that protein content, plus the hierarchical microstructure, determine how natural and synthetic spicules react to large

deformations. The nano-TGA method is an interesting technique to measure the protein content of single biominerals. One of the major drawbacks of nano-TGA, as described in chapters 3 and 6, is that the spicule loaded cantilever must be transported from the SPM to the oven where it is calcinated. This means, nano-TGA as described here does not yield information on how the mass changes with temperature, but only gives information on organic content before and after calcination. It would be of interest, for future applications, to implement a dedicated experiment where the resonance frequency of the cantilever is measured in-situ while heating the sample. Such an experiment would yield the change in mass of the cantilever as a function of temperature. One possible approach might be the lithographic integration of a resistive heating element into an AFM cantilever.

Understanding how single atoms give way to the complex architectures, phenomena and functionalities that control macrosocpic materials is the essence of mesoscale science.[2] Overall, SPM has shown to be a versatile tool for studying materials, in which, dielectric and mechanical properties are deeply controlled by their relevant mesostructures.

Bibliography

[1] Antonietti M. & Ozin G. A., 2004, Promises and problems of mesoscale materials chemistry or why meso?, *Chemistry A European Jouranl*, 10(1), 2841. doi:10.1002/chem.200305009

[2] Crabtree, G. W. & Sarrao, J. L., 2012, Opportunities for mesoscale science, *MRS Bulletin*, 37(11), 10791088. doi:10.1557/mrs.2012.274

[3] Piazza R., 2011, Soft Matter: The stuff that dreams are made of, ISBN 978-94-007-0584-5. *Springer Science+Business Media B.V.*

[4] Weiner S. & Addadi L., 2011, Crystallization Pathways in Biomineralization. Annual Review of Materials Research, 41(1), 2140. doi:10.1146/annurev-matsci-062910-095803

[5] Berthier L. & Biroli G., 2011, Theoretical perspective on the glass transition and amorphous materials, *Reviews of Modern Physics*, 83(2), 587645. doi:10.1103/RevModPhys.83.587

[6] Addadi L. & Weiner S., 2001, Crystals, asymmetry and life, *Nature*, 411(6839), 753, 755. doi:10.1038/35081227

[7] Moffitt J. R., Chemla Y. R., Smith S. B. & Bustamante, C., 2008, Recent advances in optical tweezers, *Annual review of biochemistry*, 77, 20528. doi:10.1146/annurev.biochem.77.043007.090225

[8] Gentile F., Moretti, M. Limongi, T. Falqui, A., Bertoni G., Scarpellini A., Santoriello S., Maragliano L., Zaccaria R.P. & Fabrizio E.D., 2012, Direct imaging of DNA fibers: the visage of double helix, *Nano letters*, 12(12), 64538. doi:10.1021/nl3039162

[9] Mezger M., Ocko B. M., Reichert H. & Deutsch M., 2013, Surface layering and melting in an ionic liquid studied by resonant soft X-ray reflectivity, PNAS, 110(10), 37337. doi:10.1073/pnas.1211749110

[10] Best A., Pakula T. & Fytas G., 2005, Segmental Dynamics of Bulk Polymers Studied by Fluorescence Correlation Spectroscopy, *Macromolecules*, 38 (10), 4539-4541. doi: 10.1021/ma047430k

[11] Fox T.G.Jr. & Flory P.J., 1948, ViscosityMolecular Weight and ViscosityTemperature Relationships for Polystyrene and Polyisobutylene, *J. Am. Chem. Soc.*, 70 (7), 23842395, doi: 10.1021/ja01187a021.

[12] Kremer F. & Schoenhals A., 2003, Broadband Dielectric Spectroscopy, *Springer Verlag*.

[13] Ediger M.D, 2000, Spatially Heterogeneous Dynamics in Supercooled Liquids, *Annu. Rev. Phys. Chem.*, 51: 99-128. doi: 10.1146/annurev.physchem.51.1.99

[14] Tracht U., Wilhelm M., Heuer A., Feng H., Schmidt-Rohr K. & Spiess H, 1998, Length Scale of Dynamic Heterogeneities at the Glass Transition Determined by Multidimensional Nuclear Magnetic Resonance, *Physical Review Letters*, 81(13), 27272730. doi:10.1103/PhysRevLett.81.2727

[15] Walther L., Israeloff N., Vidal Russell E. & Alvarez Gomariz H., 1998, Mesoscopic-scale dielectric relaxation at the glass transition. *Physical Review B*, 57(24), R15112R15115. doi: 10.1103/PhysRevB.57.R15112

[16] Rubinstein M. & Colby R.H., 2003, Polymer Physics, *Oxford University Press*

[17] Lodge T. P. & McLeish T. C. B., 2000, Self-Concentrations and Effective Glass Transition Temperatures in Polymer Blends, *Macromolecules*, 33(14), 52785284. doi:10.1021/ma9921706

[18] Zardalidis G. & Floudas G., 2012, Pressure Effects on the Dynamic Heterogeneity of Miscible Poly(vinyl acetate)/Poly(ethylene oxide) Blends, *Macromolecules*, 45(15), 62726280. doi:10.1021/ma301086a

[19] Arbe A., Alegría A., Colmenero J., Hoffmann S., Willner L. & Richter D., 1999, Segmental Dynamics in Poly(vinylethylene)/Polyisoprene Miscible Blends Revisited. A Neutron Scattering and Broad-Band Dielectric Spectroscopy Investigation, *Macromolecules*, 32 (22), 7572-7581. doi: 10.1021/ma990402v

[20] Zetsche A. & Fischer E.W., 1994, Dielectric studies of the α-relaxation in miscible polymer blends and its relation to concentration fluctuations. *Acta Polymerica*, 45, 168175. doi: 10.1002/actp.1994.010450306

[21] Poon W., 2004, Colloids as big atoms, *Science*, 304(5672), 8301. doi:10.1126/science.1097964

[22] Lu P. J. & Weitz D. A., 2013, Colloidal Particles: Crystals, Glasses, and Gels, *Annual Review of Condensed Matter Physics*, 4(1), 217233. doi:10.1146/annurev-conmatphys-030212-184213

[23] Chithrani B. D., Ghazani A. & Chan W. C. W., 2006, Determining the size and shape dependence of gold nanoparticle uptake into mammalian cells. Nano letters, 6(4), 6628. doi:10.1021/nl052396o

[24] Friedemann K., **Corrales T.**, Kappl M., Landfester K. & Crespy D., 2012, Facile and large-scale fabrication of anisometric particles from fibers synthesized by colloid-electrospinning, *Small*, 8(1), 14453. doi:10.1002/smll.201101247

[25] Aizenberg J., Hanson, J., Koetzle T. F., Leiserowitz L., Weiner S. & Addadi L., 1995, Biologically induced reduction in symmetry: A study of crystal texture of calcitic sponges, *Chemistry a European Journal*, 7, 414-422. doi: 10.1002/chem.19950010705

[26] Young J., Davis S., Bown P. & Mann S., 1999, Coccolith ultrastructure and biomineralisation, *Journal of Structural Biology*, 126(3), 195215. doi:10.1006/jsbi.1999.4132

[27] Noorduin W. L., Grinthal A., Mahadevan L. & Aizenberg J., 2013, Rationally Designed Complex, Hierarchical Microarchitectures, *Science*, 340(6134), 832837. doi:10.1126/science.1234621

[28] Natalio F., **Corrales T. P.**, Panthoefer M., Schollmeyer D., Lieberwirth I., Mueller W. E. G., Kappl M., Butt H.-J. & Tremel W., 2013, Flexible minerals: self-assembled calcite spicules with extreme bending strength, *Science*, 339(6125), 1298302. doi:10.1126/science.1216260

[29] Sethmann I., 2013, Creating flexible calcite fibers with proteins, *Science*, 339(6125), 12812. doi:10.1126/science.1235357

[30] Aizenberg J., Hanson J., Koetzle T. F., Leiserowitz L., Weiner S. & Addadi L., 1995, Biologically Induced Reduction in Symmetry: A Study of Crystal Texture of Calcitic Sponge Spicules, Chemistry a European Journal, 1, 414422. doi: 10.1002/chem.19950010705

[31] Schroeder H. C., Krasko A., Brandt D., Wiens M., Tahir M. N., Tremel W. & Mueller W.E.G, 2007, Silicateins , silicase and spicule-associated proteins : synthesis of demosponge silica skeleton and nanobiotechnological

applications, *Porifera Research: Biodiversity, Innovation and Sustainability*, p.581592. ISBN 978-85-7427-023-4

[32] Binning G., Rohrer H., Gerber C., & Weibel E., 1982, Surface Studies by Scanning Tunneling Microscopy, *Physical Review Letters*, 49, 57. doi: 10.1103/PhysRevLett.49.57

[33] Binnig G., Quate C.F. & Gerber C., 1986, Atomic Force Microscope, *Physical Review Letters*, 56, 930. doi: 10.1103/PhysRevLett.56.930

[34] Meyer G. & Amer N. M., 1988, Novel optical approach to atomic force microscopy, *Applied Physics Letters*, 53(12), 1045. doi:10.1063/1.100061

[35] Tamer N. & Dahleh M., 1994, Feedback control of piezoelectric tube scanners, *Proceedings of the 33rd IEEE Conference on Decision and Control* , vol.2, no., pp.1826,1831 vol.2, 14-16 Dec 1994. doi: 10.1109/CDC.1994.411117

[36] Binnig G., Rohrer H., Gerber C. & Weibel E., 1982, Tunneling through a controllable vacuum gap, *Applied Physics Letters*, 40, 178. doi: 10.1063/1.92999

[37] Park S. & Quate C. F., 1987, Theories of the feedback and vibration isolation systems for the scanning tunneling microscope. *Review of Scientific Instruments*, 58(11), 2004. doi:10.1063/1.1139507

[38] Binnig G., Fuchs H., Gerber Ch., Rohrer H., Stoll E. & E. Tosatti, 1986, Energy-Dependent State-Density Corrugation of a Graphite Surface as Seen by Scanning Tunneling Microscopy, *Europhysics Letters*, 1, 31. doi:10.1209/0295-5075/1/1/005

[39] Selloni A., Carnevali P., Tosatti E., Chen C. D., 1985, Voltage-dependent scanning-tunneling microscopy of a crystal surface: Graphite, *Physical Review B*, 31 (4), 2602-2605. doi: 10.1103/PhysRevB.31.2602

[40] Martin Y., Williams C. C. & Wickramasinghe H. K., 1987, Atomic force microscopeforce mapping and profiling on a sub 100-A? scale. *Journal of Applied Physics*, 61(10), 4723. doi:10.1063/1.338807

[41] Bhushan B., Fuchs H. & Hosaka S., 2004, Applied Scanning Probe Methods,*Springer*. ISBN 978-3-642-35792-3.

[42] Giessibl F. J., 2003, Advances in atomic force microscopy, *Reviews of Modern Physics*, 75 (3), 949-983. doi: 10.1103/RevModPhys.75.949

[43] Albrecht T. R., Gruetter P., Horne D. & Rugar D., 1991, Frequency modulation detection using high-Q cantilevers microscope sensitivity for enhanced force, *Journal of Applied Physics*, 69, 668. doi: 10.1063/1.347347

[44] Horowitz P. & Hill W., 1980, The Art of Electronics, *Cambridge University Press*. ISBN: 9780521370950

[45] Sarid D., 1991, Scanning Force Microscopy, *Oxford University Press*. ISBN 0195344693, 9780195344691

[46] Hutter J. L. & Bechhoefer J., 1993, Calibration of atomic-force microscope tips, *Review of Scientific Instruments*, 64(7), 1868. doi:10.1063/1.1143970

[47] Hertz H., 1882, Ueber die Berührung fester elastischer Körper, Journal für die reine und angewandte Mathematik, 92, 156. doi: 10.1515/crll.1882.92.156

[48] Butt H-. J. & Kappl M., 2010, Surface and Interfacial Forces, *Wiley-VCH*. doi: 10.1002/9783527629411

[49] Case J., Chilver L. & Ross T.F.C, 1999, Strength of Materials and Structures, 4th edition, *Butterworth-Heinemann*.

[50] Colchero J., Gil A. & Baro A., 2001, Resolution enhancement and improved data interpretation in electrostatic force microscopy. *Physical Review B*, 64(24), 245403. doi:10.1103/PhysRevB.64.245403

[51] Martin Y., Abraham D. W. & Wickramasinghe H. K., 1988, High-resolution capacitance measurement and potentiometry by force microscopy, *Applied Physics Letters*, 52(13), 1103. doi:10.1063/1.99224

[52] Crider P. S., Majewski M. R., Zhang J., Oukris H. & Israeloff N. E., 2007, Local dielectric spectroscopy of polymer films, *Applied Physics Letters*, 91(1), 013102. doi:10.1063/1.2753539

[53] Crider P. S., Majewski M. R., Zhang J., Oukris H. & Israeloff N. E., 2008, Local dielectric spectroscopy of near-surface glassy polymer dynamics, *The Journal of chemical physics*, 128(4), 044908. doi:10.1063/1.2825301

[54] Fumagalli L., Ferrari G., Sampietro M. & Gomila G., 2007, Dielectric-constant measurement of thin insulating films at low frequency by nanoscale capacitance microscopy, Applied Physics Letters, 91, 243110. doi: 10.1063/1.2821119

[55] Portes L., Ramonda M., Arinero R. & Girard P., 2007, New method for electrostatic force gradient microscopy observations and Kelvin measurements under vacuum, *Ultramicroscopy*, 107(10-11), 102732. doi:10.1016/j.ultramic.2007.03.012

[56] Schwartz G. A, Riedel C., Arinero R., Tordjeman P., Alegria A. & Colmenero J., 2011. Broadband nanodielectric spectroscopy by means of amplitude modulation electrostatic force microscopy (AM-EFM), *Ultramicroscopy*, 111(8), 13669. doi:10.1016/j.ultramic.2011.05.001

[57] Nguyen H. K., Labardi M., Capaccioli S., Lucchesi M., Rolla P. & Prevosto D., 2012, Interfacial and Annealing Effects on Primary α-Relaxation of Ultrathin Polymer Films Investigated at Nanoscale, *Macromolecules*, 45(4), 21382144. doi:10.1021/ma202757q

[58] Yi J. W., Shih W. Y. & Shih W.-H., 2002, Effect of length, width, and mode on the mass detection sensitivity of piezoelectric unimorph cantilevers, *Journal of Applied Physics*, 91(3), 1680. doi:10.1063/1.1427403

[59] Ilic B., Czaplewski D., Craighead H. G., Neuzil P., Campagnolo C. & Batt C., 2000, Mechanical resonant immunospecific biological detector, *Applied Physics Letters*, 77(3), 450. doi:10.1063/1.127006

[60] Thundat T., Wachter E. A., Sharp S. L. & Warmack R. J., 1995, Detection of mercury vapor using resonating microcantilevers, *Applied Physics Letters*, 66(13), 1695. doi:10.1063/1.113896

[61] **Corrales T. P.**, Laroze D., Zardalidis G., Floudas G., Butt H.-J. & Kappl M., 2013, Dynamic Heterogeneity and Phase Separation Kinetics in Miscible Poly(vinyl acetate)/Poly(ethylene oxide) Blends by Local Dielectric Spectroscopy, *Macromolecules*, 46(18), 74587464. doi:10.1021/ma4007158

[62] Nguyen H. K., Prevosto D., Labardi M., Capaccioli S., Lucchesi M. & Rolla P., 2011, Effect of Confinement on Structural Relaxation in Ultrathin Polymer Films Investigated by Local Dielectric Spectroscopy, *Macromolecules*, 44 (16), 6588-6593.

[63] Riedel C., Sweeney R., Israeloff N. E., Arinero R., Schwartz G. A., Alegria A., Tordjeman P. & Colmenero J., 2010, Imaging dielectric relaxation in nanostructured polymers by frequency modulation electrostatic force microscopy, *Applied Physics Letters*, 96(21), 213110. doi:10.1063/1.3431288

[64] Colmenero, J. & Arbe, A., 2007, Segmental dynamics in miscible polymer blends: recent results and open questions, *Soft Matter*, 3(12), 1474. doi:10.1039/b710141d

[65] Tyagi M., Arbe A., Alegria A., Colmenero J. & Frick B., 2007, Dynamic Confinement Effects in Polymer Blends . A Quasielastic Neutron Scattering Study of the Slow Component in the Blend Poly (vinyl acetate)/ Poly (ethylene oxide), *Macromolecules*, 40 (13), 4568. doi:10.1021/ma070539i

[66] Zhao J., Zhang L. & Ediger M. D., 2008, Poly(ethylene oxide) Dynamics in Blends with Poly(vinyl acetate): Comparison of Segmental and Terminal Dynamics, *Macromolecules*, 41(21), 80308037. doi:10.1021/ma8010526

[67] Harmandaris V. A., Kremer K. & Floudas G., 2013, Dynamic Heterogeneity in Fully Miscible Blends of Polystyrene with Oligostyrene, *Physical Review Letters*, 110(16), 165701. doi:10.1103/PhysRevLett.110.165701

[68] Maranas J., 2007, The effect of environment on local dynamics of macromolecules, *Current Opinion in Colloid & Interface Science*, 12(1), 2942. doi:10.1016/j.cocis.2007.03.003

[69] Zhang G., Zhai X., Ma Z., Jin L., Zheng P., Wang W., Cheng S. Z. D. & Lotz B., 2012, Morphology Diagram of Single-Layer Crystal Patterns in Supercooled Poly(ethylene oxide) Ultrathin Films: Understanding Macromolecular Effect of Crystal Pattern Formation and Selection, *ACS Macro Letters*, 1(1), 217221. doi:10.1021/mz2001109

[70] Jin X., Zhang S. & Runt J., 2004, Broadband Dielectric Investigation of Amorphous Poly(methyl methacrylate)/Poly(ethylene oxide) Blends, *Macromolecules*, 37(21), 81108115. doi:10.1021/ma049281b

[71] Liu J., Sakai V.G. & Maranas J. K., 2006, Composition Dependence of Segmental Dynamics of Poly (methyl methacrylate) in Miscible Blends with Poly (ethylene oxide), 28662874. doi:10.1021/ma052136t

[72] Okerberg B. C., Marand H. & Douglas J. F., 2008, Dendritic crystallization in thin films of PEO/PMMA blends: A comparison to crystallization in small molecule liquids, *Polymer*, 49 (2), 579-587.

[73] Pathak J.A., Colby R.H., Floudas G. & Jerome R., 1999, Dynamics in Miscible Blends of Polystyrene and Poly(vinyl methyl ether), *Macromolecules*, 32 (8), 2553-2561. doi:10.1021/ma9817121

[74] Mueller-Krumbhaar H., Zimmer M., Ihle T. & Saito Y., 1996, Morphology and selection processes in diffusion-controlled growth patterns. *Physica A: Statistical Mechanics and its Applications*, 224 (12), 322-337.

[75] Wang C. H., Zhang X. Q., Fytas G. & Kanetakis J., 1989, Investigation of diffusion processes in poly(ethylene oxide)/poly(methyl methacrylate)

blends by laser light scattering spectroscopy, Journal of Chemical Physics, 91(5), 3160. doi:10.1063/1.457643

[76] Chen Y., Dorgan B. L., McIlroy D. N. & Aston E.D., 2006, On the importance of boundary conditions on nanomechanical bending behavior and elastic modulus determination of silver nanowires, *Journal of Applied Physics*, 100(10), 104301. doi:10.1063/1.2382265

[77] Kluge D., Abraham F., Schmidt S., Schmidt H.-W. & Fery A., 2010, Nanomechanical properties of supramolecular self-assembled whiskers determined by AFM force mapping, *Langmuir* , 26(5), 30203. doi:10.1021/la904780c

[78] Zhang L., D'Acunzi M., Kappl M., Imhof A., Van Blaaderen A., Butt H.-J., Graf R. & Vollmer D., 2010, Tuning the mechanical properties of silica microcapsules, *Physical Chemistry Chemical Physics : PCCP*, 12(47), 153928. doi:10.1039/c0cp00871k

[79] Audoly B. & Neukirch S., 2005, Fragmentation of Rods by Cascading Cracks: Why Spaghetti Does Not Break in Half, *Physical Review Letters*, 95(9), 095505. doi:10.1103/PhysRevLett.95.095505

[80] Gladden J., Handzy N., Belmonte A. & Villermaux E., 2005, Dynamic Buckling and Fragmentation in Brittle Rods, *Physical Review Letters*, 94(3), 035503. doi:10.1103/PhysRevLett.94.035503

[81] Hendee W. R. & Ritenour E. R., 2003, Ultrasound Waves Medical Imaging Physics, pp. 303316, *John Wiley & Sons Inc.* doi:10.1002/0471221155.ch19

[82] Santos H. M., Lodeiro C. & Capelo-Martnez J.-L., 2009, The Power of Ultrasound. Ultrasound in Chemistry, pp. 116. doi:10.1002/9783527623501.ch1

[83] Yasui K., 2002, Influence of ultrasonic frequency on multibubble sonoluminescence, *The Journal of the Acoustical Society of America*, 112(4), 1405. doi:10.1121/1.1502898

[84] Burdin F., Tsochatzidis N.A., Guiraud P., Wilhelm A.M. & Delmas H., 1999, Characterisation of the acoustic cavitation cloud by two laser techniques, *Ultrasonics Sonochemistry*, 6(1-2), 4351. doi:10.1016/S1350-4177(98)00035-2

[85] Levi C., Barton J. L., Guillemet C., Bras E. & Lehuede P., 1989, A remarkably strong natural glassy rod: the anchoring spicule of the Monorhaphis sponge, *Journal of Materials Science Letters*, 8 (3), 337-339. doi:10.1007/BF00725516

[86] Sarikaya M., Fong H., Sunderland N., Flinn B. D., Mayer G., Mescher A. & Gaino E., 2011, Biomimetic model of a sponge-spicular optical fibermechanical properties and structure, *Journal of Materials Research*, 16(05), 14201428. doi:10.1557/JMR.2001.0198

[87] Woesz A., Weaver J. C., Kazanci M., Dauphin Y. , Morse D. E., Aizenberg J. & Fratzl P., 2006, Micromechanical Properties of Biological Silica in Skeletons of Deep-Sea Sponges, Journal of Materials Research, 21, 2068-2078. doi:10.1557/JMR.2006.0251

[88] Johnson M., Walter S. L., Flinn B. D. & Mayer G., 2010, Influence of moisture on the mechanical behavior of a natural composite, *Acta Biomaterialia*, 6(6), 21818. doi:10.1016/j.actbio.2009.12.006

[89] Miserez A., Weaver J. C., Thurner P. J., Aizenberg J., Dauphin Y., Fratzl P., Morse D. E. & Zok F.W., 2008, Effects of Laminate Architecture on Fracture Resistance of Sponge Biosilica: Lessons from Nature, *Advanced Functional Materials*, 18(8), 12411248. doi:10.1002/adfm.200701135

[90] Emlet R. B., 1982, Echinoderm Calcite: A Mechanical Analysis from Larval Spicules, *The Biological Bulletin* , 163 (2), 264275.

[91] Berman A., Addadi L., Kvick Å., Leiserowitz L., Nelson M. & Weiner S., 1990, Intercalation of Sea Urchin Proteins in Calcite: Study of a Crystalline Composite Material. Science , 250 (4981), 664667. doi:10.1126/science.250.4981.664

[92] Wong E. W., 1997, Nanobeam Mechanics: Elasticity, Strength, and Toughness of Nanorods and Nanotubes, *Science*, 277(5334), 19711975. doi:10.1126/science.277.5334.1971

[93] Whitesides G. M. & Grzybowski B., 2002, Self-Assembly at All Scales,*Science* , 295 (5564), 24182421. doi:10.1126/science.1070821

[94] Hang F., Lu D., Li S. W. & Barber A. H., 2009, Stress-strain behavior of individual electrospun polymer fibers using combination AFM and SEM, *MRS Online Proceedings Library*, 1185-II07-10. doi:10.1557/PROC-1185-II07-10

[95] Hang F., Dun L., Russell J. B., Ines J.-P., Urszula S., Beatriz C.-B., Martin D., Martin Z., Christoph B. & Asa H. B., 2011, In situ tensile testing of nanofibers by combining atomic force microscopy and scanning electron microscopy, *Nanotechnology*, 22 (36), 365708. doi:10.1088/0957-4484/22/36/365708